

KAUNAS UNIVERSITY OF TECHNOLOGY

PRASAD SHIMPI

DEVELOPMENT OF SELF-SENSING 3D
WOVEN AND MULTIAXIAL COMPOSITES

Doctoral dissertation
Technological Science, Mechanical Engineering (T 009)

2024, Kaunas

This doctoral dissertation was prepared at Kaunas University of Technology, Faculty of Mechanical Engineering and Design, Department of Mechanical Engineering during the period of 2019–2023.

The doctoral right has been granted to Kaunas University of Technology together with Vytautas Magnus University.

Scientific Supervisor:

Prof. Dr. Daiva ZELENIAKIENĖ (Kaunas University of Technology, Technological Sciences, Mechanical Engineering, T 009).

Edited by: English language editor Dr. Armandas Rumšas (Publishing House *Technologija*), Lithuanian language editor Aurelija Gražina Rukšaitė (Publishing House *Technologija*).

Dissertation Defence Board of Mechanical Engineering Science Field:

Assoc. Prof. Dr. Kęstutis PILKAUSKAS (Kaunas University of Technology, Technological Sciences, Mechanical Engineering, T 009) – **Chairperson**;

Prof. Dr. Rimvydas MILAŠIUS (Kaunas University of Technology, Technological Sciences, Materials Engineering, T 008);

Assoc. Prof. Dr. Tatjana GLASKOVA-KUZMINA (University of Latvia, Latvia, Technological Sciences, Mechanical Engineering, T 009);

Dr. Andrejs KOVALOVŠ (Riga Technical University, Latvia, Technological Sciences, Mechanical Engineering, T 009).

The official defence of the dissertation will be held at 10 a.m. on 18 March 2024 at the public meeting of the Dissertation Defence Board of Mechanical Engineering Science Field in Rectorate Hall at Kaunas University of Technology.

Address: K. Donelaičio 73–402, LT-44249 Kaunas, Lithuania.

Phone (+370) 608 28 527; email doktorantura@ktu.lt

The doctoral dissertation was sent out on 15 February, 2024.

The doctoral dissertation is available on the internet at <http://ktu.edu> and at the libraries of Kaunas University of Technology (Gedimino 50, Kaunas LT-44239, Lithuania) and Vytautas Magnus University (K. Donelaičio 52, Kaunas LT-44244).

© P. Shimpi, 2024

KAUNO TECHNOLOGIJOS UNIVERSITETAS

PRASAD SHIMPI

SAVIDIAGNOSTINIŲ TRIMAČIŲ
AUSTINIŲ IR DAUGIAAŠIŲ KOMPOZITŲ
TYRIMAS

Daktaro disertacija
Technologijos mokslai, mechanikos inžinerija (T 009)

2024, Kaunas

Disertacija rengta 2019–2023 metais Kauno technologijos universiteto Mechanikos inžinerijos ir dizaino fakultete Mechanikos inžinerijos katedroje.

Doktorantūros teisė Kauno technologijos universitetui suteikta kartu su Vytauto Didžiojo universitetu.

Mokslinis vadovas:

prof. dr. Daiva ZELENIAKIENĖ (Kauno technologijos universitetas, technologijos mokslai, mechanikos inžinerija, T 009).

Disertaciją redagavo: anglų kalbos redaktorius dr. Armandas Rumšas (leidykla „Technologija“), lietuvių kalbos redaktorė Aurelija Gražina Rukšaitė (leidykla „Technologija“).

Mechanikos inžinerijos mokslo krypties disertacijos gynimo taryba:

doc. dr. Kęstutis PILKAUSKAS (Kauno technologijos universitetas, technologijos mokslai, mechanikos inžinerija, T 009) – pirmininkas;

prof. dr. Rimvydas MILAŠIUS (Kauno technologijos universitetas, technologijos mokslai, medžiagų inžinerija, T 008);

doc. dr. Tatjana GLASKOVA-KUZMINA (Latvijos universitetas, Latvija, technologijos mokslai, mechanikos inžinerija, T 009);

dr. Andrejs KOVALOVŠ (Rygos technikos universitetas, Latvija, technologijos mokslai, mechanikos inžinerija, T 009).

Disertacija bus ginama viešame mechanikos inžinerijos mokslo krypties disertacijos gynimo tarybos posėdyje 2024 m. kovo 18 d. 10 val. Kauno technologijos universiteto Rektorato salėje.

Adresas: K. Donelaičio g. 73–402, LT-44249 Kaunas, Lietuva.

Tel. (+370) 608 28 527; el. paštas doktorantura@ktu.lt

Disertacija išsiųsta 2024 m. vasario 15 d.

Su disertacija galima susipažinti interneto svetainėje <http://ktu.edu>, Kauno technologijos universiteto bibliotekoje (Gedimino g. 50, LT-44239 Kaunas, Lietuva) ir Vytauto Didžiojo universiteto bibliotekoje (K. Donelaičio g. 52, LT-44244 Kaunas).

© P. Shimpi, 2024

TABLE OF CONTENTS

LIST OF TABLES	8
LIST OF FIGURES.....	9
LIST OF ABBREVIATIONS AND DEFINITIONS.....	11
INTRODUCTION.....	12
I. LITERATURE REVIEW	16
1.1. 3D Weaving and Manufacturing Composites	16
1.2. Angle Interlock.....	17
1.3. Orthogonal / Noobing 3D Weaving	19
1.4. Biased Weaving and Multiaxial Composites.....	21
1.5. Weaving of Biased Yarns by Constructing a New Machine	21
1.6. Weaving of Biased Yarns on Modified Looms	23
1.7. Structural Health Monitoring of 3D Woven Composite Using Nanoparticles	24
1.7.1. Structural health monitoring using carbon nanotubes	25
1.7.2. Structural health monitoring using MXene nanoparticles	26
1.8. Simulation of Impact and Tensile Loading on Composites	28
1.9. Finite element modelling of composite materials.....	29
1.10. Summary of the Literature Review	31
II. MATERIALS AND METHODS.....	33
2.1. Infusion of CNT in 3D Woven Glass Fibre Composite	33
2.1.1. Preparation of CNT masterbatch	33
2.1.2. Composite manufacturing	33
2.1.3. Microscope characterization.....	35
2.1.4. Tensile testing of composite samples	35
2.1.5. Flexural testing of composite panels	37
2.2. Doping of MXene Nanoparticles on T-profile Composite.....	39
2.2.1. Preparation of MXene nanoparticles	39
2.2.2. Manufacturing of T-profile composite	40

2.2.3.	Tensile testing of T-profile composite.....	42
2.2.4.	Fatigue testing of T-profile composite	42
2.3.	Multiaxial Woven Composite Manufacturing and Characterization..	43
2.3.1.	Design of a multiaxial pattern	43
2.3.2.	Manufacturing of multiaxial composite and tensile testing.....	45
2.3.3.	Development of multiaxial fabrics on a closed reed mechanism ...	46
2.4.	Simulation of Multiaxial Composite Mechanical Properties.....	46
2.4.1.	Material properties and meshing of glass fibre composites.....	46
2.4.2.	Ply layup in ACP pre-module.....	47
2.4.3.	Boundary conditions for tensile testing	47
2.4.4.	Material properties and meshing of carbon fibre composites.....	48
2.4.5.	Boundary conditions for impact loading	49
III.	RESULTS AND DISCUSSION	51
CNT	3.1. SHM of Orthogonal 3D Woven Planar Composites Infused with	51
	51
	3.1.1. Microscopic characterization of CNT dispersed in 3D woven	51
	3.1.2. Tensile test and electromechanical response of CNT.....	53
conditions	3.1.3. Electromechanical response of CNT under flexural loading	55
	55
	3.1.4. Summary of research findings for SHM of 3D woven.....	57
	composite by CNT	57
	3.2. SHM of 3D Woven T-profile Composite Doped with	58
	MXene Nanoparticles.....	58
	3.2.1. Electromechanical response of MXene flakes under	58
	tensile loading	58
loading	3.2.2. Electromechanical response of MXene nanoparticles under fatigue	61
	61
using MXene	3.2.3. Summary of research findings from SHM of T-profile composite	63
nanoparticles	63
	3.3. Multiaxial Composite Mechanical Test and Results	64
	3.3.1. Tensile testing of ORW pattern composite with a 5 mm hole.....	64
	3.3.2. Effect of hole diameter on reinforcement of composites.....	66

3.3.3.	Weaving of multiaxial preforms on closed reed.....	66
3.3.4.	Manufacturing of multiaxial composite	69
3.3.5	Impact testing of multiaxial composite manufactured by closed reed	69
3.3.6	Summary of research findings from mechanical characterization of multiaxial composites.....	73
3.4	Finite Element Analysis of Multiaxial Composites.....	74
3.4.1	Static structural analysis of ORW composites	74
3.4.2	Finite element analysis of impact loading of carbon composite.....	76
3.4.3	Summary of the research findings for FEA of multiaxial composites	77
4.	CONCLUSIONS	79
5.	ANOTACIJA	81
	REFERENCES.....	101
	CURRICULUM VITAE	115
	ACKNOWLEDGEMENTS	117

LIST OF TABLES

Table 2.1. Orthogonal 3D woven fabric data	33
Table 2.2. Sample codes and manufacturing methods	34
Table 2.3. Fatigue testing parameters.....	43
Table 2.4. Possible angles for MAF.....	44
Table 2.5. Multiaxial weaving patterns	44
Table 2.6. Material properties of glass fibre composites.....	46
Table 2.7. Material properties of bisphenol epoxy F.....	48
Table 2.8. Material properties generated for carbon composite	48
Table 3.1. Gauge factor and correlation coefficient for tensile test.....	53
Table 3.2. Statistical analysis of tensile testing samples	53
Table 3.3. Sample code and ultimate flexural force	56
Table 3.4. Correlation coefficient and ultimate tensile force	61
Table 3.5. Tensile testing data of ORW composites	64
Table 3.6. Stacking sequence and sample codes	69
Table 3.7. Impact testing results of carbon fibre composites	70

LIST OF FIGURES

Fig. 1.1 Weaving loom for manufacturing orthogonal fabric [97]	19
Fig. 1.2 Fibre orientations: a) orthogonal 3D weaving; b) biased weaving [39]	21
Fig. 2.1 Modified VARTM processes: (a) stacking sequence in layup, (b) schematic of the process [126].....	35
Fig. 2.2 SHM of 3D woven composite during tensile loading [126].....	36
Fig. 2.3 Composite samples flexural loading and resistance measurement schematics: a) through-thickness, b) single surface [126].....	38
Fig. 2.4 Scanning electron microscope analysis of MXene: (a) partially delaminated scattered MXene flakes, (b) single MXene flake [139]	39
Fig. 2.5 Weaving of T-profile: (a) weave design, draft and peg plan, (b) denting plan, (c) warp cross sectional view of T-profile [139].....	40
Fig. 2.6 3D woven composite T-profile: (a) specimen dimensions, (b) experimental setup for tensile and fatigue loading [139]	42
Fig. 2.7 Manufacture of composite: a) sandwich plies of MAF 34°, b) resin infusion of plies	45
Fig. 2.8 Meshing and boundary conditions of glass fibre composite sample for tensile loading	46
Fig. 2.9 Schematic of workflow in <i>Ansys</i>	47
Fig. 2.10 Meshing of carbon fibre composite plate	49
Fig. 2.11 Schematic of the workflow for simulation of impact loading[167].....	49
Fig. 2.12 Boundary conditions for impact loading of carbon composites [167].....	50
Fig. 3.1 CNT infusion by conventional VARTM process: (a–c), CNT infusion by vacuum transfer process (d–f) [78].....	51
Fig. 3.2 SEM characterization of S ₃ .G ₁ sample: (a) micro cluster of CNT, (b) CNT in resin-rich area as micro clusters (the white marking), (c) cross-section of warp fibrils in the matrix, (d) cross section of weft and warp fibrils [126]	52
Fig. 3.3 Real time damage sensing during tensile loading: a) S ₁ .G ₁ , b) S ₁ .G ₂ , c) S ₃ .G ₁ [126]54	
Fig. 3.4 Real time damage sensing during flexural testing: (a) S ₃ .G ₁ , (b) S ₃ .G ₂ surface subjected to tensile stress, (c) S ₃ .G ₂ surface subjected to bending stress [126]	56
Fig 3.5 Statistical analysis of T profile composite samples.....	59
Fig. 3.6 Real time deformation monitoring of composite T-profile: (a) tensile testing of composite T-profile, (b) piezoresistive response of MXene coating, (c) enlarged section of the initial failure [139]	60
Fig. 3.7 Real-time fatigue sensing of composite T-profile by MXene coating: (a) resistance measurement at 50 N–0.5 Hz, (b) sensing of displacement component during fatigue loading	

of 2000 cycles, (c) resistance measurement at 100 N–1 Hz, (d) sensing of displacement component during fatigue loading of 4000 cycles [139].....	62
Fig. 3.8 Comparison of ultimate tensile force for MAF patterns	65
Fig. 3.9 Comparison of hole reinforcement of ORW composite	66
Fig. 3.10 Multiaxis weaving on closed reed loom: a) anchoring of bias fibre to base fabric, b) advancement of fabric by n weft insertions, c) anchoring of bias fibre at m distance from selvage, d) return of the shuttle to the starting point, e) advancement of the anchor point, f) reversal of the direction for anchoring bias fibre [167].....	67
Fig. 3.11 Conceptualization of bias weaving parameters: a) distance between anchoring warp fibres m , b) number of inserted weft fibres n , c) angle θ between the warp and the bias fibre [167].....	68
Fig. 3.12 Force-time history comparison of: a) S_1 with S_2 , b) S_1 with S_3 [167].....	71
Fig. 3.13 Force-time history comparison of: a) S_1 with S_4 , b) S_1 with S_5 [167].....	72
Fig. 3.14 Experimental and simulation results of tensile testing	75
Fig. 3.15 Bar chart for stress values at the edge of the hole.....	75
Fig. 3.16 Stress distribution of individual MAF ply	76
Fig. 3.17 Comparison of experimental and numerical results of impact loading: a) plain woven, b) multiaxial woven [167]	76

LIST OF ABBREVIATIONS AND DEFINITIONS

Abbreviations

CNT – Carbon nanotube.
FEA – Finite element analysis
GF – Gauge factor
MAF – Multiaxial fibre
PDA – Progressive damage analysis
RTM – Resin Transfer Moulding
RVE – Representative Volume Element
SHM – Structural Health Monitoring
SEM – Scanning electron microscope.

Definitions

Angle interlock – a type of 3D weaving structure wherein fibres are interwoven through the fabric's thickness.
Bias weaving – a technique for weaving fibres in more than three directions.
Beat-up – pushing the final inserted thread toward the place where the fabric or perform is formed (fell).
Binder threads – fibres incorporated in angle interlock or orthogonal 3D weave structure to bundle the Y and X fibres together.
Creel – an input device for fibres or threads during weaving.
Dobby/Jacquard – a device to form shed on a weaving loom.
Fell – cloth/preform formation point.
Fibre Volume – the volume of the fibres occupied in the total volume of the preform.
Glass, carbon – a type of fibre used in technical textiles.
Heald shaft – a device used in conjugation with dobbie/jacquard on a weaving loom to open or close the shed.
Heald eye – a part of the head shaft where fibres are passed through.
Let-off – a device for sequential release of fibres during weaving.
Noobing – non-interlacing orthogonal interlacing and binding.
Warp – fibre incorporated in the machine/length direction of the fabric.
Weft – fibre incorporated in the cross machine/width direction of the fabric.

INTRODUCTION

The field of composites has seen significant advancements in recent years, with a focus on developing new and innovative materials for use in aerospace, civil engineering and other industries. *Structural Health Monitoring* (SHM) of composites and multiaxial composites represent the promising areas where smart composites capable of in-situ detection of damage as well as advanced composites with fibres integrated in more than 2 directions are under development.

SHM of composites refers to the process of monitoring the structural integrity and performance of composite materials using various techniques and technologies [1–13]. Composites are materials that are made up of two or more distinct components, typically a matrix material and a reinforcement, combined to create a material with improved mechanical properties. However, these materials can also be susceptible to various types of damage, such as delamination, fibre breakage, matrix cracking, and moisture absorption, which can significantly affect their mechanical performance and structural integrity over time. SHM techniques for composites typically involve the use of sensors, data acquisition systems, and analysis algorithms to monitor the condition of composite structures, detect any potential damage or degradation, and provide early warning of structural issues continuously or periodically. Some common SHM techniques used for composites include strain sensors, acoustic emission sensors, ultrasonic sensors, thermography, vibration analysis, piezoresistance sensors, data analysis and machine learning [14–23]. Out of all techniques, the electrical resistance sensors for SHM of composites have been studied extensively by embedding a wide variety of nanoparticles, such as carbon nanotubes (CNT), graphene, MXene, etc., during various stages of composite manufacturing.

CNTs are nanoscale cylindrical structures made of carbon atoms whereas MXenes are 2-dimensional (2D) materials derived from selective etching of titanium carbide MAX phase. These nanoparticles exhibit high electrical conductivity and piezoresistance characteristics which are beneficial for SHM of composites. It has also been determined that these nanoparticles enhance the mechanical properties of the composites, thus making them an ideal candidate for the detection of damage in composites [24–33].

Although SHM of composites using nanoparticles has been a subject of studies for 2D laminated composites, there exists a significant lack in studying the behaviour of these nanoparticles when embedded in 3-dimensional (3D) woven composites. 3D weaving is an upcoming area in composite manufacturing where fibres are integrated in 3 directions during the weaving stage to make a preform devoid of any layers. 3D woven composites eliminate delamination and exhibit superior mechanical properties as compared to 2D laminated composites [34–41].

Multiaxial composites are an upcoming area in composite manufacturing, where fibres are integrated in more than 2 directions during the preform manufacturing stage. The usual process in manufacturing the multiaxial preform is knitting, braiding or weaving of the fibres, out of which, weaving provides the highest dimensional

stability. However, weaving of the multiaxial preform on the conventional weaving loom poses significant challenges as the heald wires and reed pose an obstacle during indexing of multiaxial fibre at the required angle. To overcome this challenge, researchers have developed innovative techniques and modifications in the weaving loom to integrate fibres in more than 2 directions. One of the techniques to weave multiaxial preforms is by using open reed on the conventional weaving loom. This type of reed has open dents, as opposed to closed reed on the conventional loom where reed dents are closed on both sides. The open reed has special dents for multiaxial fibres as well as special heald shafts which have freedom to move in 2 axes [36, 42–73].

Although there exist a variety of techniques to weave multiaxial preforms, there is also a gap in the development of new techniques of manufacturing multiaxial preforms. In addition, there is significant lack in the studies of the mechanical properties of multiaxial composites and the effect of incorporating multiaxial fibre in conventional composites, in the practical as well theoretical manner.

The purpose of this research is to explore the potential of 3D woven composites infused with CNT and MXene nanoparticles for use in SHM systems, and also to study their behaviour in tensile, flexural, and fatigue load conditions. In addition, advanced composite manufacturing techniques for producing multiaxial woven composites have been explored, and mechanical properties of the multiaxial composites have been evaluated.

Research aim and tasks

The aim of this research is to design, develop and manufacture self-sensing 3D woven and multiaxial composites. To achieve this aim, the following tasks have been carried out:

1. To develop glass fibre 3D woven composites embedded with CNT.
2. To develop glass fibre 3D woven T-profile composites doped by MXene nanoparticles.
3. To design and develop multiaxial composites by the open and closed reed weaving method.
4. To study efficiency of SHM of 3D woven composites by monitoring the electromechanical response during tensile, flexural, and fatigue testing.
5. To analyze the tensile and impact properties of multiaxial composites.
6. To develop the simulation model to evaluate the mechanical behaviour of multiaxial composites.

Scientific novelty

1. A novel technique has been developed to infuse CNT in a localised area of glass fibre 3D woven composites by using a porous material. The technique reduced the quantity of CNT required for efficient SHM of 3D woven composites, thus saving material costs.
2. A novel glass fibre 3D woven T-profile composite has been manufactured by doping the junction region with MXene nanoparticles. This technique has proven to be successful in sensing the damage in-situ of complex shaped composites.

A novel technique has been developed to weave multiaxial preforms on a closed reed weaving mechanism, thus eliminating the requirement of complex changes in the conventional weaving looms.

Practical significance

The significance of this research lies in its potential to provide new and innovative composite materials for use in SHM systems, and to advance the field of multiaxial composites. The findings of this study could lead to improved structural safety and reliability in various industries, as well as more profound understanding of the behaviour of 3D woven composites infused with CNT and MXene nanoparticles in tensile, flexural and fatigue load conditions. On the other hand, the new technique developed to manufacture the multiaxial composite by weaving preforms on closed reed could be beneficial in mass production. In addition, the research results of glass fibre multiaxial composites can significantly improve the composite design by making a hole more robust while keeping the cost competitive.

Statements presented for defence

1. CNT integrated by the vacuum transfer method on a glass fibre 3D woven composite can function as a damage sensor under tensile and flexural loading conditions. CNT transferred via a porous material under vacuum pressure does not get filtered by glass fibres.
2. MXene nanoparticles doped on glass fibre 3D woven T-profile composites can detect damage under tensile and fatigue loading conditions. The spraying of MXene nanoparticles on the junction region of a T-profile composite makes the process easy to manufacture and utilizes the minimum amount of MXenes.
3. Multiaxial composites having fibres integrated in more than 2 directions help to tailor the mechanical properties of composites. Multiaxial composites manufactured by open and closed reed can reinforce carbon composites under impact loading and glass fibre composites under tensile loading, respectively.

Publications of the research results

The results of this research have been presented in three peer-reviewed publications in journals referred in the *CA WoS* database, and in one peer-reviewed publication in conference proceedings. In addition, experimental results have been presented at three international conferences.

Structure and outline of the dissertation

The dissertation is structured into five chapters, including an introduction, literature review, materials and methods, results & discussion, and conclusion. The introduction provides a brief overview of the research and its objectives, while the literature review covers the relevant background information and previous studies in the field. The methodology chapter outlines the methods and techniques used in the research, while the results chapter presents and analyses the findings. The discussion chapter explores the implications of the results, and the conclusion summarizes the

key findings and provides recommendations for future research. The thesis comprises 118 pages, 31 figures, and 15 tables.

1. LITERATURE REVIEW

Composites have a wide range of applications, ranging from automobiles to windmills and the sports industry. In most of the areas, they are used as a structural component. One of the applications is in the aerospace industry where heavier metal parts are replaced with lightweight composites denoted by a similar strength and load bearing capacity. The basic constituents of such composites are the reinforcement and the matrix material. Textile materials from specially developed fibres such as carbon and glass fall under the category of reinforcement. Carbon is mainly used in the aerospace industry due to its high strength and lightweight properties. As it is a brittle fibre, bending and abrasion causes filamentation and end breakage; therefore, special machines and assemblies are developed to handle carbon yarns during the textile process.

Composites for aerospace applications are made by laying multiple sheets of woven carbon fabric on a mould until the desired thickness is achieved [74, 75]. Each layer of the layup is wetted with epoxy resin or a suitable matrix, stacked upon each other in the mould, and then cured at high temperatures. The resin is transferred by one of the two processes – either by 1) RTM (*Resin Transfer Moulding*) [76], or by 2) VaRTM (*Vacuum Assisted Resin Transfer Moulding*) [77].

One of the major drawbacks in this process is the delamination of layers when subjected to tensile or compressive loads [78]. To overcome this problem, the entire layup is reinforced additionally by stitching [79], Z pinning, or tufting [80]. The stitching process uses threads and a needle to insert and lock threads through the thickness at various points. In Z-pinning, short pins of a length equal to the layup thickness are punched at predefined places on the fabric. These pins can be of carbon or another metallic material. Tufting is a process where threads are penetrated through the thickness of the layup by stitching needles.

1.1. 3D Weaving and Manufacturing Composites

Researchers have come up with a new method of 3D weaving where, instead of fabric layers, yarns are stacked upon each other in layers prior to weaving [39, 81, 82]. These layers are then woven according to the requirements in various manners to yield a fabric having the desired thickness. This eliminates the complete layup process, and the resultant fabric does not delaminate. The 3D fabric is then subjected to similar matrix treatment as discussed above and heat-cured to give a composite. There are primarily two methods of weaving 3D fabrics, viz, 1) angle interlock, and 2) orthogonal/noobing

1.2. Angle Interlock

Angle interlock 3D weaving is a type of a 3D weaving technique used in the production of composite materials. It involves the interlocking of yarns or fibres at specific angles to create a stable and load-bearing structure. In angle interlock 3D weaving, the yarns are woven at different angles to each other to create a strong, interlocking matrix which can withstand both tensile and compressive forces [83, 84].

Angle-interlock preforms are created by layering several warp layers (longitudinal fibres; 'X' direction) on top of each other and interlacing them with numerous weft layers (transverse fibres; 'Y' axis) in predetermined patterns to create one thick preform with no discernible individual layers [85, 86]. Due to their interlaced architectures, these thick preforms are anticipated to have greater shear, delamination resistance, impact damage tolerance, and better heat dispersion when used in composites [87]. These characteristics are necessary for both structural and thermal applications, such as brake pads, exhaust cones, and wing sections.

As the fibres are interlocked, thus the mechanical properties across thickness tend to be homogenized [88]. Also, angle interlock fabric preforms show higher drapability as compared to other 3D weaving processes, thus making this concept suitable for complex geometries. The preforms can be woven on a conventional weaving loom with the addition of a dobby or jacquard attachment, thereby making it a more accessible option compared to orthogonal weaving. This is a significant advantage because it enables the creation of a wide range of weave architectures by simply changing the weave designs.

One of the most notable features of angle interlock weaving is the ability to create preforms with a high level of mouldability and drapeability [34]. This makes it an attractive option for researchers exploring applications in areas such as ballistics, where the layer-to-layer structure and interweaves play a critical role in supporting the material. Additionally, the option to increase the fibre content of the preform by using stuffer threads leads to improvements in the structural properties, thereby making it a more suitable option for certain applications where the strength is a primary concern.

As the name suggests, the angle interlock architecture involves each yarn traveling at an angle from its starting plane to the subsequent layers, which results in all layers being interlocked and contributing to the thickness of the fabric.

Based on the degree of interlocking, angle interlock weaving can be split into two categories. Examples include layer-to-layer angle interlocking and through thickness. Each yarn contributes to the X, Y, and Z content while simultaneously traversing the thickness from surface to surface in the through thickness variation. If the angular arrangement is along the warp, the contribution is made toward X and Z; if it is along the weft, the contribution is made toward Y and Z. The number of layers and their thickness determine the angle at which each thread moves.

On the other hand, yarns in the layer-to-layer variation only traverse to the subsequent neighbouring layer before returning to their original plane. Angle interlock weaving requires specialized 2D weaving equipment with the capacity to alter the paths of the threads while weaving.

The mechanical properties of 3D-woven composites under both tension and compression loading conditions have been analyzed [89]. The authors focused on the influence of the weaving structural parameters on the mechanical behaviour of the composites. In their study, they considered various parameters, such as the yarn count, the fabric thickness, and the weave pattern to understand how they impact the mechanical properties.

A comparative study on the fatigue properties and damage processes of 3D-woven composite plates with different numbers of layers (three and five layers) under tensile cyclic loading was conducted [90]. It was discovered that there were five stages to the fatigue damage mechanisms: transverse surface crack formation, transverse matrix crack generation, debonding between the warp and weft yarns, growth of debonding and weft fibre breaking, and accumulation of damage leading to specimen rupture. The first two stages occurred within one tenth of the fatigue life, whereas the third and fourth stages, which were critical, occurred from one tenth of the fatigue life until almost the specimen's failure point. The accumulation of damage that eventually caused the specimen to fail was the last step.

For the through-thickness 3D-woven composite, a finite element model and an analytical model were created [91, 92]. The objectives of the study were to examine the mechanical behaviour of the composites and to forecast their coefficients of thermal expansion. The authors discovered that the finite element result and the analytical result were in good agreement, thus demonstrating the ability of the models to offer helpful data for comprehending the behaviour of 3D-woven composites under various loading circumstances.

By using the load-control experimental approach, the compression-compression fatigue characteristics of 3D-woven composites were analysed [93]. The authors discovered that it was the accumulated damage to the resin close to the yarns that caused the composite's eventual fatigue failure by looking at the damage morphology at the cross-section.

The fatigue performance of layer-to-layer 3D weaving angle interlock composites was the subject of an extensive investigation [88]. The 3D weaving angle interlock composite's three-point bending fatigue was examined in this investigation, and it was shown that the integrated construction structure of the composite prevented delamination even under high-cycle fatigue circumstances. The performance of the 3D woven angle interlock and 3D woven orthogonal composites in quasi-static three-point bending and bending fatigue were also compared. The 3D angle interlock woven composite exhibited a longer fatigue life at the same stress levels, whereas the 3D orthogonal woven composite performed better in terms of quasi-static bending resistance.

Under tension-tension fatigue loading, the 3D angle interlock woven composite's damage and failure were examined using the acoustic emission (AE) technology, optical microscopy, micro-CT, etc. [94]. According to the findings, debonding took place at the warp tow-matrix-weft tow interface, where the warp tows had the greatest amount of undulation. In order to identify the mechanisms and forms of damage during cyclic loading, tests were also paused at specified points in the

fatigue life. It was discovered that fatigue damage happened in three separate stages involving different damage modes.

1.3. Orthogonal / Noobing 3D Weaving

Noobing is non-interlacing, orthogonally orientating, and binding, according to Nandan Khokhar [95]. A set of linear yarns that are arranged in either a uniaxial or a multi-axial orientation and are commonly referred to as stuffer yarns are bound or tied by using the necessary sets of binding yarns to create a corresponding layer-less 3D fabric which essentially consists of three orthogonal yarn sets that do not interlace, inter-loop, or intertwine. No sets of yarns, aside from the binder threads, are intertwined, in contrast to the 3D weaving method, where each set of yarns is interwoven with every other yarn.

In the noobing process, as shown in Fig. 1.1, the layers do not interlace with either weft or among themselves, but are just stacked upon each other, while a special set of threads is used to interweave and bind all the layers and weft together [96, 97]. To weave 3D noobed fabric on a conventional loom, yarns comprising of each layer have to be drawn through a separate heald shaft [98]. The stuffer yarns of any layer do not participate in interlacement, and the whole layer is lifted to allow the weft yarn to be passed. Moreover, each heald shaft has to be lifted for passing the weft and lowered to facilitate the lifting of other shafts.

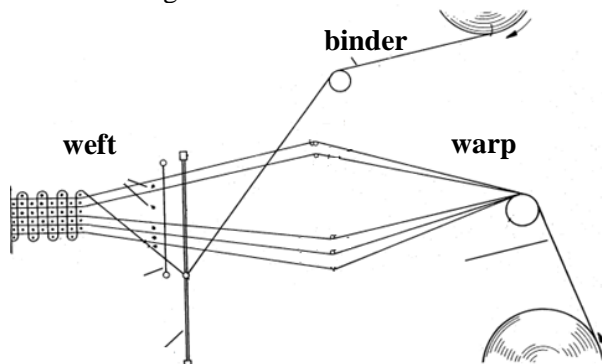


Fig. 1.1 Weaving loom for manufacturing orthogonal fabric [97]

This repeated movement of lifting and lowering imparts much damage to carbon yarns. Therefore, researchers have developed a new technique of shed formation called *pseudo shedding* where the individual layers are staggered permanently in the vertical direction at a predetermined height, thus forming multiple open sheds at the picking point which are also staggered vertically. This method eliminates the unnecessary movement of yarns during each cycle of weft insertion. There are many already available methods to create the pseudo shed as follows:

1. Soldering the reed at specific places on alternate dents according to the required layer height. This is suitable only for a lower number of layers/sheds;
2. Using a perforated plate or polished steel rods to space the layers vertically [99];
3. Using special heald wires having multiple eyelets [100];
4. Using a Jacquard head [101].

It has been investigated how the Z-yarn quantity and location affect the in-plane characteristics of 3D woven structures. The in-plane characteristics diminish as the Z-yarn volume fraction ratio rises. However, a local delamination-type failure event could happen if the ratio falls. Due to the Z-yarn, the 3D woven or 2D fabric/stitched composites limit the impact energy to the immediate area when subjected to an impact load.

An experimental study was conducted on multiaxial and orthogonal 3D woven composites to determine their bending strength and modulus [38]. The results showed that the orthogonal woven composites had a higher bending strength of 569 MPa and a higher modulus of 50.5 GPa compared to the multiaxial woven composites which had a bending strength of 43.5 MPa and a modulus of 715 MPa.

The study also examined the bending failure modes of composites. The failure of the multiaxial woven composite was caused by local delamination between the filler and the bias yarns where it was constrained by the Z-yarn and the bias yarn breakage at the outside surface of the warp side. In contrast, the bending failure in the orthogonal woven composite involved matrix and yarn breakages that first happened in the normal direction of the yarn, but later spread parallel to the yarn direction. This failure occurred at the exterior surface. The Z-yarn prevented the crack from spreading further.

In various studies, the stress-strain curves for different materials are similar for orthogonal 3D woven composites. Carbon fibre composites exhibit an initial linear region at a strain of approximately 0.6%, followed by a significant nonlinear response at 2.5–3.0% [89, 90, 92]. The same nonlinear response was observed for Kevlar/epoxy [102]. In the case of *glass fibre reinforced polymer* (GFRP), the curve is smooth with a kink developing at a strain of 0.3%, growing linearly until 1.4%, and then softening further till failure. Due to waviness, the initial and secondary moduli of Kevlar/epoxy and GFRP drop by 35–50% and 20–30%, respectively. The deflection angle typically falls between 4° and 10°.

In 3D orthogonal woven composites, the stress-strain curve under compression is almost linear before failure. When the impact of waviness on the compression properties of these composites was examined, it was discovered that the compression reduces as the Z-fibre fraction rises [103, 104]. In 3D orthogonal woven composites, a crimp angle of 20°–25° and minor waviness of about 1°–2° were also noted. It has also been investigated how the characteristics of these composites are affected by waviness [105].

Studies on the impact of the binder density on the modulus and tension stress of 3D orthogonal woven composites revealed an inverse relationship between the two quantities [106]. The weft density was investigated in relation to the characteristics of these composites, and it was discovered that this effect was stronger than that of the warp density [102]. In 3D orthogonal woven composites, different designs and densities can alter the direction and segregation of failure [107].

In this investigation, it was discovered that the failure strain is reduced by fibre deformation in glass/vinyl ester composites through Z yarn compression, whereas the modulus and stress in 3D orthogonal woven composites were virtually linear with an

increasing strain rate [108]. In a different study, it was found that the curves for in-plane compression are steeper than those for through-thickness, and that the modulus in carbon 3D orthogonal woven composites increases slightly before reaching a peak. High strain rates allowed energy to spread over a broad region of composite plates [109].

1.4. Biased Weaving and Multiaxial Composites

Methods of 3D weaving, as discussed above, orient fibres in just 3 mutually perpendicular axes, i.e. X, Y, and Z. Particularly for aerospace applications, yarns are required to be laid in a biased angle θ to the main warp line in addition to the warp and weft yarn sets for the improvement of the shear properties [36]. This requirement is satisfied by an additional set of yarns called biased threads which, although drawn in the warp direction, but traverse periodically in the width/weft direction to lie at a biased angle, as shown in Fig. 1.2. As these yarns are required to traverse width-wise, the conventional reed becomes an obstruction to the yarn movement. They can be incorporated in a fabric by the knitting, braiding, or weaving techniques. Out of these three methods, weaving provides superior structural integrity. To weave this kind of fabric, special looms and mechanisms are developed which eliminate the use of the conventional reed, and the yarn is beat-up by other elements. Many researchers have developed various methods and mechanisms to weave biased yarn on a surface as well as in sandwiched layers.

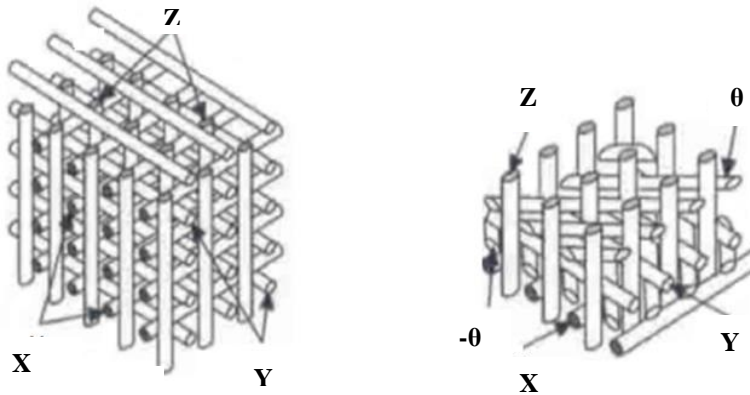


Fig. 1.2 Fibre orientations: a) orthogonal 3D weaving; b) biased weaving [39]

1.5. Weaving of Biased Yarns by Constructing a New Machine

As reported in some patent literatures, researchers have developed new machines where the fundamental weaving techniques are radically changed to incorporate biased yarns in three-dimensional woven structures.

Anahara and Yasui [58] have developed a multiaxial 3D weaving mechanism where the normal warp, bias and weft yarns are bound by binder yarns which are inserted vertically with a needle. Heald wires are eliminated, and, in their place,

smooth or threaded shafts are used. Normal warps are passed on smooth shafts, whereas biased yarns are passed on threaded shafts which are staggered vertically to separate layers instead of passing through heald eyes. The weft is inserted by a rapier which also does the beat-up as a reed cannot be used. The threaded shaft traverses the biased yarns along the fabric width.

Yet another way of indexing is by an endless belt carrying grooves through which the biased yarns are passed. A stepper motor rotates the belt, and biased yarns are indexed along the width of the fabric. As the biased yarns are in continuous rotation, the yarn feed also has to be in rotation.

The above system is further modified in a guide block array which is traversed by a shaft. They circulate along a rectangular path in one direction. Biased yarns are passed through these blocks, and the yarn supply is also rotated. This method incorporates the biased yarn in the sandwiched layers.

Bilisik and Mohamed [70] have developed a multilayer biased preform where tubes are used as guides to guide the warp yarns and index the biased fibres. The weft and Z yarns are inserted with a needle insertion system. The reed provides an obstruction to the biased yarn movement, so, weft insertion needles beat-up the inserted yarns to the cloth fell.

Biased yarns are woven on the surface, whereas warp yarns are sandwiched in the middle. 32 tubes of biased yarns are arranged in a box which indexes them periodically. Two such boxes are arranged above and below the warp surface which interchange their position once they reach at the selvedge. The biased yarn supply is also rotated to avoid yarn entanglement. The warp and biased yarns are staggered to form a permanent open shed. Z yarns are inserted to form a shed in which the weft yarns are inserted. Z yarns retract to bind all the yarns (warp, biased, and weft).

Uchida et al. [65] have developed a multiaxial weaving loom orienting yarns in five directions. The fabric has four layers +bias, -bias, warp, and weft. All the layers are locked by binders. Biased yarns are drawn through a rotating chain having the horizontal axis. This chain indexes the yarn by one unit during each weaving cycle, and the weft is inserted by rapiers into the permanent open shed. Z-yarns are inserted by special rapiers which insert the yarn in the vertical plane. This same assembly beats up all yarns till the cloth fell.

Mood GI [43] has developed four layer multiaxial 3D woven fabrics. This fabric has four fibre sets: +bias, -bias, warp, and weft. Biased yarns are sandwiched between the warp and the weft which interlace to bind all the yarns. Yarn traversing is done by a split reed and a Jacquard mechanism. Biased yarns are drawn from the creel in the sheet form and fed to special heddles connected to a Jacquard head. Biased yarns along with warp yarns are passed through a split reed which has 2 parts. The upper part is moveable, and it traverses width-wise, while the bottom part is stationary. Biased yarns which are to be traversed are selected by the jacquard head and positioned in the dents of the upper reed. Binder yarns are inserted by needles which are locked by weft yarns. Beat-up is done by an open reed.

A multiaxial weaving loom based on the sliding tube principle has been created by Nayfeh [72]. Warp, weft, and biased yarn sets make up a 3D woven fabric. The

yarns that have been biased are fed through a series of tubes that are positioned on grooves in a block. The tubes can slide along a path created by the adjacent blocks aligning. In the gap between the neighbouring blocks, the warp is conveyed. Weft yarns are inserted with a shuttle. Weft and bias move to the interlace through shed warp yarns which are formed. An open reed beats the threads till the fabric collapses.

1.6. Weaving of Biased Yarns on Modified Looms

Some researchers have modified the conventional weaving loom to incorporate a biased yarn in the regular 3D woven structure, as reported in patent literature.

Based on the lappet weaving principle, Ruzand and Guenot have created a multiaxial 3D weaving process and machine [61]. The bias yarns move across the width on either a single surface or both surfaces. On the two surfaces of the construction, the weft yarns and the warp binding yarns are woven together to hold them together. The warp and the weft are piled on top of one another to form sandwiched layers. This method, which uses pairs of lappet bars on either one or both sides of the fabric, was developed from lappet weaving. Until they reach the opposing fabric selvedge, each pair of lappet bars moves in the opposite way without changing the direction of a segment. The lappet's section separates as it approaches the selvedge, thus releasing the strands holding the guide and selvedge together. Transferred to the opposite side, the removed lappet segment is reattached to the lappet bar, and yarns are tied. Weft insertion is done with a rapier, and bias yarns are held in place by a selvedge-forming device.

Based on the multilayer narrow weaving principle, Bryn, Islam, and Lowery have created the multiaxial four-layer fabric [54]. The warp and weft yarn sets in the cloth cause bias. On this loom, different cross sections, such as pi, T, or +, can be woven. Biased yarns are constantly woven into the plain weave structure as they move from selvedge to selvedge throughout the fabric's width. An individual hook is used to insert the bias yarn set, traversing the biased yarns and moving them vertically to create a shed for the insertion of the weft.

The open reed weaving (ORW) technology developed by *Lindauer Dornier GmbH* is a novel technique which allows for the incorporation of additional thread systems into the fabric at varying angles, thus providing a more versatile and flexible fabric design [110]. The technology involves the use of a specialized reed that is unlike the conventional weaving reed. The ORW reed is equipped with alternating open and closed reed dents enabling the additional material, called *multi-axial fibre* (MAF), to be fed through the open dents and the warp threads to be guided through the closed dents.

The MAF is guided over an additional package of laying needles, which is lowered into the open reed dents. This allows for the multi-axial yarns to be incorporated into the fabric at discrete angles, thereby providing greater flexibility in the fabric design. The laying needle package can also be moved axially in the weft direction by using an additional linear actuator, which further enhances the versatility of the ORW technology.

1.7. Structural Health Monitoring of 3D Woven Composite Using Nanoparticles

SHM of composites refers to the use of sensors, actuators, and other devices to monitor the health and performance of composite structures in real-time. The goal of SHM is to detect and diagnose the potential damage or deterioration of composite materials and to provide early warning signs of a potential failure. This information is used to improve the maintenance and management of composite structures and to ensure their safety and reliability over time [3, 4, 12].

Non-destructive testing techniques, such as ultrasonic testing, radiography, thermographic testing, acoustic testing, and shearography testing, are used for the detection of damage in composite materials [27, 111]. These techniques have been found to be effective in detecting damage with an accuracy of up to 95% in some cases. However, they can be expensive, with costs ranging from several thousand to tens of thousands of dollars per test, depending on the complexity of the material and the required level of detail.

Integrating sensors into the composite material during its manufacturing process is a favourable approach, as it enables continuous online monitoring and can provide real-time data for predictive maintenance [112]. The most straightforward technique for integrating sensors is to incorporate optical fibres, metallic yarns, piezoelectric materials, yarns coated with conductive dyes, microcapsules, etc. into the fabric during the weaving process, or directly integrating the sensors into the composite structure [34, 113, 114]. The use of these sensors can provide strain data with a resolution of up to 0.1%, and it has been found to have a repeatability of $\pm 0.5\%$ under controlled laboratory conditions [1, 10].

In terms of using conductive nanoparticles, these have been found to be effective in detecting changes in electrical resistance with a sensitivity of up to 0.1Ω per unit strain [19, 115, 116]. The use of conductive nanoparticles dispersed in the matrix or as a conductive coating on the surface of the composite material has been found to provide strain data with a resolution of up to 0.05% [7, 18]. These sensors have been found to have a repeatability of $\pm 0.2\%$ under controlled laboratory conditions [19].

Several types of nanoparticles have been used for SHM of composites, including:

1. CNT [16];
2. Graphene nanoplatelets [117];
3. Nano silver particles [114].

These nanoparticles are denoted by unique mechanical, electrical, and thermal properties that can be utilized in composites to enhance the sensing capabilities of SHM systems. The choice of nanoparticles for a particular SHM application will depend on the specific requirements of the composite structure and the desired monitoring capabilities. In this research, carbon nanotubes and MXene nanoparticles were used for SHM, which shall be explained further in detail.

1.7.1. Structural health monitoring using carbon nanotubes

CNT has been widely studied as potential materials for use in composite materials for SHM due to their unique mechanical, electrical, and thermal properties. Studies have shown that CNT can be successfully incorporated into various composite materials to improve their sensing capabilities. For instance, CNT has been used to develop electrical resistance sensors for detecting changes in the mechanical properties of composites [23], [118], [[119]. The high electrical conductivity as well as the high aspect ratio of CNT make them well-suited for this type of application [120].

Additionally, CNT has been used to develop composite materials with enhanced thermal conductivity for SHM applications [121]. The high thermal conductivity of CNT can be used to detect temperature changes in the composite material, which can indicate potential damage or deterioration [122].

The electrical conductivity of CNT in epoxy resin is influenced by several factors, such as the content of CNT in the matrix, the size of the composite sample, the method of dispersion, the agglomeration of CNT, etc. [14]. In general, a higher content of CNT results in a lower resistance of the network, with a threshold content of around 0.7–0.8 required for percolation. At low CNT contents, the resistance of the CNT network can be as high as $10^6 \Omega \cdot \text{cm}$, while, at high CNT contents, the resistance can be as low as $10^2 \Omega \cdot \text{cm}$. The resistance of the CNT network can also change in response to external strains and damage accumulation, with a strain sensitivity of around $10^3 \Omega/\%$ [123].

The preparation of multi-scale all-carbon fibres can be classified into two approaches: indirect methods and direct methods. Indirect methods involve depositing pre-formed carbonaceous nanofillers onto the carbon fibre surface, while direct methods produce carbonaceous nanofillers *in situ*. Although physical interactions are expected in indirectly prepared fibres, some approaches involve grafting procedures to enhance the adhesion between the carbon fibre and nanoparticles.

To disperse CNT in composites, two commonly used methods are *chemical vapour deposition* (CVD) [40, 124], which is a direct method, and *vacuum-assisted resin transfer moulding* (VARTM), which is an indirect method. CVD involves growing the CNT on the composite substrate, and it has been shown to enhance the mechanical properties of composites significantly, with an increase in the tensile strength of up to 20% [125]. On the filtration of CNT particles due to the difference in the flow properties of the nanotubes and the resin, resulting in agglomerated CNT particles that can be up to 50 μm in size [126, 127].

Below, some of the common methods to incorporate CNT in VaRTM process by the indirect method are listed.

1. *Dispersion*: In this method, CNTs are dispersed in a polymer matrix by using mechanical methods, such as high-speed mixing, chemical methods, such as functionalization or sonication. The aim is to distribute CNT evenly throughout the matrix to ensure maximum reinforcement [128, 129].
2. *Functionalization*: This involves chemically modifying CNTs to improve their compatibility with the polymer matrix. This can involve functionalizing the surface

of the CNT with chemical groups that can bond with the polymer, or making changes to the polymer matrix to improve adhesion [130, 131].

3. *Solution Blending*: This method involves dissolving CNTs in a solvent and then blending the solution with the polymer. The solvent is then evaporated, leaving behind a composite material. This method is often used when the polymer and CNT are not compatible with each other in their solid state [131, 132].
4. *Intercalation*: In this method, CNT are inserted between the layers of a layered material, such as clay or graphite. CNTs are intercalated into the layered material, which enhances the mechanical properties of the composite. This method is often used to produce high-strength, lightweight composites [132, 133].

CNTs in epoxy resin conduct electricity through quantum tunnelling and contact resistance [121]. Quantum tunnelling is a quantum mechanical phenomenon where electrons can transfer through a potential barrier. In the context of carbon nanotubes (CNT) in epoxy resin, quantum tunnelling occurs when electrons transfer between CNT structures with a gap in the order of magnitude of 1 nm. This leads to electrical conductivity in the CNT network [134].

Contact resistance is another factor contributing to the electrical conductivity of CNT in epoxy resin [123]. It occurs due to the overlapping of CNT, thus providing a continuous path for electrical conductivity. The resistance of the CNT network changes with the change in the dimensions of the composite and can be attributed to various mechanisms, such as the change in dimension, the piezoresistance of individual CNTs in response to applied strain, damage accumulation, and change in quantum tunnelling and contact resistance.

1.7.2. Structural health monitoring using MXene nanoparticles

MXene nanoparticles have been gaining attention as potential materials for the use in SHM of composite materials. A literature review of MXene nanoparticles in composite materials for SHM shows that they are denoted by several unique properties which make them attractive for use in this field.

MXene nanoparticles are 2D materials consisting of transition metal carbides or nitrides. MXene nanoparticles, with their two-dimensional (2D) structure of titanium carbide ($Ti_3C_2T_z$) and surface functional groups (-O, -OH, and/or $-F_{2,3}$) which is denoted by T_z at the end of the formula, demonstrate exceptional mechanical and electrical properties [135]. With a tensile strength of 590 MPa (980 nm thick film) [31] and a Young's modulus ranging between 500–800 GPa [32], these particles are produced through the selective etching of elements from the three-dimensional (3D) MAX phase [28]. The weak van der Waals forces between the nanoflakes make them ideal for strain sensing applications [30], and they can be homogeneously dispersed in a matrix through techniques such as melt blending, *ex-situ* blending [136], and *in-situ* polymerization [137].

MXene conducts electricity through quantum tunnelling and contact resistance [138]. The quantum tunnelling effect allows for the transfer of electrons between the nano flake structures, with a gap of around 1 nm, while contact resistance occurs due to the overlapping of the MXene particles providing a continuous path for electrical

conductivity. Most research in the structural health monitoring domain has been focused on planar surfaces, but, in practical applications, composite panels often have complex shapes and geometries [139]. The general steps to manufacture MXene nanoparticles are as follows:

1. *Synthesis of the precursor material*: the first step in the manufacturing of MXene nanoparticles is to synthesise the precursor material, which is usually a layered transition metal carbide or nitride, such as Ti_3C_2 . This is typically done by employing a solid-state reaction in a high-temperature furnace [140, 141].
2. *Exfoliation*: the second step involves exfoliating the layered precursor material to produce individual nanoscale sheets. This can be done by using either chemical or mechanical methods. Chemical exfoliation involves using a solvent or an etching solution to dissolve the layers of the precursor material and separate them into individual sheets. Mechanical exfoliation involves using a shear force, such as sonication or grinding, to separate the layers of the precursor material [142, 143].
3. *Functionalization*: the final step in the manufacturing of MXene nanoparticles is functionalization, which involves modifying the surface of the nanoparticles to enhance their properties and behaviour. This can be done by using chemical methods, such as attaching functional groups, or physical methods, such as coating the surface with another material [144, 145].

One of the key advantages of MXene nanoparticles is their high electrical conductivity. This makes them well suited for use in electrical resistance-based SHM systems [26]. MXene nanoparticles have also been shown to improve the thermal conductivity of composite materials, which can be useful for temperature-based SHM systems [29].

Another advantage of MXene nanoparticles is their ability to enhance the mechanical properties of composite materials. This makes them well suited for use in composite materials that are subjected to high levels of stress and strain [146].

Several studies have shown that MXene nanoparticles can be effectively incorporated into composite materials to enhance their SHM capabilities. For example, researchers have used MXene nanoparticles to develop electrical resistance sensors for detecting changes in the mechanical properties of composite materials [24]. Some of the more common techniques to incorporate MXene nanoparticles in composites are as follows:

1. *Solution infiltration*: In this method, MXene particles are added to a polymer resin and then infiltrated into the fibre reinforcement by using a vacuum or pressure process. The aim is to ensure good dispersion and distribution of the MXene particles throughout the composite. This method can be used to produce composites with improved mechanical, electrical, and thermal properties [147, 148].
2. *Melt blending*: In this method, MXene particles are added to a polymer resin and then melted and blended with the fibre reinforcement. The process involves heating the mixture of the MXene particles, polymer resin, and fibre reinforcement to a temperature above the melting point of the polymer resin, and then mixing the components to form a homogeneous composite material. This method is often used

to produce composites with improved thermal stability. The typical polymers deployed are polypropylene [30] and polylactic acid [149].

3. **Electrospinning:** In this method, MXene particles are added to a polymer solution and then electrospun with the fibre reinforcement to produce a nanocomposite material. Electrospinning involves the application of an electrical field to the polymer solution, which causes it to form nanofibres. The MXene particles are embedded in the nanofibres, which results in a composite material with improved mechanical and electrical properties [150].
4. **Compression moulding:** In this method, MXene particles are mixed with a polymer resin and then compression moulded with the fibre reinforcement. The process involves applying high pressure and temperature to the mixture of the MXene particles, polymer resin, and fibre reinforcement, which results in a homogeneous composite material. This method is often used to produce large parts with complex shapes. The most common type of polymers used are polyurethane [151], polystyrene [152], and polyvinyl fluoride [153].

Thus, in conclusion of the literature review on MXene nanoparticles, we can suggest that they are efficient in detecting damage and strain when embedded in composite structures. In addition, they are also able to conduct heat, which makes them useful in manufacturing multifunctional composites.

1.8. Simulation of Impact and Tensile Loading on Composites

Although the woven fibre laminated composites are denoted by great specific strength, specific stiffness, and fatigue resistance, they can nevertheless be damaged by tensile and impact loads that have low velocities. Impact loading can result in complicated damage, such as matrix cracking, delamination, and fibre breaking. Tensile loading can result in matrix cracking, matrix debonding, and fibre pullout. In comparison to costly experimental procedures, the *finite element method* (FEM) and the *finite element analysis* (FEA) are thought to be the most realistic and effective methods for simulating and predicting the complex damage behaviour of these composites under impact and tensile loads. They can also increase the efficiency of the study. As a result, FEA is the method of choice for researching how these composites respond to the impact and tensile damage.

The duration of an impact between two bodies is very short; typically, in the order of microseconds. During this time, a large amount of energy is transferred between the bodies, thus causing significant deformation and, potentially, damage [67]. To investigate the transient response of the impact, certain assumptions are often made to simplify the analysis. These assumptions may include the following points:

1. Frictionless contact between the impactor and composite structure. This means that no energy is lost due to frictional forces at the contact interface.
2. Neglecting the damping effect in the composite structure. This means that no energy is dissipated due to internal friction within the material.

3. Ignoring the effect of gravity during the impact period. This may be a reasonable assumption if the impact is occurring in a microgravity environment or if the duration of the impact is very short.
4. Assuming rigid body behaviour for the impactor. This means that the impactor is treated as a solid object with no internal deformation.

These assumptions can simplify the analysis of the impact response, but they also limit the accuracy of the results. In reality, there will always be some level of friction, damping, and deformation during an impact.

During the loading phase of an impact, the contact force typically follows the *Hertzian contact law* [154, 155] which relates the contact force to the amount of deformation at the contact interface. This law is based on the assumption that the bodies are elastic and that the contact area is small compared to the overall size of the bodies.

In addition to the Hertzian contact law, other expressions have been proposed to calculate the contact force during an impact. One such expression was proposed by Tan and Sun [156], which takes into account the nonlinearity and viscoelasticity of the materials involved. This expression can be useful for predicting the behaviour of composite structures which exhibit complex mechanical behaviour during an impact. The following equations are used to calculate cases of loading and unloading, respectively:

$$F_c = k \alpha^{1.5}, \quad (1.1)$$

$$F_c = F_m \left(\frac{\alpha - \alpha_0}{\alpha_m - \alpha_0} \right), \quad (1.2)$$

where F_c is the contact force, F_m is the maximum contact force reached during the impact, α_m is the maximum indentation which corresponds to F_m , α_0 is the permanent indentation from the loading/unloading cycle, k is the modified Hertzian contact stiffness.

1.9. Finite element modelling of composite materials

When composite components experience stress and strain beyond their capacity, it results in material failure. To prevent such failures and ensure the longevity and safety of the components, materials are designed by using various theories which help understand their behaviour and properties. These theories also aid in studying the different types of stress and strain generated in the material. A failure occurs when a material is unable to perform its intended function, which includes fracture, buckling, and matrix cracking.

Different theories, such as the *maximum stress theory*, *maximum strain-theory*, *Tsai-Hill theory*, *Tsai-Wu* [157] and *Hashin damage theory* [158] are used to study the properties of composite materials. The maximum stress theory, also known as the first ply failure theory, is a widely used theory for predicting the failure of composite materials under uniaxial stress conditions [157]. On the other hand, the maximum strain theory assumes that a failure occurs when the maximum strain is reached in the composite ply [157]. According to this theory, a failure in a composite material occurs

when the maximum stress in any individual ply exceeds the strength of that ply. It assumes that the stress distribution within the ply is uniform and that the plies are oriented in a specific direction. It also assumes that the strength of the plies is independent of their orientation with respect to the applied load. The Hashin failure criterion is a widely used composite failure criterion which takes into account four separate modes of failure. These modes of failure include fibre tension, fibre compression, matrix tension, and matrix compression. Each of these failure modes is predicted by a separate equation. It is often used in conjunction with other failure criteria to more accurately predict the failure of composite materials.

Ansys® is general purpose simulation software which adapts explicit dynamics and *LS Dyna*™ as solver for composite impact problems [159, 160]. To solve the problems, it is required to input the following categories of data:

1. **Material properties:** Material properties must be identified for both the impactor and the target object. This includes the density, Young's modulus, Poisson's ratio, and the yield or failure strength. The materials can be modelled as isotropic, orthotropic, or anisotropic.
2. **Initial and boundary conditions:** The initial conditions for the impactor must be specified, including the impact velocity, acceleration, and orientation. The boundary conditions for the target object must also be specified, such as a clamped or simple support. These conditions can significantly affect the results of the simulation and should be chosen carefully to accurately represent the physical system being modelled.
3. **Contact conditions:** The type of contact and the friction coefficient must be defined between the impactor and the target object.

In addition to these three categories of input data, other factors, such as the mesh density, the time step size, and the solver settings can also impact the accuracy and efficiency of the simulation. Therefore, it is important to carefully choose all the input parameters and thoroughly validate the simulation results against experimental data or other analytical solutions [161].

The initiation criteria in ANSYS are used to determine when and where a material failure is expected to occur. Each criterion has its own set of equations defining a specific failure mechanism. The available initiation criteria in ANSYS, including the maximum strain, the maximum stress, Hashin, Puck, LaRC03, and LaRC04, can be used for different types of materials and loading conditions [162, 163].

In addition, ANSYS allows users to define up to nine additional criteria as user-defined initiation criteria. This allows users to customize the failure criteria to their specific needs and materials. However, only the Hashin criterion is compatible with the progressive damage analysis (PDA) method in ANSYS [160].

The Hashin criterion is based on the concept of micromechanics. It calculates the stress and strain components in each direction of a material to determine if any direction exceeds the failure criteria. The PDA method in ANSYS allows for a more detailed analysis of the failure process by simulating the progressive damage and crack propagation in the material.

The impact damage behaviour of a composite panel with a circular hole using the *ANSYS Workbench* by modelling the panel as a three-layered composite using the shell element and simulating the impact using the explicit dynamics method showed that the damage propagation was influenced by the material properties of the composite, the impact energy, and the impact location [164, 165].

In another study, the impact behaviour of a sandwich panel with a honeycomb core using the *ANSYS Workbench* was investigated. The panel was modelled by using solid elements, whereas the impact simulation was using the explicit dynamics method. The authors found that the impact energy, the impact location, and the core density significantly affected the damage propagation and the failure modes of the panel [166].

1.10. Summary of the Literature Review

The summary of the literature review on 3D woven composites, SHM of composites using CNT and MXene nanoparticles, multiaxial composites and simulation can be generalized with the following points:

- 1 3D woven composites may possess improved mechanical properties compared to the traditional 2D laminates. This is because the fibres in a 3D woven composite are interlocked in three dimensions, which can improve the load-bearing capacity and resistance to delamination and other types of failure. However, the structural health monitoring of 3D woven composites is not explored as compared to laminated composites.
- 2 Structural health monitoring of laminated composites by such nanoparticles as CNT and MXene has been researched in depth. However, there is a significant lack of research when it comes to the structural health monitoring of 3D woven composites embedded with nanoparticles. The main reason of the current state is that the manufacturing of 3D woven composites by the resin infusion method poses process difficulties for the dispersion of nanoparticles in a composite.
- 3 The methods to manufacture multiaxial preforms have been surveyed. It has been observed that the presently available methods require complex mechanical changes in the existing weaving loom to manufacture a multiaxial preform. Such machines are slow and inefficient to produce multiaxial preforms in large quantities. Thus, a research gap exists in the method of manufacturing multiaxial preforms and the ensuing composites. In addition, significantly less research has been carried out to study the mechanical properties of multiaxial composites. Thus, a gap in research also exists in terms of studying the bias fibre behaviour in multiaxial composites.
- 4 The numerical simulation of an impact and the tensile loading of composites in Ansys have been well established. The software offers a comprehensive library of materials, composite pre- and post-processing modules, a failure criteria package, and static-dynamic loading simulation in explicit dynamics. It also supports user-

defined material properties and function(s). However, significantly less research data is available to model the mechanical properties of multiaxial composites in FEA. Thus, there exists a research gap to develop a FEA simulation model of multiaxial composites and their behaviour under tensile and impact loading conditions.

Based on the research gaps identified during the literature review, in this dissertation, the technology and the processes to manufacture a multiaxial composite and to incorporate CNT and MXene nanoparticles into a 3D woven composite have been designed and developed. The mechanical characterization of composites in terms of the tensile, flexural, fatigue and impact loading, the efficiency of the SHM of self-sensing composites and the FEA of multiaxial composites have also been investigated.

2. MATERIALS AND METHODS

2.1. Infusion of CNT in 3D Woven Glass Fibre Composite¹

2.1.1. Preparation of CNT masterbatch

The initial stage in diffusing CNT into composite is to create a masterbatch, an epoxy CNT combination that may be further diluted to reach the desired concentrations. The NCTM 7000 multi-walled CNT was purchased from *Nanocyl*® (Belgium) in the powder form. The manufacturer's datasheet indicated that the multiwalled CNT made by using the catalytic chemical vapour deposition technique had an average diameter of 10 nm. *Sika GmbH*® (Germany) provided the epoxy resin and the hardener for the *Biresin CR-122 Bisphenol F*.

Solvent evaporation was used to create the masterbatch. CNTs do not mix well with bisphenol F epoxy. So, in order to make the masterbatch, 100 mL of hexane and 0.13 g of CNT powder were combined and sonicated for 5 minutes. After that, 6.37 g of epoxy resin was added and mechanically mixed into the mixture until the hexane solution became clear once more. To generate a mixture of epoxy with evenly scattered 2 wt% CNT particles, the resulting epoxy-CNT sediment¹ was collected and degassed in a vacuum at 50 °C for an hour.

2.1.2. Composite manufacturing

TexTech Industries® (USA) supplied an orthogonal E glass fabric. The fabric had an overall fibre content of 51 vol%, with 49 wt% X fibres, 48 wt% Y fibres, 3 wt% Z fibres, and a total thickness of 2.2 mm, as per the supplier's datasheet which is presented in Table 2.1.

Table 2.1. Orthogonal 3D woven fabric data

Parameter	Machine Direction (warp)	Cross Machine Direction (weft)
Yarns	5 (2 binders, 3 stuffers)	2
Thread density	8.26/cm	6.3/cm
Number of layers	3	4
Yarn material	E glass	
Aerial density (g/m ²)	3200	
Weave type	plain woven orthogonal	

The matrix to be used was bisphenol F resin with an amine hardener. 3D woven composites were manufactured by using vacuum infusion with three different methods, and the resulting samples were given unique codes in the format of S_iG_n (where 'i' is the method, and 'n' is the group number), as shown in Table 2.2.

¹ The material presented in this chapter has been published in [126]

Table 2.2. Sample codes and manufacturing methods

Method and sample code	Method 1		Method 2	Method 3	
	S ₁ .G ₁	S ₁ .G ₂	S ₂	S ₃ .G ₁	S ₃ .G ₂
Dimensions (mm)	300 × 250	300 × 250	100 × 100	300 × 300	300 × 300
CNT dispersion process	Cast	Cast	Infusion	Vacuum transfer	Vacuum transfer
Vacuum pressure (kPa)	101.3	101.3	101.3	101.3	30.4
Notch 'V' shaped	inside CNT film	outside CNT film		not notched	

In method 1, pure epoxy was infused into the 3D woven fabric by using the traditional VARTM procedure, and the fabric was then allowed to cure for 12 hours at room temperature. After that, a doctor blade was used to cast a 0.25 weight percent CNT in the epoxy resin film onto the 3D weaved composite. The 2 wt% CNT masterbatch was diluted with epoxy resin to produce CNT mixes with electrical resistance of the order of $10^3 \Omega$. The cast was 50 mm in length and 100 μm in thickness. The castings were post-cured in an oven at 80 °C for 5 hours after being allowed to solidify at room temperature for 12 hours.

In method 2, a 3D woven fabric was infused with a mixture of pure epoxy and 0.25 wt% CNT filler by using the VARTM process. The composites were cured for 12 h at room temperature and post-cured at 80 °C for 5 h.

As seen in Fig. 2.1a, method 3 involved directly impregnating the CNT on the fibres in a perpendicular direction. It was decided to employ porous nylon knitted spacer fabric to absorb the 0.25 wt% CNT and epoxy combination. To transfer the CNT onto the fibre surface, vacuum pressure was used during the layup, and it was then allowed to cure for 12 h. Sample S₃.G₁ was given 101.3 kPa vacuum pressure, while sample S₃.G₂ was given 30.4 kPa vacuum pressure to regulate the infusion of CNT. The resin was infused into the orthogonal 3D woven fibre reinforcement by using the traditional VARTM process after CNT curing for 12 h. The finished composite was then post-cured at 80 °C for 5 h. By comparing the filtration of CNT by dry and impregnated peel ply sheets, it was discovered to be 1.12 g.

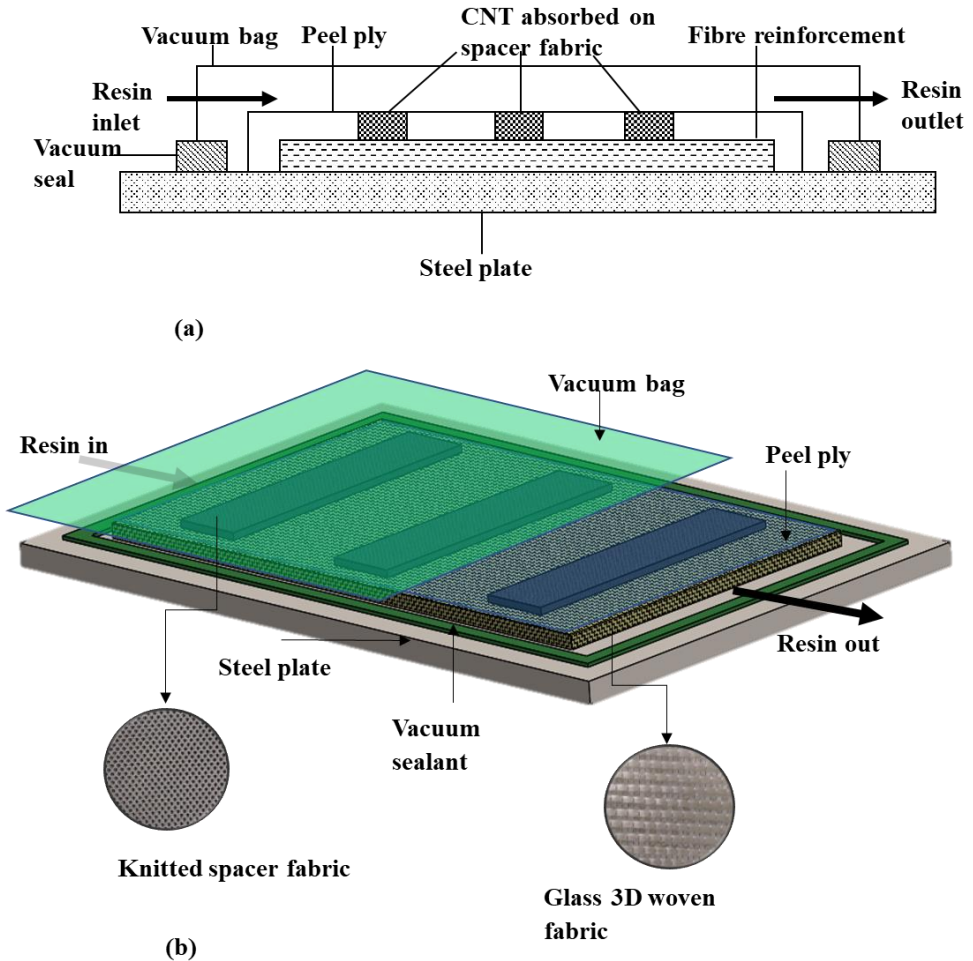


Fig. 2.1 Modified VARTM processes: (a) stacking sequence in layup, (b) schematic of the process [126]

2.1.3. Microscope characterization

Composite panels of S_2 and $S_3.G_2$ were cut into $15\text{ mm} \times 30\text{ mm}$ pieces and examined under an optical microscope to further analyse the distribution of CNT in the composites. The samples were put on a sodium lamp backlight, which made the CNT opaque to the sodium light and the glass fibres infused with epoxy transparent to the sodium light. For SEM characterisation, the $S_3.G_1$ samples were cut into $5\text{ mm} \times 5\text{ mm}$ pieces in the warp direction by using an *FEI Quanta 200 FEG*.

2.1.4. Tensile testing of composite samples

A waterjet cutting device was used to cut the specimens from method 1 into rectangular pieces measuring $250\text{ mm} \times 25\text{ mm}$. Three groups were created from these specimens. $S_1.G_1$, $S_1.G_2$, and $S_3.G_1$. Notches were cut into the $S_1.G_1$ and $S_1.G_2$

specimens in order to better understand the nature of the CNT sensor signal during the absorption of the fracture energy. The $S_1.G_1$ specimens were cut with a 1 mm V-shaped notch at the edge to serve as a damage initiation point inside the CNT film. As depicted in Fig. 2.2, a comparable notch was cut on the edge of the $S_1.G_2$ specimens to start damage outside the CNT layer.

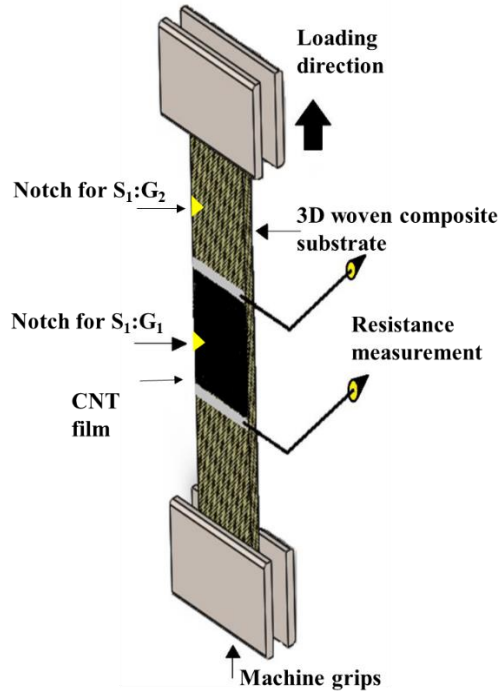


Fig. 2.2 SHM of 3D woven composite during tensile loading [126]

The tensile and electrical characteristics of the samples were unaffected by the presence of the notches. This was done in such a way that the structural integrity of the sensor, which is made up of a network of individual CNT rather than a bulk substance, would not be compromised by minor damage.

On the other hand, group $S_3.G_1$ specimens were not notched. Five specimens were made for each group in order to ensure the repeatability of the results. By using conductive thermoplastic PLA combined with CNT, copper wires were connected.

The *Adamel® DY36™ UTM* machine, which has a load cell capacity of 50 kN, was used to test the composite samples in compliance with ISO 527-4 guidelines. A uniaxial tensile load is given to the sample in accordance with the ISO 527-4 standard test procedure to assess the tensile properties of polymer matrix composite materials. To maintain an even loading rate across all the samples, the machine's crosshead speed was adjusted to 2 mm/min. The stress values were calculated by dividing the measured force with the cross sectional area of the composites, whereas the strain values were captured by an extensometer mounted on the test samples during testing.

The specimens were directly held by machine grips without the use of any tabs, thereby ensuring that the electrical characteristics of the CNT network were precisely monitored during the tensile loading. The sample and the grips were separated by layers of insulating sandpaper to avoid any electrical contact that would have impacted the values obtained during the measurements.

Throughout the tensile loading, an *IR 3000 Bluetooth* data acquisition system with a *Fluke® 287 RMS™* multimeter was used to continually measure the electrical resistance of the CNT network. Two probes were placed on the surface of the composite material at known distances from one another, and the measurements were taken by using this technique. After that, Ohm's law was used to compute the electrical resistance.

To establish a relationship between the applied strain and resistance, the statistical correlation coefficient and the gauge factor (*GF*) were calculated. The statistical correlation coefficient is a measure of the strength of the relationship between two variables, in this case, the applied strain and the resistance of the CNT network. The gauge factor is defined as the ratio of the relative change of absolute resistance to strain in the composite given by the following equation:

$$GF = \frac{\frac{\Delta R}{R_0}}{\varepsilon}, \quad (2.1)$$

where ΔR and R_0 are the change in resistance and the initial resistance, respectively, whereas ε is the tensile strain.

It is an important parameter to determine the sensitivity of the CNT network to the applied strain, and it can be used to optimize the design of the composite material for specific applications.

2.1.5. Flexural testing of composite panels

The 3-point bending test was performed on samples $S_3.G_1$ and $S_3.G_2$ to ascertain the flexural characteristics of the composite material according to ISO-14125 test standards. A *Tinius Olsen®* machine with a 10 kN load cell capacity was used for the testing. The materials were prepared by cutting them into strips that were 80 mm × 15 mm in size before the testing. The samples were then set up in a beam-like configuration on two bottom rollers with a diameter of 10 mm and a span length of 64 mm, as illustrated in Fig. 2.3.

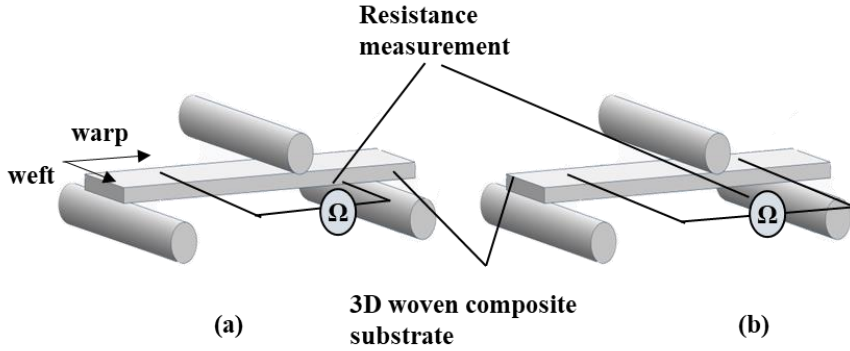


Fig. 2.3 Composite samples flexural loading and resistance measurement schematics: a) through-thickness, b) single surface [126]

A top roller with a 10 mm diameter that was placed precisely in the middle of the span length applied the bending force on the samples. To establish a constant loading rate across all the samples, the force was delivered at a speed of 1 mm/min. All the rollers were taped with an insulating material to avoid any electrical contact with the specimen.

$S_3.G_1$ and $S_3.G_2$ were evaluated on 5 samples each to ensure that the results were repeatable. This made sure that any variability of the results could be reduced, and the accuracy of the test results could thus be increased.

To measure the electrical properties of the composite material during the flexural testing, copper wires were soldered onto CNT castings, and silver paste was applied to the electrodes in order to decrease the contact resistance. This ensured that the electrical resistance measurements were accurate and consistent throughout the testing process.

The resistance values were measured and logged by using a two-probe technique while employing the *Fluke® 287 RMS™* multimeter with an *IR 3000 Bluetooth* data acquisition system. With this technique, two probes were placed on the composite material's surface at predetermined distances from one another, and the electrical resistance between them was measured. To enable the detection and analysis of any changes in the electrical characteristics of the CNT network, the resistance values were continually tracked during the testing process.

As illustrated in Figs. 2.3a and 2.3b, the electrodes were positioned across the sample thickness for $S_3.G_1$ and over the same surface for $S_3.G_2$. In a standalone flexural test, tensile stress and compressive stress was applied to the conductive CNT network of sample $S_3.G_2$. The sample's stress σ_f in MPa and strain ε_f in mm/mm was calculated with the following equations

$$\sigma_f = \frac{3FL}{2wt^2}, \quad (2.2)$$

$$\varepsilon_f = \frac{6st}{2L}, \quad (2.3)$$

where F is the force in kN, L is the span length of the specimen in mm, w is the width of the specimen in mm, t is the thickness of the specimen in mm, s is the deflection in mm.

2.2. Doping of MXene Nanoparticles on T-profile Composite²

2.2.1. Preparation of MXene nanoparticles

$Ti_3C_2T_z$ MXenes were synthesized from the Ti_3AlC_2 MAX phase obtained from MRC in Kiev, Ukraine. The MAX phase was etched by using a mixture of hydrochloric acid (*Merck*®, Germany) and lithium fluoride (*Sigma Aldrich*®, Germany) to produce $Ti_3C_2T_z$ MXenes.

In order to initiate the synthesis, MAX phase was added to a mixture of LiF/HCl and stirred for 24 hours at room temperature. This process led to the formation of a multilayer MXene sediment at the bottom of the container. The sediment was further delaminated by using 99 wt.% LiCl (*Sigma Aldrich*®, Germany) to obtain the desired $Ti_3C_2T_z$ MXene.

The resultant solution was then washed with deionized water to adjust the pH before being centrifuged at 3500 rpm for 10–15 times to eliminate any contaminants. Up until the supernatant's pH hit 6.5, the solution was repeatedly washed. This made sure that there were no acidic residues left behind that might have affected the $Ti_3C_2T_z$ MXene's functionality.

The concentration of $Ti_3C_2T_z$ MXene in the supernatant was measured and found to be 0.335 mg/mL. To increase the concentration, the solution was centrifuged to obtain a higher concentration of 3.3 mg/mL. This high concentration was necessary to achieve a resistivity in the order of $10^5 \Omega$. 5 layers of MXene were spread on a glass slide, gold-coated and subjected to a 15 keV electron beam under SEM. The partially delaminated MXene flakes with sizes ranging between 1–10 μm can be observed in Fig. 2.4a. A close-up view of a single-stack of MXene flake of a size of $2.5 \times 5 \mu\text{m}$ could be observed in Fig. 2.4b.

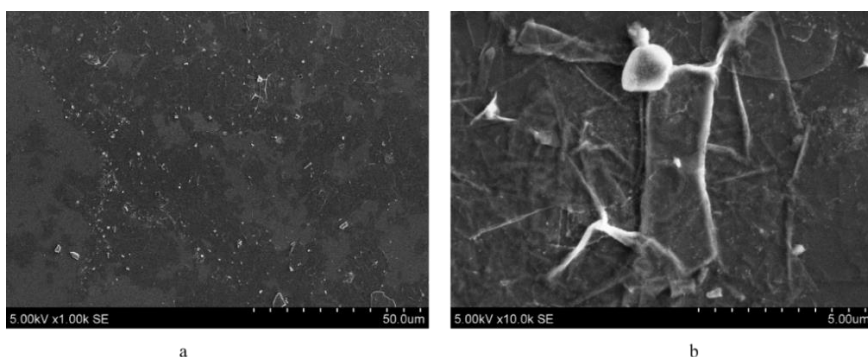


Fig. 2.4 Scanning electron microscope analysis of MXene: (a) partially delaminated scattered MXene flakes, (b) single MXene flake [139]

² The material presented in this chapter has been published in [139]

2.2.2. Manufacturing of T-profile composite

The single layer fabric T-profile preform was woven on an 8-head shaft dobby loom by using shuttle insertion. The preform was made by weaving glass rovings of 300 tex in a specific draft and denting plan as shown in Figs. 2.5a and 2.5b, respectively. The T-profile was woven in a folded form to ensure the proper alignment and to achieve the desired shape.

The base of the T-profile preform was created by using plain weave, while maintaining a constant value of 8 threads per centimetre for both the warp and the weft. The design shown in Fig. 2.5a was woven to create the desired T-profile shape. This design provided the necessary stability and rigidity to the preform, while also ensuring that the preform was lightweight and easy to handle.

To further strengthen the preform, two additional glass rovings were threaded at the base section, near the junction of the T-profile, as shown in Figs. 2.5b and 2.5c. These additional rovings served as reinforcements providing extra support to the preform and preventing any potential failure points.

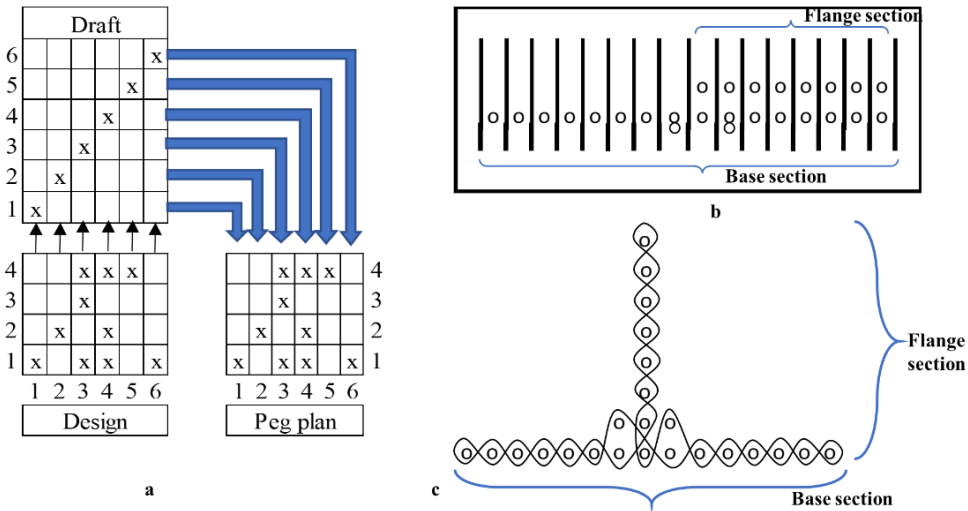


Fig. 2.5 Weaving of T-profile: (a) weave design, draft and peg plan, (b) denting plan, (c) warp cross sectional view of T-profile [139]

To manufacture the composite with the woven T-profile preform, *Biresin CR-122 Bisphenol F* epoxy resin and an amine hardener supplied by *Sika GmbH*® (Germany) were chosen as the matrix. The matrix was applied manually to the preform which had been placed in a metal mould. A layer of a perforated plastic sheet, and polyester non-woven fabric was placed on top of the wet preform to absorb the extra resin. The application of the matrix was done carefully to ensure that all fibres were fully impregnated with the matrix material.

To ensure complete impregnation of the matrix material, the wet preform was then subjected to 101.3 kPa vacuum pressure for 3 hours. The extra resin was absorbed by the non-woven fabric.

The preform was then cured at room temperature for 24 hours. During this time, the matrix material underwent a chemical reaction, thus hardening and bonding with the fibres. After the initial curing, the composite was post-cured in an oven at 80°C for 5 hours to ensure complete cross-linking and further improve its mechanical properties. This final curing step was necessary to achieve the desired strength and stiffness of the composite.

Argon-oxygen plasma was used as the initial treatment for the composite T-profile which has a thickness of 1 mm. It was sliced into the dimensions depicted in Figs. 2.6a and 2.6b after plasma treatment. Then, by using an airbrush with a 0.4 mm diameter nozzle and a compressor with a 0.1 mL/s paint yield (*Sparmax HB-040*TM and *DC-25X*TM 2.07 bar compressor from *Anest Iwata Sparmax Co.*[®], Taiwan), the T-profile was sprayed with 10 layers of MXene.

Each layer of MXene was sprayed for 10 seconds at a distance of 15 cm from the preform in a 250 mm² area. This area was chosen so that the MXene layer would retain the effective resistivity and the machine grips would not touch the conductive layer. After each layer had been applied, it was dried at 60°C by using an air dryer. This ensured that each layer was properly adhered to the T-profile and allowed for the gradual build-up of the MXene layers, as shown in Fig. 2.6b.

The use of plasma treatment prior to the application of the MXene layers was essential in improving the adhesion between the composite material and the MXene layers. Argon oxygen plasma was applied at the flange section of the composite to increase the hydrophilicity of the surface and aid in better adhesion of MXene dispersion in water. The use of an airbrush with a small diameter nozzle allowed for precise application of the MXene layers, thereby ensuring even coverage across the surface of the T-profile.

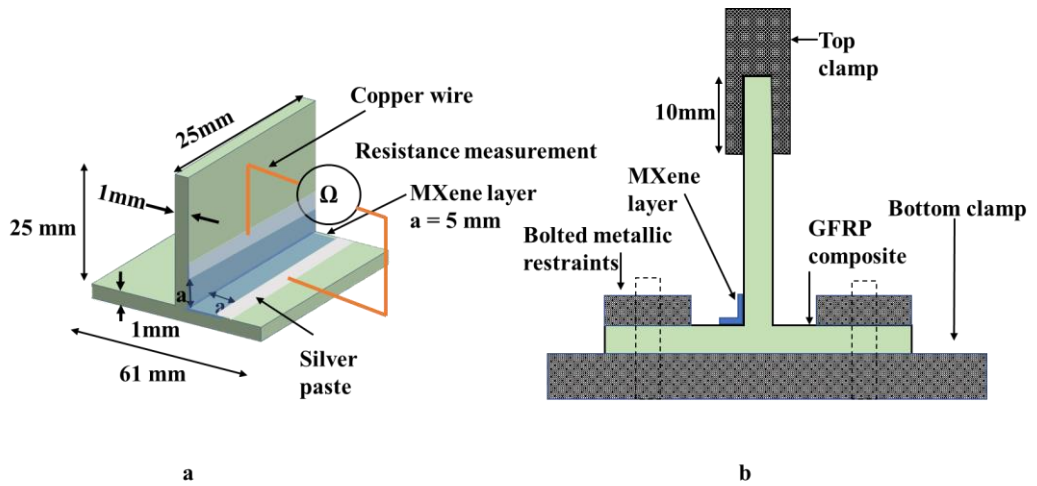


Fig. 2.6 3D woven composite T-profile: (a) specimen dimensions, (b) experimental setup for tensile and fatigue loading [139]

2.2.3. Tensile testing of T-profile composite

To evaluate the behaviour of the composite material under tensile load, five specimens were cut to dimensions as shown in Fig. 2.6. To conduct the tensile testing, an *Instron ElectroPuls E10000TTM* machine with a testing speed of 2 mm/min and load cell capacity of 10 kN was used. The specimens were mounted as shown in Fig. 2.6b. The base section of the composite was bolted to the bottom clamp with electric insulating tape, and the flange section of the composite was gripped in the top clamp with electric insulating sandpaper in order to reduce slippage. These measures ensured that the specimens were securely held in place during the testing process.

To measure the electrical resistance of the MXene coating during tensile testing, copper wires were soldered onto the coating, and silver paste was applied to reduce the contact resistance. The change in electrical resistance during tensile testing was measured by using the two-probe method shown in Fig. 2.6a by *Fluke® 287 RMSTTM* multimeter with a *Bluetooth* data logging system. The contact resistance of 0.8 Ω was measured by taking the difference between the two-probe and four-probe methods of the multimeter contacts. This ensured that the measurements were accurate and reliable. To establish a relationship between the applied force and resistance, the statistical correlation coefficient was calculated. The statistical correlation coefficient is a measure of the strength of the relationship between two variables, in this case, the applied force and the resistance of the MXene network.

2.2.4. Fatigue testing of T-profile composite

Another objective of this study was to investigate the fatigue behaviour of the composite material under cyclic loading. To accomplish this, five composite specimens of the dimensions as shown in Fig. 2.6 were tested for tensile-tensile

fatigue on a 10 kN load cell capacity *Instron ElectroPuls E10000T*TM machine, manufactured by *Instron*®, Norwood, MA, USA.

The specimens were tested for 6000 cycles, after being split into two sets of 2000 and 4000 cycles, consecutively. The parameters used in the testing process are listed in Table 2.3. To ensure accurate measurements, the mounting of specimens on the machine and the measurement of change in electrical resistance were done in the same manner as described in Section 2.2.3 *Tensile Testing*.

The loading amplitude of the *Instron* machine was set in the elastic region of the sample to avoid any plastic deformation. The measurement of cyclic displacement was functional only by the internal load cell of the *Instron* machine. However, the error probability in measuring the displacement increases due to the slippage of the samples at grip. To ensure the accuracy of the displacement measurement, the load cell was calibrated against an external optical strain sensor by tensile testing pristine bisphenol F epoxy dog-bone specimens according to ISO 527-2-5A. The difference in displacement measurement was found to be 0.28%.

Table 2.3. Fatigue testing parameters

Parameter	Values	
No. of cycles	2000	4000
Frequency (Hz)	0.5	1
Load (N)	50	100

2.3. Multiaxial Woven Composite Manufacturing and Characterization

2.3.1. Design of a multiaxial pattern

Multiaxial ORW fabrics can be distinguished between the base fabric, consisting of warp and weft threads, and the multiaxial portion. The base fabric is oriented in the 0° direction (the warp threads) or 90° direction (the weft threads). The multiaxial threads can be introduced into the fabric at discrete angles with two partially independent thread systems. Details on the possible fibre orientations of the multiaxial threads (the weave angle) are described in Table 2.4. These values are calculated by taking in account the lateral and vertical shift of MAF. The lateral shift of MAF can be attributed to the lateral movement of multiaxial warp insertion needles. These needles are capable of shifting laterally in a discrete distance of the reed count. In the present study, the reed count is 2.5 needles/cm, which makes the lateral movement of the needle in discrete amounts of 8 mm, 16 mm, 24 mm, and so on. This number can be denoted as a sequence n , $2n$, $3n$ and so on. The vertical shift of MAF can be attributed to the number of weft insertions including the one binding MAF. This number can be denoted by m . In this study, the number of weft per cm was 2.5. The angle can be calculated with the following equation:

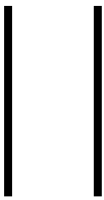


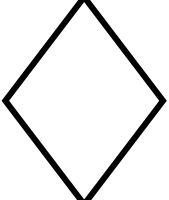
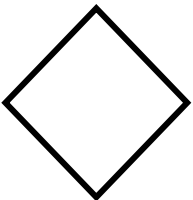
$$\theta = \tan^{-1} \left[\frac{n}{m} \right]. \quad (2.4)$$

Table 2.4. Possible angles for MAF

Weft threads m	Lateral shift n		
	$n = 1$	$n = 2$	$n = 3$
1	63.4	76.0	80.5
2	45.0	63.4	71.6
3	33.7	53.1	63.4
4	26.6	45.0	56.3
5	21.8	38.7	50.2
6	18.4	33.7	45.0
7	15.9	29.7	40.6
8	14.0	26.6	36.9
9	12.5	24.0	33.7
10	11.3	21.8	31.0
11	10.3	20.0	28.6
12	9.5	18.4	26.6
13	8.7	17.1	24.8
14	8.1	15.9	23.2
15	7.6	14.9	21.8
16	7.1	14.0	20.6
17	6.7	13.2	19.4
18	6.3	12.5	18.4
19	6.0	11.9	17.5
20	5.7	11.3	16.7

With the data values from Table 2.4, 5 patterns were designed, whose schematics are as shown in Table 2.5 and woven on the ORW machine with the plain weave as base. MAF gradually increased the angle from 0, 14, 27, 34 and 45. Glass fibre *Hybon2002*TM of 1200 tex from *NEG*® Japan was used as the warp, the weft, and MAF. The resultant fabric ply had 600 GSM with 2.5 threads/cm warp and weft density. The measured distance between two adjacent MAFs was 2.5 cm.

Table 2.5. Multiaxial weaving patterns

MAF angle 0°	MAF angle 14°	MAF angle 27°	MAF angle 34°	MAF angle 45°
				

2.3.2. Manufacturing of multiaxial composite and tensile testing

The multiaxial composites were manufactured by the vacuum assisted resin infusion process, as shown in Fig. 2.7b. When applying this method, a polished glass plate is taken as the base. A wax based release agent is applied in the area where the fabric preforms are to be placed. Four layers of glass fabric plies were placed on the plate, wherein the multiaxial plies were sandwiched between two plain woven plies of 600 GSM, as shown in Fig. 2.7a. Finally, a peel ply, a flow enhancer, and vacuum foil were placed on top of each other. The whole setup was vacuum sealed with a sealant tape, and negative pressure was applied. After ensuring that there was no leakage, epoxy resin was allowed to wet the setup, which was closely monitored till the whole preform was wetted out. The epoxy resin system in use was *RIMR426*TM, whereas the hardener was *RIMR435*TM manufactured by *Hexion*®, USA. After the preforms had been consolidated, the laminates were cured in an oven for 8h at 80° C.

The laminated composites were tensile tested according to ISO 527-4 test standard on a *Zwick Roell*® testing machine. First, they were polished, glued with tabs, and later cut into dimensions of 250 mm x 25 mm. A hole of 5 mm was drilled in the centre of the pattern to study the reinforcement effect of the fibres. The hole size resembled the standard bolts used for fitting composite panels. To study the effect of reinforcement on the hole diameter, 0° MAF samples were drilled with 7, 8, and 9 mm holes, respectively. The damage in the tested samples was visually analyzed.

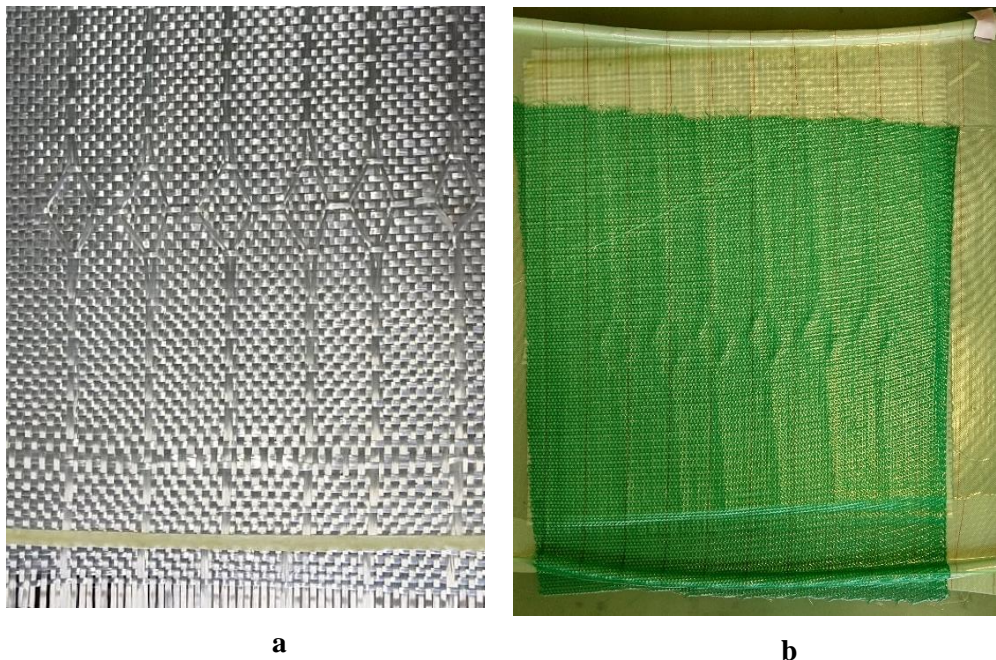


Fig. 2.7 Manufacture of composite: a) sandwich plies of MAF 34°, b) resin infusion of plies

2.3.3. Development of multiaxial fabrics on a closed reed mechanism

As described in the literature review, there are several methods for weaving multiaxial fabrics. However, a major drawback of these processes is the complex modification in the weaving loom, either in the reed, or in the shedding area, as described in ORW. The closed reed and heald wires pose an obstacle to the lateral movement of MAF. Hence, an innovative method was developed to manufacture multiaxial fabrics on a closed reed weaving mechanism [167].

2.4. Simulation of Multiaxial Composite Mechanical Properties

A numerical simulation model of multiaxial composites manufactured as described in Section 2.3 was carried out in *Ansys*. As discussed in the literature review, *Ansys* is powerful software for the simulation of a variety of load conditions and materials. It also offers in-built material properties and ACP (*Ansys* composite pre-processor) module for simulation of composite materials.

2.4.1. Material properties and meshing of glass fibre composites

Material properties, as shown in Table 2.6, were derived from the mechanical characterization of the composites [168]. They were defined in the engineering data section. As shown in Fig. 2.8, a rectangular part of 250 mm x 25 mm was designed in the design modeller. It was assigned the shell type of a mesh as the ACP module input was only of the shell type.

Table 2.6. Material properties of glass fibre composites

Property	Value
Density	1.85 g/cm ³
Young's Modulus in X direction E_1	28085 MPa
Young's Modulus in Y direction E_2	28085 MPa
Poisson's ratio in XY ν_{12}	0.159
Shear modulus in XY G_{12}	3610 MPa
Thickness of the composite	2 mm

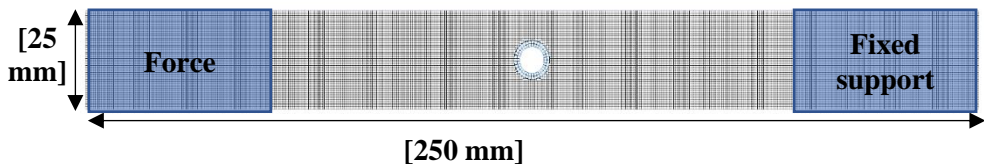


Fig. 2.8 Meshing and boundary conditions of glass fibre composite sample for tensile loading

During the meshing of the geometry, quadrilateral elements were defined with a size of 1.2 mm. Face meshing was applied to a circular hole to uniformly distribute the elements and reduce the distortion. A 50 x 25 mm area at each end of the geometry was defined in the named selection to apply the boundary conditions which would be

similar to the tabs mounted on the actual sample. The mesh consisted of 12800 nodes and 12849 elements.

2.4.2. Ply layup in ACP pre-module

The schematic workflow of static structural analysis is shown in Fig. 2.9. The geometry mesh and the engineering data setup were given as input to the ACP pre-module. The workflow in the module was as follows:

- a) Material data. The material properties defined in Table 2.6 were exported in this section. The thickness of a single fabric ply was set at 0.46, and 4 such plies were defined in a stack with $[0]_4$ configuration. For the sake of the accuracy of the simulation, the laminate and stiffness compliance matrices were calculated.
- b) Rosette and Edge sets. To define MAF in the reinforcements, an edge set was defined with the fibre path taken by MAF. The edge set is a feature of ACP module to define custom fibre paths in a composite. For an unreinforced hole, no edge sets were defined. In the next step, parallel rosettes were added to the geometry to define the directions X, Y and Z of the fibres relative to the global axis.
- c) Oriented selection sets and Modelling ply. The oriented selection sets is a feature where the fibre plies together with the rosettes are applied to the various sections of the geometry. In the case of MAF composite samples, 2 types of oriented selection sets were used, the X-Y direction for plain woven glass fibre plies, and edge sets for MAF. For unreinforced hole samples, only X-Y direction sets were applied to the whole geometry. The modelling ply is the final step where plies are defined according to the actual production stacking of the composites. For the MAF geometry, the edge set plies were placed in the middle section of the stack, with the top and bottom plies of plain glass fibre.

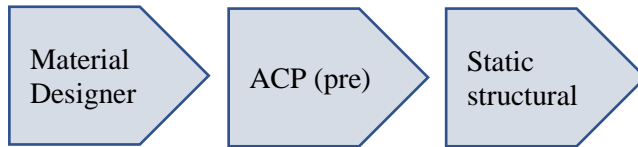


Fig. 2.9 Schematic of workflow in *Ansys*

2.4.3. Boundary conditions for tensile testing

To simulate the tensile testing of the composite, boundary conditions mimicking the tensile loading conditions were set, as shown in Fig. 2.8. The input from the ACP is fed to the static structural module, as shown in Fig. 2.9. The results of the experimental tests showed that the average extension at breaking for samples of unreinforced composites was 1.5 mm, while it was 1 mm for ORW reinforced composites. One end of the grip is stationary, while force was applied to the other end to ensure constant deflection of 2 mm/min. Thus, to set up the boundary conditions,

one named selection was applied a constant deflection of 1 mm, whereas the other was applied fixed support. The principal axis of the geometry was aligned to the X axis to ensure coordination between the rosette and the global axis. Force was applied in X direction, whereas fixed support was applied in the -X direction.

2.4.4. Material properties and meshing of carbon fibre composites

To simulate the impact properties of carbon composite, the material properties of bisphenol epoxy F were inputted from the manufacturer’s datasheet, as shown in Table 2.7. Carbon fibre 230 GPa available in the engineering materials library of *Ansys* was used as the reinforcement. The composite properties as shown in Table 2.8, were generated in the *Material Designer* module by selecting the representative volume element (RVE) of a plain-woven fibre mesh.

Table 2.7. Material properties of bisphenol epoxy F

Parameters	Values
Density	1.16 g/cm ³
Young’s Modulus	2700 MPa
Poisson’s ratio	0.35
Bulk modulus	3110 MPa
Shear modulus	1100 MPa
Tensile yield strength	83 MPa

Table 2.8. Material properties generated for carbon composite

Parameters	Values	Stress limit Parameters	Values	Strain limit Parameters	Values
Density	1420 kg/m ³	Tensile X	805 MPa	Tensile X	0.0126
Young’s modulus E ₁	61.34 GPa	Tensile Y	805 MPa	Tensile Y	0.0126
Young’s modulus E ₂	61.34 GPa	Tensile Z	50 MPa	Tensile Z	0.08
Young’s modulus E ₃	6.9 GPa	Compression X	509 MPa	Compression X	0.0102
Poisson’s ratio V ₂₃	0.3	Compression Y	509 MPa	Compression Y	0.0102
Poisson’s ration V ₁₃	0.3	Compression Z	170 MPa	Compression Z	0.012
Shear modulus G ₁₂	3.3 GPa	Shear XY	125 MPa	Shear XY	0.022
Shear modulus G ₂₃	2.7 GPa	Shear YZ	65 MPa	Shear YZ	0.019
Shear modulus G ₁₃	2.7 GPa	Shear XZ	65 MPa	Shear XZ	0.019

A 60 mm x 60 mm square plate and a hemisphere of 20 mm diameter was designed in the *Design Modeller* module. The hemisphere was meshed as with tetrahedral elements, whereas the plate as shown in Fig. 2.10 was meshed with quadrilateral elements. The overall schematic of the workflow is shown in Fig. 2.11, and the mesh of the composite plate contained 4770 nodes and 10325 elements. This data was inputted to the ACP pre module, and the procedure described in Section 2.4.3 was repeated.

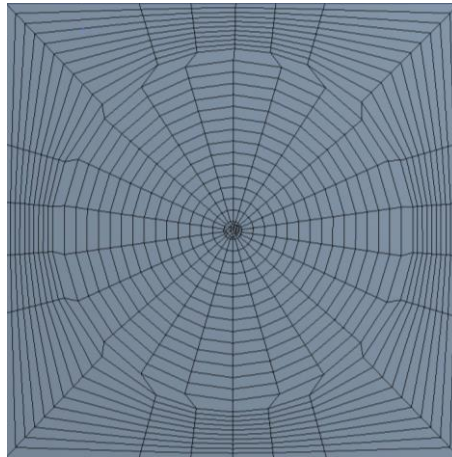


Fig. 2.10 Meshing of carbon fibre composite plate

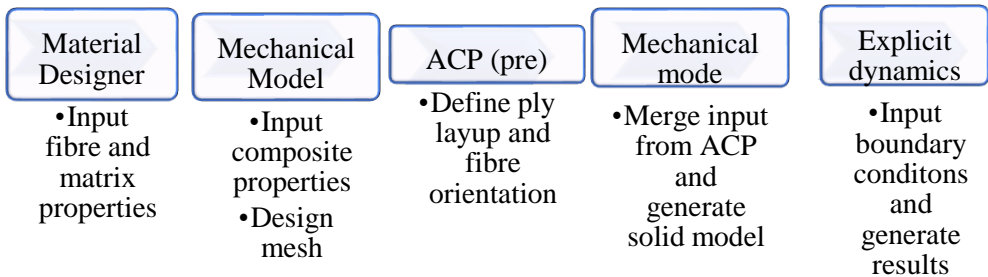


Fig. 2.11 Schematic of the workflow for simulation of impact loading[167]

2.4.5. Boundary conditions for impact loading

The output from the ACP pre-module was inputted to the *Explicit Dynamics* module of *Ansys*. *Explicit Dynamics* is useful for the conditions where the force varies dynamically with respect to time. The hemispherical impactor was assigned 2.1 m/s of velocity in the -Z direction to simulate the fall of the drop weight. A point mass at the centre of the impactor mesh was assigned with 5.186 kg (colored in red). The middle circular section of 40 mm diameter, visible in Fig. 2.12, was left unconstrained, while the rest of the mesh was constrained as a fixed support (colored in blue). The

plate and the impactor mesh were set to the frictional contact, and the coefficient of friction was set to 0.33.

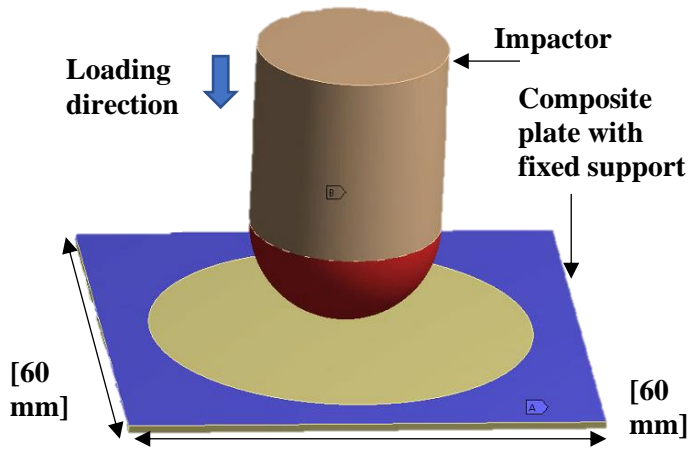


Fig. 2.12 Boundary conditions for impact loading of carbon composites [167]

3. RESULTS AND DISCUSSION

3.1. SHM of Orthogonal 3D Woven Planar Composites Infused with CNT

3.1.1. Microscopic characterization of CNT dispersed in 3D woven composite

The CNT particles permeate through the thickness of the 3D woven glass fabric and stick to the glass filaments, thus showing strong interfacial bonding between the CNT and the matrix, according to the SEM characterization of $S_3.G_1$ samples.

As illustrated in Fig. 3.1, at 80× and 800× times magnification, the CNT dispersion could be seen as dark patches against the translucent composite. The ‘macroscopic cake filtration’ phenomenon, which is brought on by the filtering of large CNT agglomerates by glass fibres, can be seen in Fig. 3.1b of S_2 sample at 80× magnification. Agglomerations of CNT particles are created as a result of this filtering mechanism, and they can be seen in Fig. 3.1c at 800× magnification. The fact that these agglomerations are primarily found in the space between weft yarns suggests that these areas are denoted by a larger concentration of CNT.

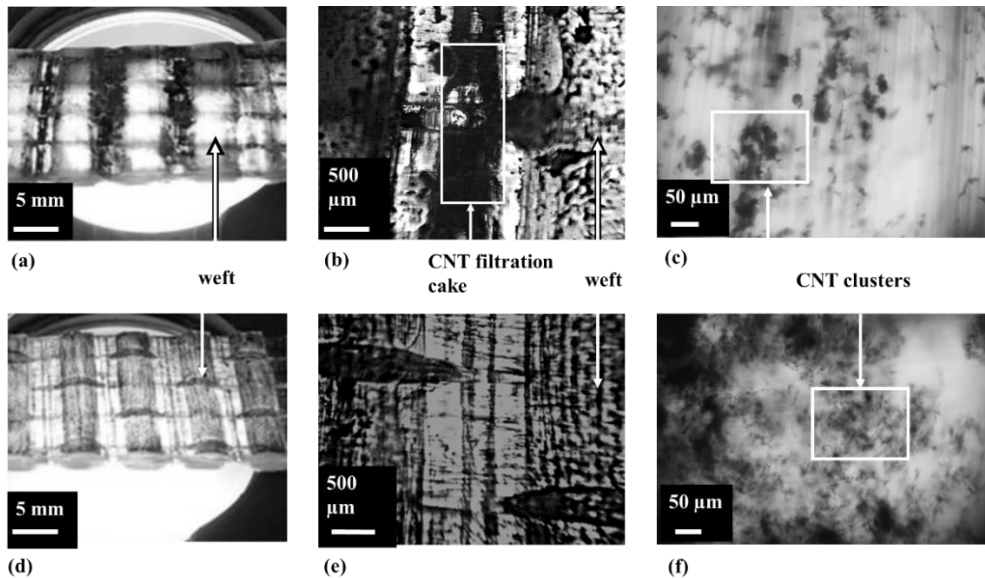


Fig. 3.1 CNT infusion by conventional VARTM process: (a–c), CNT infusion by vacuum transfer process (d–f) [78]

In contrast, because the CNT particles were directly deposited on the fibres rather than passed through them, it was evident from the 80× magnification of the $S_3.G_2$ sample in Fig. 3.1e that no filter cake had formed. The $S_3.G_2$ sample in Fig. 3.1f was magnified 800× times, and the picture revealed that CNT particles were equally distributed, and they formed a broader network than S_2 . When compared to the

traditional vacuum infusion, optical micrographs showed that CNT particles were equally spread with minimal filtering by the fibres.

As shown in Fig. 3.2a, CNT particles at 100000 \times are distributed throughout the composite in the form of tiny micro clusters. Three main categories can be used to group the presence of CNTs in the composite. First, Fig. 3.2b depicts a resin-rich region devoid of fibres at 10000 \times . This shows that the CNTs are evenly distributed throughout the resin, which can provide the composite material with improved mechanical and electrical properties. Second, in Fig. 3.2c, the matrix containing warp fibres is displayed at 500 \times . It is visible that the CNT is sticking to the glass filaments and creating a network of tiny clusters all throughout the matrix. Thirdly, Fig. 3.2d at 100 \times displays the matrix with weft fibres. The CNT can be observed here adhering to the weft and forming micro clusters between the fibres.

Furthermore, Fig. 3.2d shows that the cross-section of the warp and weft fibrils did not form macro clusters or filter cakes. This is a crucial finding since the development of a filter cake may result in weak mechanical qualities and a reduced structural integrity. The SEM analysis shows that CNT had permeated and attached to the matrix and the core fibre, with some micron-scale filtering by the fibres. This homogeneous dispersion behaviour makes it a desirable material for structural health monitoring because it can make strain and damage measurements easier.

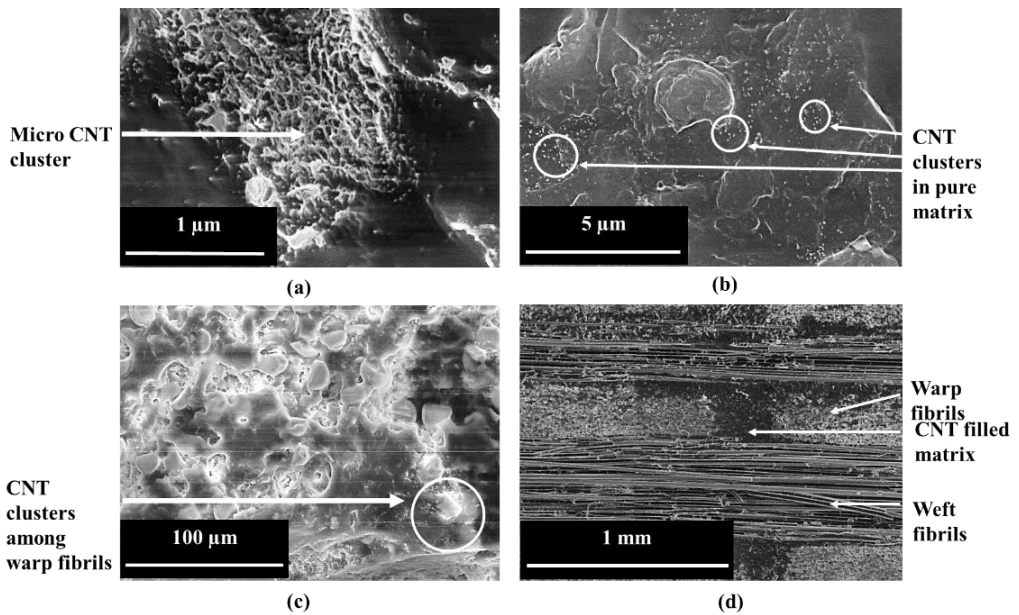


Fig. 3.2 SEM characterization of S₃.G₁ sample: (a) micro cluster of CNT, (b) CNT in resin-rich area as micro clusters (the white marking), (c) cross-section of warp fibrils in the matrix, (d) cross section of weft and warp fibrils [126]

3.1.2. Tensile test and electromechanical response of CNT

Fig. 3.3 shows the graphs of $\Delta R/R_0$ (change in resistance normalized to the initial resistance) plotted against the tensile strain for three composite samples $S_1.G_1$, $S_1.G_2$, and $S_3.G_1$, respectively. The resistance values were filtered by using the moving average method over 25 datapoints. These graphs demonstrate a statistically monotonic relationship between the stress and the resistance. To measure the efficiency of the CNT piezoresistivity, the Spearman's correlation coefficient between the resistance and the stress data was calculated for each of the five samples. The correlation coefficient ranges from -1 to 1, and it is calculated by taking the difference of the weighted average of all the datapoints of stress and the absolute resistance values. Table 3.1 presents the correlation coefficients with their respective GF values. Table 3.2 shows the statistical analysis of all the samples tested for tensile loading.

Table 3.1. Gauge factor and correlation coefficient for tensile test

Sample code	Gauge Factor (GF) at 1% strain	Correlation coefficient
$S_1.G_1$	0.91	0.81
$S_1.G_2$	1.38	0.96
$S_3.G_1$	1.79	0.94

Table 3.2. Statistical analysis of tensile testing samples

Sample	Ultimate tensile force (kN)		
	$S_1.G_1$	$S_1.G_2$	$S_3.G_1$
1	26.57	27.89	26.33
2	28.87	24.25	24.35
3	24.69	23.48	27.43
4	27.66	27.65	25.63
5	25.32	26.12	26.34
Average	26.622	25.878	26.016
Coefficient of variance	0.06	0.07	0.04

Specimen $S_1.G_1$ underwent tensile stress, and a crack developed in the CNT film area which spread through the sample's breadth and began in the notch. The CNT film, which had already begun to lengthen in response to the deformation of the composite specimen, began to deteriorate due to the absorption of the fracture energy, which caused a brief spike in the network's total resistance. This can be seen in overall strain, as shown in the sample given in Fig. 3.3a. The strain cannot be efficiently mapped due to the CNT network's ongoing degradation, which is supported by a reduced correlation coefficient. The sensor and composite specimen were severely damaged when the sample finally fractured inside the CNT film area.

The resistance of the CNT network of $S_1.G_2$ altered in accordance with the strain of the composite substrate without absorbing the fracture energy of the composite substrate when the matrix crack at the notch began to occur outside the CNT film.

Therefore, the following mechanisms can be used to explain the change in resistance of the CNT network, as illustrated in Fig. 3.3b.

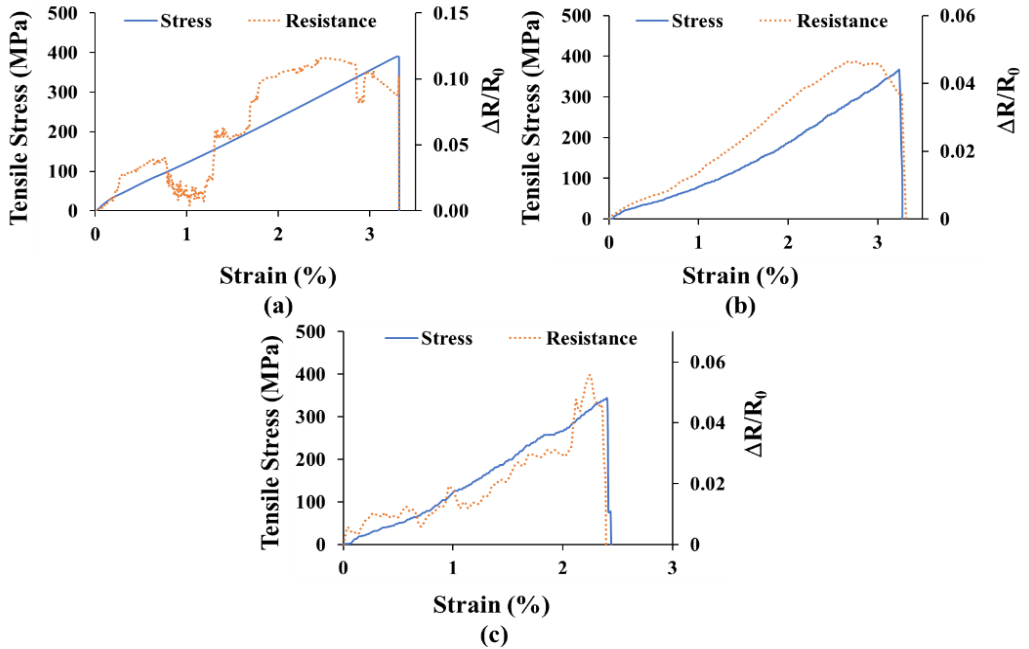


Fig. 3.3 Real time damage sensing during tensile loading: a) $S_1.G_1$, b) $S_1.G_2$, c) $S_3.G_1$ [126]

Similar to a conventional strain gauge, the macro level variation in the composite substrate's dimensions affects the CNT sensor's geometry, which, in turn, affects the resistance. A network of individual CNTs which stretch in response to the substrate's strain make up the CNT sensor, which results in an increase in resistance. However, due to a significant Poisson's value contraction, a decrease in the electrical resistance value of the CNT sensor is seen at the maximum stress, which may be determined to be between 2–3% strain.

The nanotubes drift away as a result of the applied strain at the micro scale, which raises the tunnelling and contact resistance. Additionally, it activates the innate piezoresistivity of CNT, which aids in the overall resistance change of the sensor.

According to Fig. 3.3c, the electromechanical response of the CNT network in $S_3.G_1$ under tensile loading reveals that the piezoresistive signal produced by the CNT network is a mixture of some CNT absorbing the fracture energy of the fibres and the matrix, similar to sample $S_1.G_1$, and the remaining CNT elongates with the strain without absorbing the fracture energy, similar to sample $S_1.G_2$.

While the overall signal closely correlates with the strain, the microfractures of the fibre and the matrix are identified as brief spikes in the signal. The correlation coefficient suggests this. The CNT impregnated in sample $S_3.G_1$ exhibits a drop in

resistance between 2–3% strain, i.e., close to the sample's breaking point, as a result of the width contraction.

For samples $S_1.G_1$ and $S_3.G_1$, a linear regression model was created to determine the GF , which is the slope of the line that fits the resistance change vs. the strain graph the best. For these samples, the graph is not linear, with the GF for CNT concentrations of 0.05–0.3% in the pure matrix with the fibre reinforcement ranging from 2.5 to 3.7 in the non-linear zone, and 2.2–2.4 in the linear region. This study and the GF of $S_1.G_2$ are in good agreement.

For $S_1.G_1$, however, the damage build-up and the fracture energy absorption resulted in sudden and significant increases in resistance over a modest strain, which points to a greater GF . The lower correlation coefficient suggests that this does not ensure the effectiveness of mapping the strain. If compared to the other samples, sample $S_3.G_2$ has the highest GF because the resistance change demonstrates a combination of linear and non-linear behaviour.

To measure changes in the mechanical strain, CNT sensors make use of their electrical characteristics. CNT sensors use the concept of tunnelling resistance, which happens when electrons pass through a potential barrier as the basis for their detecting process. The resistance of the CNT sensor changes with the amount of the mechanical strain being applied, as the strain affects the distance between the nanotubes, and thus the tunnelling resistance.

The distance between adjacent CNT particles can grow to infinity when subjected to tensile loading, thereby allowing for a wider variation in resistance and, consequently, a higher sensitivity to strain. However, under compressive stress, the tunnelling gap shortens, and CNT overlapping rises, which limits the ability of CNT to map the strain. This results in a reduction in resistance, which becomes saturated once a certain degree of strain has been reached. As a result, the sensitivity of CNT sensors to compressive strain is often lower than their sensitivity to tensile strain.

It has been discovered that the lowering of the filler weight percentage can boost the strain sensitivity of CNT sensors. This is because of the possibility that a larger filler weight percentage could lead to a denser packing of CNT, which might restrict their capacity to deform and lessen their sensitivity to strain. By lowering the weight proportion, the CNT particles are given more freedom to move, and, as a result, respond to the strain more strongly. It is crucial that CNT networks can detect both tensile and compressive loads separately in order to accurately map the total flexural loading.

3.1.3. Electromechanical response of CNT under flexural loading conditions

Five samples of $S_3.G_1$ and $S_3.G_2$ presented in Table 3.3 were each subjected to flexural loading in order to compare the effectiveness of completely infused CNT particles with partially infused ones for flexural load mapping. To quantify the changes in resistance with the applied strain, the piezoresistive response of the CNT network was displayed as $\Delta R/R_0$ against the strain values.

Table 3.3. Sample code and ultimate flexural force

Sample	Ultimate force (kN)	
	S ₃ G ₁	S ₃ G ₂
1	2.87	2.12
2	2.65	2.65
3	1.96	1.86
4	2.10	1.97
5	2.43	2.75
Average	2.4	2.27
Coefficient of variation	0.14	0.16

The experiment’s findings demonstrated that the partially infused CNT network had a higher flexural load mapping efficiency than the fully infused network. As it can be seen in the graph of one representative sample from each group in Fig. 3.4, this was demonstrated by a higher change in resistance for a given degree of strain.

The results of this work concur with earlier investigations on the electromechanical response of sensors under flexural loading in composite materials. For example, similar results have been observed in studies on CNT spray-coated on glass fibres [119], silver-coated sensors embedded in glass composites [114], and carbon black coated sensor wire embedded in a 3D woven angle interlock composite [34].

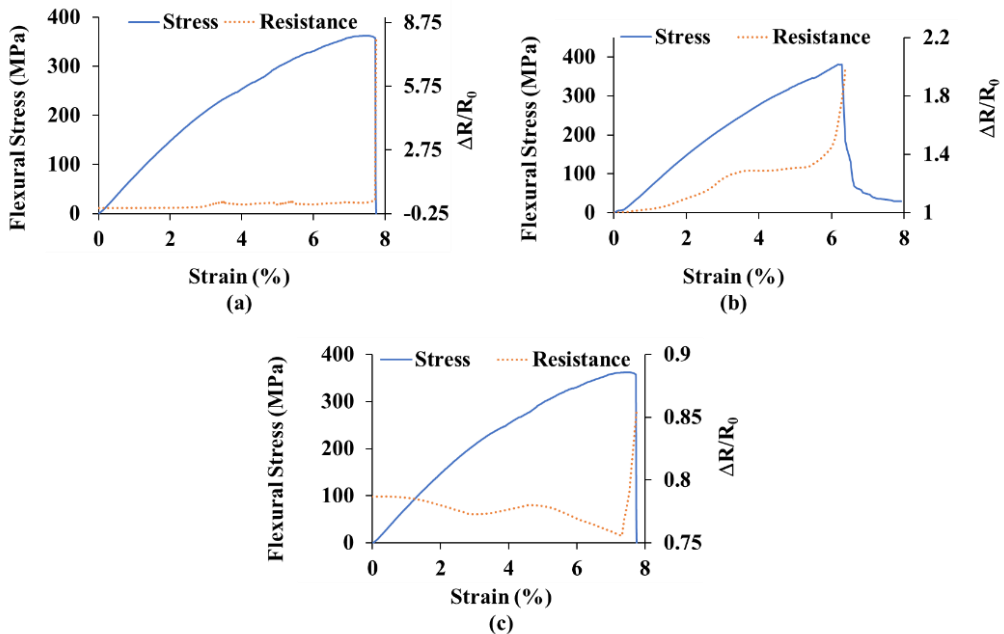


Fig. 3.4 Real time damage sensing during flexural testing: (a) S₃G₁, (b) S₃G₂ surface subjected to tensile stress, (c) S₃G₂ surface subjected to bending stress [126]

When the bending load was applied to S₃.G₁, a site of the absence of weft yarns was where the crack first appeared. Damage initiation in the composite started at the surface under tension and moved towards the compression side due to the brittle nature of the matrix material and its lower tensile strength relative to its compressive strength. While, in the compression section, the distance between the adjacent particles CNT dropped, the resistance increased on the bottom portion of the composite where the distance between adjacent CNT particles increased.

As seen in Fig. 3.4a, the sum of the increase and decrease in resistance tended to maintain the values constant up to 3% strain where the crack had not yet developed. Beyond 3% strain, however, the fracture spread and eventually destroyed the CNT network, thus causing a gradual increase followed by a sudden increase in the resistance value at the sample's ultimate failure.

This behaviour of the change in resistance values has been studied in previous research, and the findings are consistent with those of the present study [10]. The results suggest that CNT networks can effectively monitor crack formation and propagation in composite materials under bending stress, and that changes in resistance values can be used to track the progression of damage in the material.

The S₃.G₂ specimens only exhibited conductivity along a single surface, thereby indicating that the CNT network was contained inside the interface between the fibre and the matrix, and it did not permeate through the thickness of the specimens. According to Figures 3.4b and 3.4c, the electromechanical response of the CNT network was unique for both tensile and compressive stress during the bending test.

When the conductive bottom surface of S₃.G₂ was subjected to tension during the bending test, the increase in the distance between the overlapping CNT and tunnelling resistance increased the overall resistance in response to the applied strain. The formation of microcracks in the composite led to an increase in the resistance values due to the breaking of CNT networks, which can be observed to be between 2–6% strain. At the ultimate stress, the matrix and the fibres broke, thus leading to the CNT network's catastrophic failure, which can be identified as a steep increase in resistance at 6.2% strain.

When the conductive top surface of S₃.G₂ was subjected to compression stress during bending, as shown in Fig. 3.4c, the resistance started decreasing as the gaps between adjacent CNT particles decreased. The ultimate fracture of the composite led to permanent damage in the CNT network, which could be observed as a steep increase in resistance at 7.5% strain.

3.1.4. Summary of research findings for SHM of 3D woven composite by CNT

In this study, the research focused on the manufacturing of self-sensing composites by using a novel method of infusing CNT with porous media on a 3D woven fabric preform. The resulting composites were able to function as a real-time strain and damage sensor. This is an important development as it allows for continuous monitoring of structures such as aircraft, bridges, and wind turbines which are subject to mechanical stress and damage over time.

To test the performance of the self-sensing composites, the composites were subjected to tensile and flexural loading. The piezoresistive response of the CNT network was studied by measuring the change in the resistance values in response to the applied strain. To compare the functionality of the developed sensors with the conventional methods, CNT was cast on the surface of pure epoxy infused 3D woven composite substrates and subjected them to tensile loading.

The results of the study showed that the concept of localized infusion of CNT via porous media is feasible for real-time strain monitoring and damage sensing in orthogonal 3D woven composites. The CNT particles were uniformly dispersed in the composite with marginal microscopic filtration by porous material infusion, which was found to be superior to the conventional vacuum-infused composites where macroscopic cake filtration and agglomeration of CNT were observed.

The study also found that the level of vacuum pressure used during the infusion process had a significant impact on the distribution of CNT within the composite. At a pressure of 101.3 kPa, the CNTs were infused through the thickness of the fabric, whereas, at a pressure of 30.4 kPa, the CNT particles were only infused in the outer layer fibres. This was confirmed by measuring the resistance of the composite across the thickness, scanning electron microscopy (SEM) and optical imaging.

It was found that through-thickness infused CNTs were efficient in measuring the tensile strain and the damage of the fibre as well as the matrix. The partially infused CNTs were efficient in monitoring the flexural load under tensile and bending stress, similar to other strain sensing techniques. Therefore, depending on the requirement and the area of sensing, CNT can be infused through the thickness or deposited only on the fibre surface.

Another notable finding of the study was that the self-sensing composites were manufactured by using only a minimum amount of CNT, without any sophisticated tools for dispersion, and it was the only additional component in the manufacturing process. This makes the self-sensing composites manufacturing method a cost-efficient and simple option.

3.2. SHM of 3D Woven T-profile Composite Doped with MXene Nanoparticles

3.2.1. Electromechanical response of MXene flakes under tensile loading

Statistical analysis of all the samples is shown in Graph 3.5. The average value of the ultimate tensile force of 4 samples is plotted, which comes to 1844 N. In Fig. 3.6a, the force-displacement graphs for four composite T-profile samples are shown. However, it is important to note that one of the five samples was rejected due to a premature failure at the clip restrains. It is also worth noting that the graphs indicate two distinct zones – the initial failure and the final failure. We can identify the initial failure as a drop in the tensile load values for the first time. Additionally, it can also be observed that the force and resistance curves exhibit a statistically monotonic relationship.

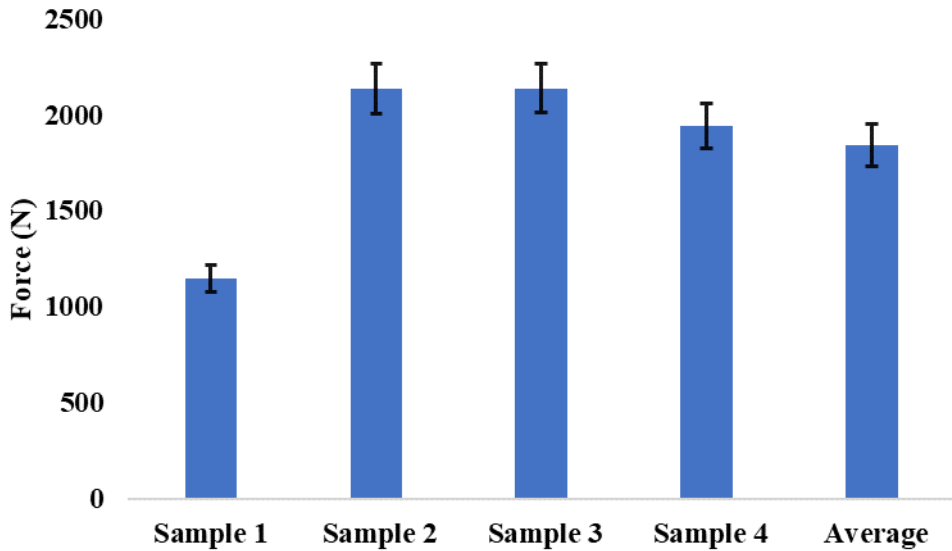


Fig 3.5 Statistical analysis of T profile composite samples

To further analyse this relationship, the product moment correlation coefficient for each of the four samples was calculated. It was done by dividing the covariance by the standard deviation of the force and the absolute resistance datapoint values. The results are presented in Table 3.4, which includes the correlation coefficient and the ultimate force of each sample. It is important to note that the correlation coefficient ranges from -1 to 1, where ‘-1’ denotes an entirely inverse relationship, whereas ‘1’ indicates a purely direct relationship between the datasets.

Since the behaviour of all the graphs is similar, the piezoresistive response of the MXene coating of one sample was plotted as shown in Fig. 3.6b. It was obtained by plotting $\Delta R/R_0$ against force-displacement. It is worth noting that the piezoresistive response of the MXene coating corresponds well with the previous studies on MXene-based SHM of composites.

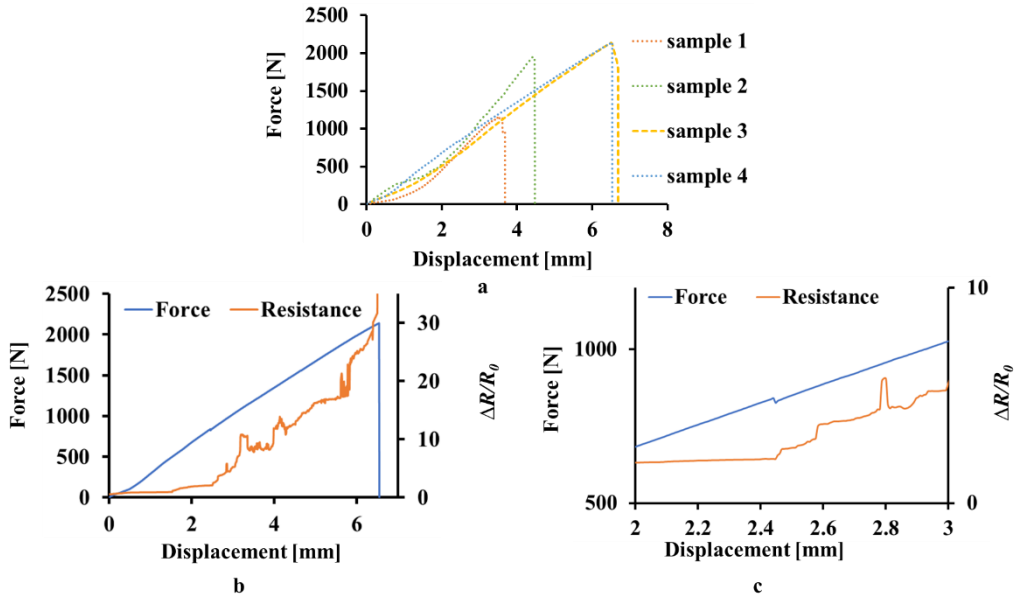


Fig. 3.6 Real time deformation monitoring of composite T-profile: (a) tensile testing of composite T-profile, (b) piezoresistive response of MXene coating, (c) enlarged section of the initial failure [139]

During the experiment, the sample was subjected to an increasing tensile load, which caused it to elongate. As the sample elongated, the stress began to accumulate at the junction region of the T-profile. This region was where the composite's flange and the base components were joined together. As a result of this stress accumulation, the resistance of the MXene coating began to increase, which was measured and recorded in Fig. 3.6b.

At a displacement of 2.44 mm, the initial failure of the composite occurred. This failure was detected by observing a disturbance in the resistance value of the MXene coating, as shown in Fig. 3.6c. Between 2.44 mm and 6.54 mm displacement, the crack propagation started at the resin-rich area of the junction and continued to propagate into the base section. The progression of the crack ultimately led to a catastrophic failure of the composite causing the flange and the base parts to separate from each other.

Interestingly, the crack did not propagate near the restraints, which were the clips at the base and the clamp at the flange. Instead, the crack was restricted to the base section of the composite. Throughout the stress accumulation until the failure, the deformation of the composite was detected by a steady increase in the resistance of the MXene coating, which was monitored and recorded in Fig. 3.6b.

Table 3.4. Correlation coefficient and ultimate tensile force

Parameter	Sample 1	Sample 2	Sample 3	Sample 4
Correlation coefficient	0.70	0.68	0.71	0.68
Ultimate tensile force (N)	1150	2138.5	2140.2	1948

When a tensile load is applied to the T-profile, the junction region where the direction of the load changes from the top clamp to the clip restraints experiences a build-up of stress. This is the region where the composite initially fails as the external force exceeds the tensile strength of the matrix. Subsequently, the yarn/matrix interface and the composite itself fail as the force increases further. Although delamination is typically the main failure mode for laminated composites, the 3D woven T-profile composite experiences yarn/matrix damage at the junction as its primary failure mode.

On planar surfaces, the MXene coating demonstrates a piezoresistive response which corresponds linearly to the applied strain. As shown in Fig. 3.6b, the steady increase in the resistance of the MXene coating is due to the combined elongation of the base and the flange sections. The junction of the T-joint composite has been identified as the location where crack formation begins based on the theoretical and experimental reports. As the MXene coating is adhered to the composite, it absorbs the fracture energy and cracks in a similar manner, which results in spikes in the resistance values.

At a macro level, the MXene coating's resistance changes in response to the composite substrate's dimensional changes, similar to the traditional strain gauges. At a micro level, the MXene coating consists of a network of individual MXene flakes that absorb the fracture energy of the substrate and break.

3.2.2. Electromechanical response of MXene nanoparticles under fatigue loading

The results were generated by plotting the $\Delta R/R_0$ graphs of a single sample in Fig. 3.7, which provided insights into the electromechanical response of the MXene to fatigue loading within the elastic limit. The cyclic stress applied at a frequency of 0.5 Hz resulted in a change in resistance, as shown in Fig. 3.7a. The change in the resistance of the MXene coating corresponded to the cumulative effect of the cyclic stress imparted by the machine. As the number of cycles increased, so did the load, displacement, and the subsequent deformation, which were sensed by the MXene coating as a gradual rise in the resistance values. The resistance data points were averaged to produce the results shown in Fig. 3.7b.

The MXene coating was also capable of sensing any cracks or damage that occurred during the loading, as indicated by a sudden change in the resistance values at the same load. This was captured at the 1000th cycle in Fig. 3.7a, thus indicating that the MXene coating could detect damage early on in the loading process.

The composite T-profile sample was subjected to a 50 N load within its elastic limit, which resulted in minimal damage to the MXene coating. This was confirmed by the constant resistance readings before and after the 0.5 Hz frequency loading.

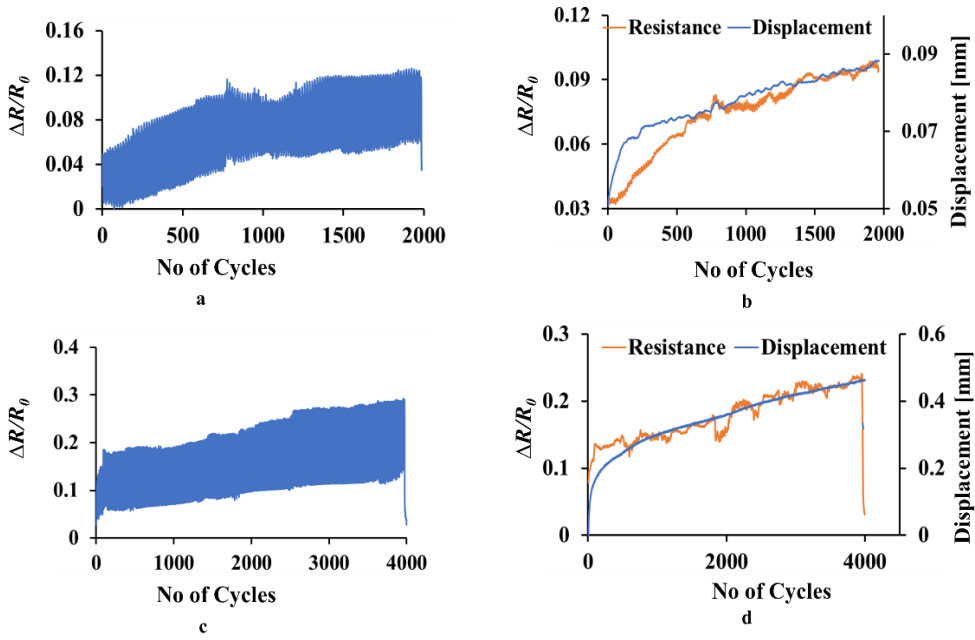


Fig. 3.7 Real-time fatigue sensing of composite T-profile by MXene coating: (a) resistance measurement at 50 N–0.5 Hz, (b) sensing of displacement component during fatigue loading of 2000 cycles, (c) resistance measurement at 100 N–1 Hz, (d) sensing of displacement component during fatigue loading of 4000 cycles [139]

When the loading force was increased to 100 N and the frequency was raised to 1 Hz, stress accumulation and damage progression occurred rapidly. Although the composite sample was stressed near the border of its elastic limit and thus accumulated some damage, the overall structural integrity of the MXene coating remained stable. This was demonstrated by a 3.2% increase in the resistance values of the MXene coating before and after the test, which indicates that the coating was still able to sense the cyclic stress and the cumulative increase in deformation corresponding to the external displacement. These results are presented in Fig. 3.7c and Fig. 3.7d, respectively.

It is worth noting that the electromechanical response of the MXene coating during cyclic loading at 0.5 Hz and 1 Hz in this study is consistent with the previous studies. These findings suggest that the MXene coating is a reliable material for sensing cyclic loading and deformation under the given loading conditions. However, further studies are still necessary to determine the long-term durability of the coating and its performance under varying loading conditions.

During the fatigue loading process of the composite sample, MXene flakes experience cyclic stress and relaxation, which leads to periodic changes in the resistance values. This phenomenon can be attributed to the tunnelling and contact resistance. However, with each cycle, the strain and load on the sample increase, causing the stress to accumulate at the junction of the composite. As a result, the MXene coating experiences a permanent increase in the resistance values since the individual flakes drift apart and cannot return to their initial position. This mechanism leads to a direct correlation between the resistance of the MXene coating and the cyclic stress and deformation of the composite T-profile.

To elaborate further, the cyclic loading of the composite sample leads to a repetitive application of stress, followed by a relaxation phase, on the MXene flakes. During the stress phase, the flakes are brought closer together, thereby resulting in a decrease in the resistance values due to the increased tunnelling and contact between them. Conversely, during the relaxation phase, the flakes move apart, which leads to an increase in the resistance values.

However, with each cycle, the stress at the junction of the composite increases, leading to a permanent deformation of the MXene flakes. This deformation makes it impossible for the flakes to return to their original position, thus leading to a permanent increase in the resistance values. The accumulation of this deformation leads to a direct correlation between the resistance of the MXene coating and the cyclic stress and deformation of the composite T-profile.

Therefore, the resistance of the MXene coating can serve as a reliable indicator of the mechanical performance of the composite T-profile. By monitoring the changes in the resistance values, one can determine the level of the cyclic stress and deformation that the composite is experiencing. This information can be crucial in assessing the durability and reliability of the composite in various applications.

3.2.3. Summary of research findings from SHM of T-profile composite using MXene nanoparticles

In this research study, a self-sensing composite was developed by using MXene particles sprayed onto a 3D woven composite T-profile. The MXene coating demonstrated the ability to sense damage and deformation in real-time under tensile and fatigue loading conditions. To better understand the electromechanical response of the MXene coating, the resistance values were plotted against the force-displacement.

The results of the study demonstrated that the application of MXene particles to the junction of the composite T-profile is an efficient method for detecting damage and deformation in complex-shaped composites. The partially delaminated MXene flakes at a concentration of 3.3 mg/mL were successful in sensing the deformation of the T-profile composite. The MXene coating was able to sense the initial failure and the total deformation until failure through a spike and a steady increase in the resistance values, respectively.

During tensile testing, the junction region was identified as the primary failure zone, thereby emphasizing the critical nature of this area and the need for health

monitoring. The MXene coating sprayed at the junction was capable of sensing the initial failure and the total deformation until failure through a spike and a steady increase in the resistance values, respectively.

During fatigue loading, damage was detected through an abrupt change in the resistance values under the same loading conditions. At a load frequency of 0.5 Hz and 1 Hz for 50 N and 100 N, respectively, the MXene coating was stable and captured the cyclic stress. However, at a load-frequency combination of 100 N-1 Hz, a permanent increase of 3.2% in the resistance of the MXene coating was observed, which indicates a threshold level of the damage initiation.

The self-sensing composites developed in this study were found to be easy to manufacture and cost-effective. However, the sensing function was limited to deformation monitoring. In the future, the piezoresistive response of the MXene nanoparticles could be calibrated against the conventional strain gauges mounted on the base and the flange sections of the T-profile. This data could be used to determine the stress levels at various zones in complex-shaped composites.

3.3. Multiaxial Composite Mechanical Test and Results

3.3.1. Tensile testing of ORW pattern composite with a 5 mm hole

The statistical data of all the tested samples is shown in Table 3.5. As shown in Fig. 3.8, a comparison of the ultimate tensile force averaged over 6 samples for each pattern shows a clearly downward trend with an increase in the fibre angle. This suggests that, with an increase in the MAF angle, the reinforcing effect for a hole decreases.

Table 3.5. Tensile testing data of ORW composites

Sample	Ultimate tensile force (N)				
	0°	14°	27°	34°	45°
1	21815	21605	21156	17122	18353
2	19348	20423	20043	18467	18138
3	23091	21745	17318	17983	16849
4	22382	19064	18639	20308	17840
5	19658	17184	21088	18657	21497
6	20679	20017	19378	19356	15126
Average	21162	20006	19604	18470	17967
Coefficient of variation	0.07	0.08	0.07	0.05	0.11

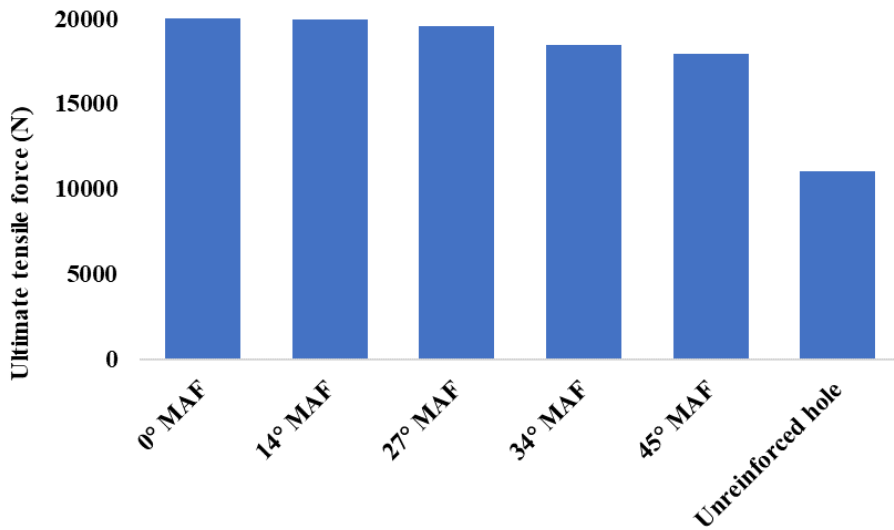


Fig. 3.8 Comparison of ultimate tensile force for MAF patterns

It was observed that all the MAF patterns successfully reinforced the hole and increased the tensile strength by at least 38.37% (reinforcement by 45° MAF). The highest reinforcement effect was observed in the 0° pattern, followed by 14°, 27°, 34°, and 45°, respectively. The difference between the ultimate tensile force of the 0° and 45° MAF observed was 11.2%.

The classical laminate theory is used to explain the behaviour of unidirectional composites, which assumes that the strength of a composite material depends on the fibre's alignment in the loading direction. When the fibres are aligned with the loading direction, they can carry the majority of the applied load and result in high strength. As the deviation of the fibre angle from the loading axis increases, the composite gradually loses its strength, and the fibres are not aligned with the direction of the applied load.

During tensile loading, stress accumulation starts at the edges of the hole, which is the weakest point in the composite. This stress accumulation causes the failure of the composite material from the hole. To prevent this, MAF patterns are incorporated into the composite material to reinforce the hole and increase the tensile strength. MAF patterns contain fibres oriented in customized directions (other than warp and weft), which deflects stress accumulation away from the hole and aligns it in the loading direction. The efficiency of MAF to deflect stress and to align increases with a decrease in the angle.

With a decrease in the MAF pattern angle, they are more aligned towards the loading axis. During the stress build-up at the hole, some of the stress is transferred by the MAF, which is in the machine grips as well, in the loading axis as they surround the hole. The MAF also experiences torque, which resists the lateral contraction in the

composite. Thus, these effects combined reinforce the hole and prevents a premature failure.

3.3.2. Effect of hole diameter on reinforcement of composites

As shown in Fig. 3.9, the plot of the ultimate tensile force of each hole diameter is presented. Six samples for each pattern were tested, and the arithmetic average of the ultimate tensile force was used in the graph.

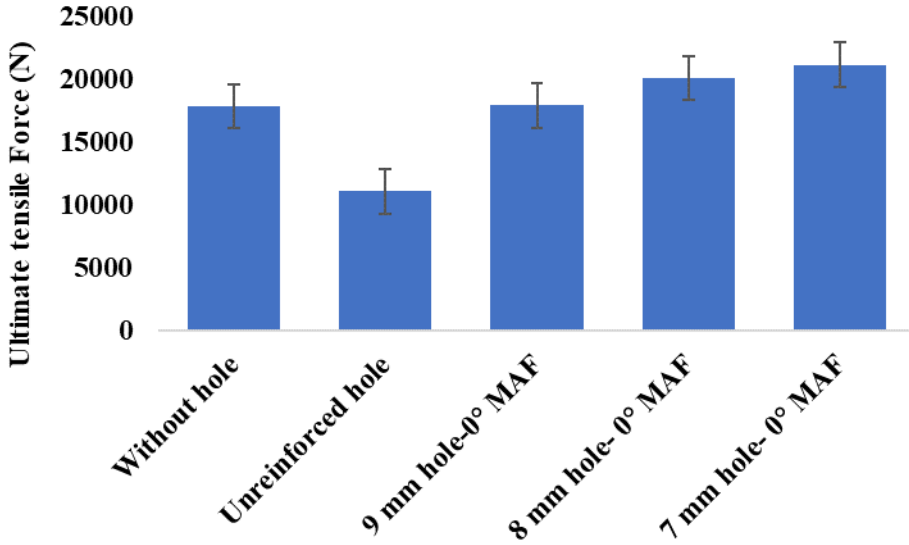


Fig. 3.9 Comparison of hole reinforcement of ORW composite

As observed from the graphs, the 0° pattern reinforces the holes of a diameter up to 9 mm. The ultimate tensile force of the 0° pattern decreases as the hole diameter increases. This can be attributed to the decrease in reinforcing fibres which are present during the tensile testing. As the hole diameter increases, more fibres are either broken or removed from the composite. In the case of an unreinforced composite, since there are no extra fibres to compensate for the loss, thus these composite samples require the lowest force for breaking. The 0° MAF reinforces the hole by compensating the loss for the broken/missing fibres, and thus an increase in the ultimate tensile force can be observed, which tends to decrease with an increase in the hole diameter.

3.3.3. Weaving of multiaxial preforms on closed reed³

Hence, an innovative solution has been developed to weave multiaxial fabrics on a conventional weaving mechanism. The MAF can be considered as a partially inserted weft, and it has multiple anchor points along the length of the fabric, as shown in Fig. 3.10. Each biased fibre requires an individual shuttle, which is different from the one used for full-width weft insertion, thus forming two separate sets of a weft

³ The material presented in this chapter has been published in [167]

insertion device. As discussed in Section 2.3.1, the MAF requires lateral as well as vertical motion. Here, the lateral shift is the inherent motion of the shuttle, while the vertical shift is achieved by adjusting the weft insertion rate. In this method, the anchor points determine the $\pm\theta$ biased angle of the overall fabric. The general steps followed for weaving are as follows:

1. Prepare the weaving as per the conventional method, including warp drawing and denting, weave designing, lifting plan, etc.
2. Calculate the number of biased fibres required, and, subsequently, the number of shuttles. In this study, 6 shuttles were used which were stored and changed manually.
3. Assign the anchor points for the biased fibres based on the $\pm\theta$ angle requirement.
4. Weave the fabric pick-by-pick, as per the lifting plan.

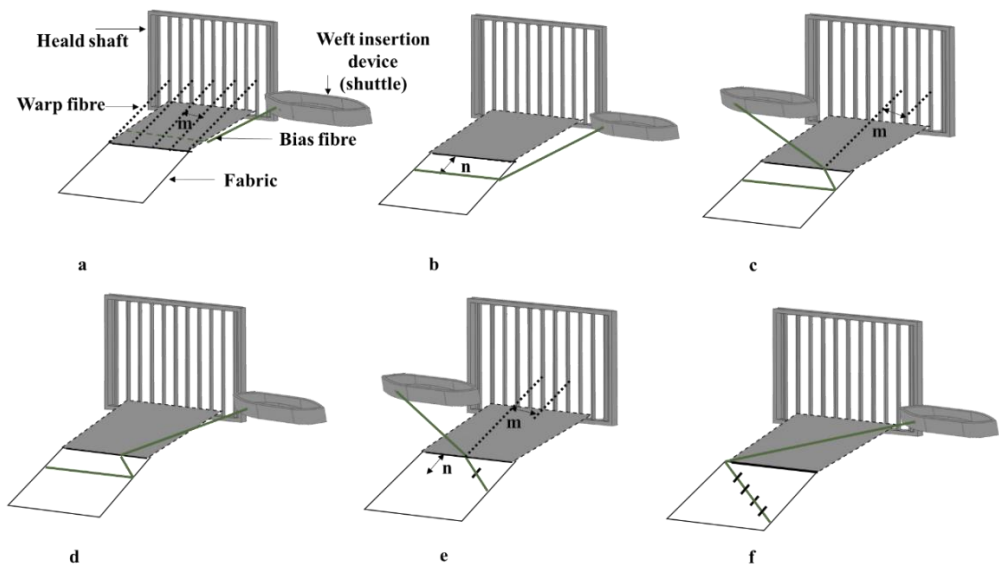


Fig. 3.10 Multiaxis weaving on closed reed loom: a) anchoring of bias fibre to base fabric, b) advancement of fabric by n weft insertions, c) anchoring of bias fibre at m distance from selvage, d) return of the shuttle to the starting point, e) advancement of the anchor point, f) reversal of the direction for anchoring bias fibre [167]

Carbon fibres *AS4TM* of 200 tex 3K *HexTow[®]* supplied by *R&G Faserverbundwerkstoffe GmbH[®]* were used as the warp, the weft, and the MAF to weave a multiaxial fabric on a 24 heald shaft dobby machine. The measured angle of the MAF with the warp was 45° . In reference to Fig. 3.10, the steps to weave a multiaxial fabric are described as follows:

Step 1. The shuttle is passed through the full width of the fabric to initially grip the biased fibre, as shown in Fig. 3.10a.

Step 2. The bias fibre is stationary for n number of weft insertions, as shown in Fig. 3.10b.

Step 3. The starting point for the indexing of the biased fibre can be either from the selvedge or from a point interior in the fabric, away from the selvedge. In this presentation, the latter case is demonstrated where the biased fibre is positioned in the interior of the fabric with the warp at m distance apart from the selvedge, as shown in Fig. 3.10c.

Step 4. To orient the biased fibres at the required angle, it is important that weft insertion should be only in a single direction, i.e., either right-left, *OR* left-right. In this step, the shuttle is brought to its initial position without inserting the weft, as shown in Fig. 3.10d.

For advancing the bias fibre, steps 2–4 are repeated, as shown in Figs. 3.10e and 3.10f. When the biased fibres reach the selvedge, a reversal of the path is achieved by reversing the direction of the shuttle insertion, reversing the order of the anchor points, and repeating steps 2–4. These steps are further applied to multiple shuttles to weave the whole biased fabric. Out of multiple shuttles, only one bias fibre shuttle is inserted at a time to avoid anchoring of a single bias fibre at multiple points.

The process of creating a biased angle involves shifting a fibre at predetermined intervals between the warp and the weft. The biased angle θ , as shown in Fig. 3.11c, is the angular distance between the warp and the biased fibre.

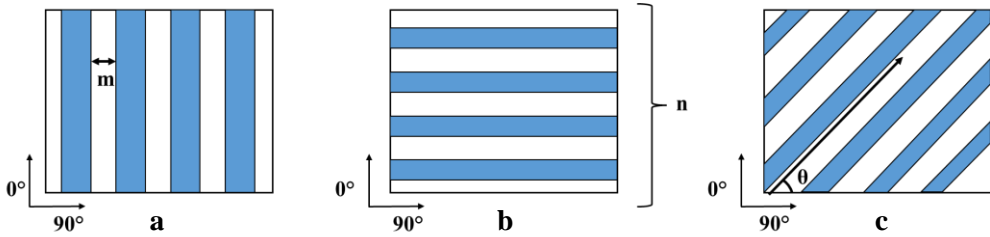


Fig. 3.11 Conceptualization of bias weaving parameters: a) distance between anchoring warp fibres m , b) number of inserted weft fibres n , c) angle θ between the warp and the bias fibre [167]

To calculate the biased angle θ and the float length of the biased fibre, we need to know the distance between the warp assigned for anchoring the biased yarn m and the number of the intervals of the inserted weft that the biased yarn is anchored at n , as shown in Fig. 3.11. In this case, both values are given as 10 mm. Equation (2.4), as discussed above in this section, can be used to calculate the biased angle θ . By using the given values of $m = 10$ mm and $n = 10$ mm, we get the value of 45° . The following equation can be used to calculate the float length of the biased fibre l :

$$l = \sqrt{n^2 + m^2} \quad (3.1)$$

By using the given values of $m = 10$ mm and $n = 10$ mm, we get $l = 14.1$ mm. Therefore, the resultant angle θ is 45° with a float length of 14.1 mm.

3.3.4. Manufacturing of multiaxial composite

The matrix in use was *Biresin CR-122 Bisphenol F* epoxy resin and an amine hardener supplied by *Sika GmbH* (Germany). The reinforcement used for the composites included bias woven and plain-woven carbon fabrics. The bias woven fabric was used to provide strength in diagonal directions, while the plain-woven fabric provided strength in the horizontal and vertical directions.

The hand layup technique involves manually placing the layers of reinforcement onto the surface of the mold which are left to harden for 24 hours under vacuum pressure at room temperature. The vacuum pressure helped to remove air and excess resin from the composite, which resulted in a more uniform and stronger material.

After the initial curing process, the composites were post-cured in an oven at 80°C for 5 hours. This step helps to improve the strength and durability of the composites by promoting further chemical reactions between the resin and the hardener. The sample code and the stacking sequence of the composites are detailed in Table 3.6.

Table 3.6. Stacking sequence and sample codes

Sample code	Stacking sequence	Thickness
S ₁	[0] ₄	0.85 mm
S ₂	[45/0/0/0]	0.85 mm
S ₃	[45/0/0/45]	0.85 mm
S ₄	[*0 ₄₅ /0/0/0]	0.85 mm
S ₅	[*0 ₄₅ /0/0/*0 ₄₅]	0.94 mm

* 0₄₅ – multiaxial fibres integrated on plain woven fabric

To study the effect of biased yarns on the out-of-plane properties of the composite, impact testing was performed on a *Coesfeld*® low velocity impact machine in accordance with the ISO 6603-02 Standard. The composite samples were cut into squares of dimensions 60 × 60 mm and fastened with a clamp of an inner diameter of 40 mm. An impactor weighing 5.18 kg of a diameter of 20 mm was dropped from a height of 0.4 m onto the sample, which resulted in a total energy of 20 J.

During the impact test, a piezoelectric sensor was placed near the clamp to measure the force and the deflection of the sample. The force and deflection data was used to analyze the response of the composite in order to impact and determine its out-of-plane properties. This information is important for understanding the behaviour of the composite under external loads and for designing the structures requiring high impact resistance.

3.3.5 Impact testing of multiaxial composite manufactured by closed reed

The force-time curves for cross and angle ply laminates were compared, and the results are presented in Fig. 3.12. Both samples showed yielding followed by stable

crack growth, which is a typical behaviour of composite materials subjected to impact loading. However, the results indicated that sample S₂ had a lower contact force compared to S₁. This reduction in the contact force can be attributed to the increased difference in the bending stress between dissimilar plies, as illustrated in Fig. 3.12a. Specifically, the angle plies have a higher bending stress compared to the cross plies, which leads to higher deformation and stress concentration at the interface between the two plies. This can cause delamination and reduce the overall strength and stiffness of the composite material. The impact testing results of all the samples are presented in Table 3.7.

Table 3.7. Impact testing results of carbon fibre composites

Sample	Maximum impact force (kN)				
	S1	S2	S3	S4	S5
1	1.603	1.486	1.308	1.614	1.423
2	1.735	1.584	1.309	1.916	1.810
3	1.548	1.481	1.341	1.718	1.751
4	1.675	1.356	1.355	1.423	1.685
5	1.489	1.398	1.412	1.562	1.786
Average	1.61	1.46	1.35	1.65	1.69
Coefficient of variation	0.05	0.05	0.03	0.10	0.08

Furthermore, the introduction of a second ply oriented at a 45° angle in sample S₃ caused a further decrease in the peak contact force, as shown in Fig. 3.12b. This trend suggests that an increased dissimilarity between the plies can negatively impact the contact force and the overall mechanical performance of the composite material. Specifically, the introduction of an angle ply at 45° introduces an additional source of stress concentration, which leads to a reduced load bearing capacity and an increased likelihood of failure.

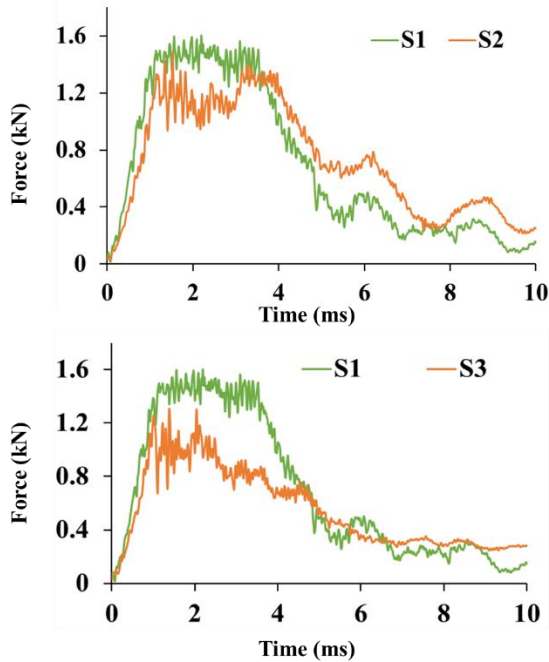


Fig. 3.12 Force-time history comparison of: a) S_1 with S_2 , b) S_1 with S_3 [167]

Fig. 3.13 depicts the force-time curves of S_4 and S_5 in comparison to S_1 . The dissimilarity between the plies in the composite material is eliminated by weaving the bias fibres with a plain weave base. At the point of the peak contact force, the bias fibre provides additional reinforcement to the plain-woven ply, which is observable in Fig. 3.13a as an increase in the peak load. Furthermore, the addition of a second multiaxial ply in S_5 further enhances the reinforcing effect of the bias fibre, as illustrated in Fig. 3.13b.

These findings are consistent with the previous research that has investigated the effect of the alignment of fibre directions close to warp fibre [66, 71]. By weaving the bias fibres with a plain weave base, the dissimilarity between the plies is reduced, which leads to an increase in the peak load at the point of the contact force. Moreover, the reinforcing effect of the bias fibre is further amplified by adding a second multiaxial ply, which results in an even higher level of reinforcement and an improved load bearing capacity.

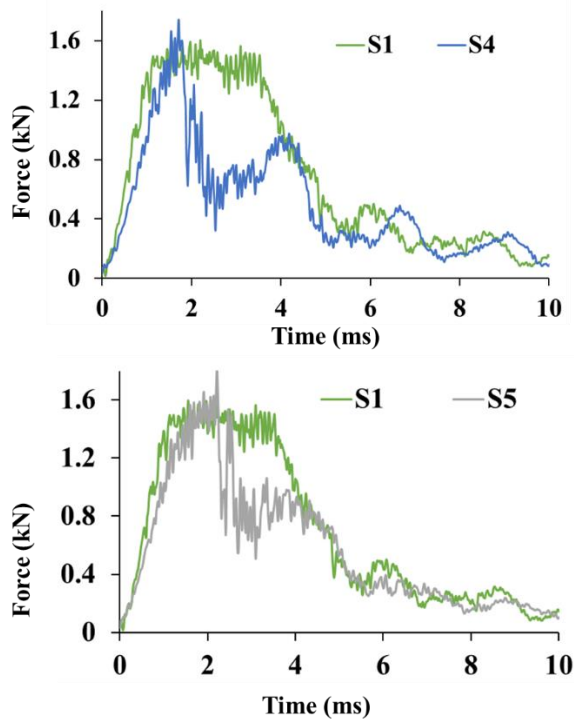


Fig. 3.13 Force-time history comparison of: a) S_1 with S_4 , b) S_1 with S_5 [167]

Impact loading is a complex process involving the breaking and tearing of the fibres, matrix damage, and delamination of composite materials under both tensile and compressive loads. This damage mechanism occurs because the sudden application of the load leads to a stress wave propagating through the composite material, which causes localized deformation and damage. The resulting damage can compromise the strength and stiffness of the material, thus leading to a potential failure.

Previous research on the impact properties of carbon composites has shown that the plain-woven ply, with fibre directions of 0° and 90° , exhibits the highest capacity.

Furthermore, it has been shown that the stacking sequence of composite materials can have a significant impact on their mechanical properties. By varying the stacking sequence, it is possible to optimize the mechanical performance of the material for specific applications. For example, in applications requiring high impact resistance, the plain-woven ply is often the preferred stacking sequence. On the other hand, in applications requiring high stiffness and strength, other stacking sequences may be preferred. The results of the force-time curve comparison for S_4 and S_5 further emphasize the potential benefits of using bias fibres with a plain weave base and a multiaxial ply in composite material manufacturing to enhance their mechanical performance.

3.3.6 Summary of research findings from mechanical characterization of multiaxial composites

This study aimed to investigate the reinforcement effect of multiaxial composites made by employing two different weaving techniques. The first weaving method used a *Dornier* ORW machine to weave MAF in five different patterns, where 1200 tex glass fibres were oriented in increasing angles of 0°, 14°, 27°, 34°, and 45° with respect to the warp threads, while maintaining the base weave as plain. The resulting multiaxial woven plies were sandwiched between the plain woven glass fibre plies of 600 gsm and infused with the *RIMR 426* epoxy resin system to manufacture composites. After curing at 80 °C for 8h, the glass fibre composites were tabbed and cut into 250 x 25 mm dimensions for tensile testing, while following the ISO 527-4 test standard.

To examine the effect of reinforcement by the MAF patterns, a 5 mm hole was drilled at the centre of the test coupon. The tensile testing results of each MAF pattern were compiled and analyzed, with the following findings:

All MAF patterns were successful in reinforcing the 5 mm hole, with the highest reinforcement seen in the 0° MAF pattern, whereas the least reinforcement was observed in the 45° MAF pattern. The 0° MAF pattern increased the ultimate tensile force by 44% compared to the unreinforced hole, while the 45° MAF pattern increased it by 38.37%.

The hole drilled in the composite reduced the ultimate tensile force of the pristine composite (without a hole and without the MAF pattern) by 38%.

The MAF patterns were found to deflect the stress accumulation arising at the hole towards the loading axis, thereby reinforcing the hole by compensating for the broken fibres. Less deviation of the MAF from the warp increased the reinforcing effect of the hole.

The 0° MAFs were able to reinforce a hole up to 9 mm in diameter without compromising the tensile strength of the pristine composite. The MAF compensates for the loss of the fibres due to the drilling of a hole.

Overall, the study successfully characterized the multiaxial composites made by employing the ORW technique and demonstrated that the MAF patterns could effectively reinforce holes in the composites. The 0° MAF pattern provided the highest level of reinforcement, while the 45° MAF pattern showed the least reinforcement. The findings contribute to the development of improved composite materials with enhanced mechanical properties.

The second method of this research work was to develop a new technique for manufacturing multiaxial composites and to evaluate their impact strength. The method involved the use of carbon fibres of 200 tex as MAF and weaving them on the surface of a plain-woven fabric by using multiple shuttles, with the help of the closed reed on a conventional weaving mechanism. The composites were manufactured by placing multiaxial plies on top of 3 plies of 160 GSM plain woven carbon fabric and infusing them with bisphenol F epoxy resin by using the hand layup method. The multiaxial composites were then subjected to impact loading at 20 J energy and compared to cross and 45° angle ply stacked laminated composites. The impact results

were plotted as the force-time history, computed with a piezoelectric sensor at the clamp. The study produced the following findings:

The partial insertion of weft at predetermined intervals has been proven to be a feasible method for manufacturing multiaxial composites. This method did not require complex modifications to the weaving loom and could be carried out on a conventional closed reed with a jacquard/dobby attachment coupled with a multiple weft insertion system.

The impact force of multiaxial composites was found to be higher compared to plain woven composites. This indicates that the addition of bias fibres on the surface of plain-woven fabric improved the impact resistance of the composite as the difference in the bending stiffness of the plies was minimal.

3.4 Finite Element Analysis of Multiaxial Composites

3.4.1 Static structural analysis of ORW composites

The results of the static structural analysis of the tensile testing of ORW composites shall be discussed in this section. Fig. 3.14 shows the simulated stress and the actual stress on the composite samples when using the maximum stress and the maximum strain theory.

The stress distribution of MAF patterns from Fig. 3.14 a–f clearly shows that, as the MAF angle deviates from the warp, the stress starts to build up near the hole. Fig. 3.14f shows that, for 45° MAF, the stresses are concentrated near the hole and MAF; however, as the angle nears 0°, the stresses are uniformly distributed in the whole length of the composite samples. Visual analysis of the damaged samples shows that matrix cracking and fibre debonding occurred in the zones where stress was accumulated. This can be observed as bands with a higher brightness in the experimental results are visible in Fig. 3.14. The zones of low stress concentration were not affected, and thus remained undamaged. The simulation results in Fig. 3.14 denote the low stress concentration zones in the blue color whereas higher stress concentration with the green or yellow color, which is well collaborated with the experimental results. The stress values calculated near the hole are plotted in the chart, as shown in Fig. 3.15. It can be observed that the MAF reinforces the hole by decreasing the stress values, which shows an increasing trend as the MAF angle increases.

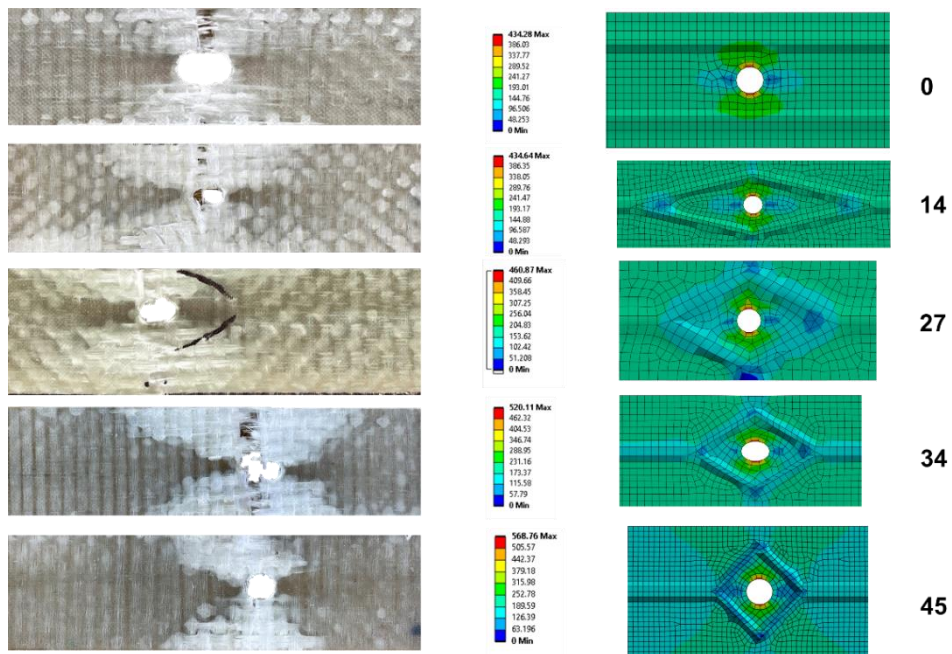


Fig. 3.14 Experimental and simulation results of tensile testing

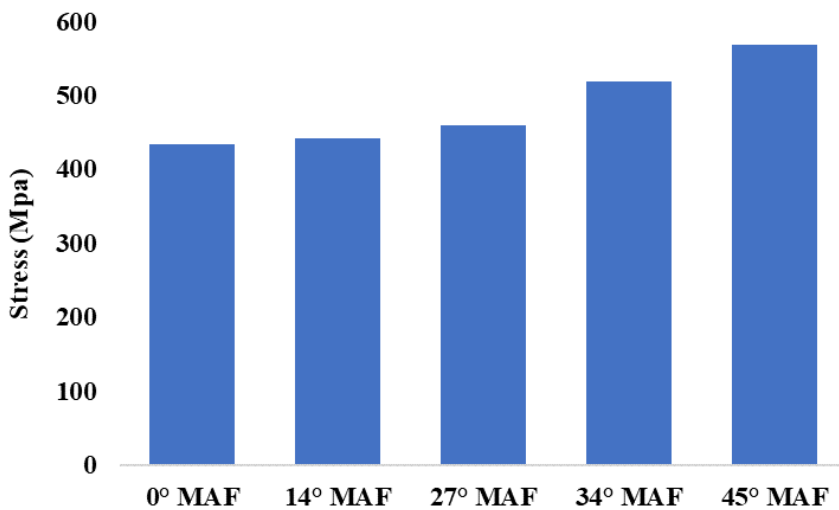


Fig. 3.15 Bar chart for stress values at the edge of the hole

The stress distribution in the simulation is well-corroborated with the experimental results, as discussed in Section 3.3.2. As shown in Fig. 3.14, the 45° MAF composite shows that the stresses at the break were concentrated mainly near the MAF and the hole, whereas it also shows that, for 0° MAF, the stresses were

distributed well towards the grips of the sample. The low stresses arising in the loading direction near the hole were also well predicted by the FEA. Fig. 3.16 shows the stresses arising in the individual MAF ply in the composite, which also shows a trend of an increase in the distribution of stresses as the fibre angle nears towards the warp.

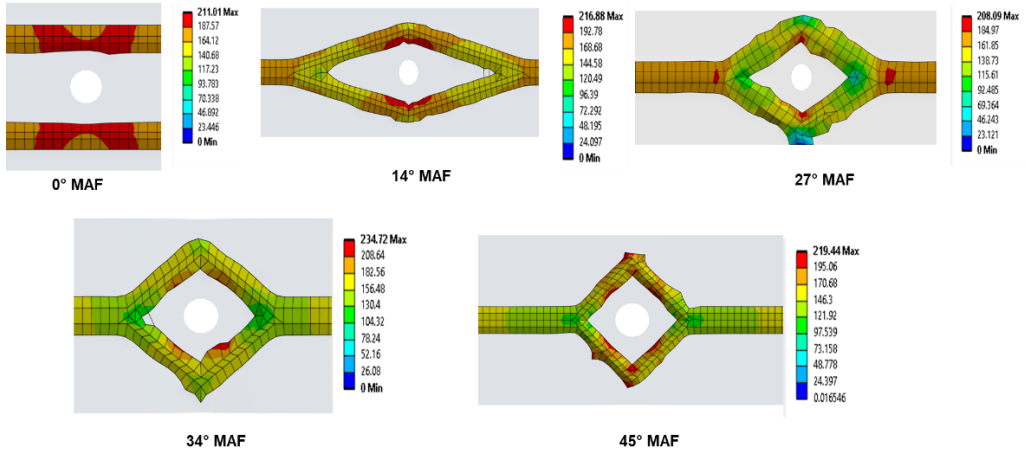


Fig. 3.16 Stress distribution of individual MAF ply

3.4.2 Finite element analysis of impact loading of carbon composite

The numerical modelling described in Section 2.4.5 involved the use of the Hashin failure criteria to simulate the behaviour of composite materials during the drop weight impact testing. The force moment data obtained from explicit dynamics was plotted against the experimental values obtained during the drop weight impact testing of carbon composites. The simulation results are presented in Fig. 3.17, which shows good agreement with the experimental data obtained from the actual testing. The model was able to accurately capture the force-time history of the composite specimen in both the elastic and the nonlinear plastic regions.

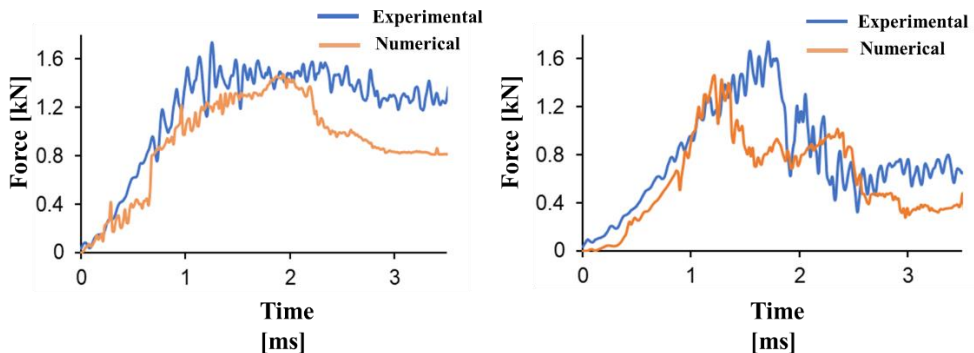


Fig. 3.17 Comparison of experimental and numerical results of impact loading: a) plain woven, b) multiaxial woven [167]

Moreover, the difference in the peak force values between the simulation and the experimental results was found to be relatively small, with a discrepancy of 3% observed for the plain-woven composite, and 5% for the multiaxial woven composite. This small difference can be attributed to the presence of errors during the testing, as well as machine vibration which can affect the accuracy of the results. In reality, the composite specimen is not perfectly gripped by the testing machine during the experiment, which can result in some degree of movement and deformation that is not captured in the simulation.

3.4.3 Summary of the research findings for FEA of multiaxial composites

The research discussed in this section focuses on the static structural analysis of the tensile testing of glass fibre ORW composites as well as the explicit dynamic simulation of impact loading of a carbon fibre composite. For the static structural analysis, a 1 mm constant deflection was applied to the geometry, and the equivalent von Mises stress was calculated at the hole and near the gripping points. The stress distribution of the MAF patterns was analyzed. For the explicit dynamics of carbon composites, the impactor of a 20 mm diameter was assigned 5.186 kg load and 2.1 m/s velocity to the impact on a composite plate of 60 x 60 mm dimensions. The research findings of the study can be summarized as follows:

It was observed that as the MAF angle deviates from the warp, stress starts to build up near the hole. The stress values calculated near the hole were plotted on a chart which showed that the 0° MAF provided the highest reinforcement of the hole by decreasing the stress values, while 45° MAF reinforced the least.

The stress distribution in the simulation was well corroborated with the experimental results. The low stresses arising in the loading direction near the hole were also well predicted by the FEA.

The stresses arising in an individual MAF ply in the composite showed a trend of an increase in the distribution of the stresses as the fibre angle neared towards the warp. Overall, the research provides valuable insights into the stress distribution of ORW composites under tensile testing, which could inform the design of these materials for various applications.

In the numerical modelling study of impact loading on multiaxial carbon fibre composites, the Hashin failure criteria have been used to simulate the behaviour of composite materials during the drop weight impact testing. This type of testing involves dropping a weight onto a composite specimen and measuring the force and the displacement response. The simulation results were compared to the experimental data obtained from the actual testing of carbon composites.

The simulation results presented in Section 3.4.2 showed good agreement with the experimental data, by capturing the force-time history of the composite specimen in both the elastic and the nonlinear plastic regions. The difference in the peak force values between the simulation and the experimental results was relatively small, with a discrepancy of only 3% observed for the plain-woven composite, and 5% for the multiaxial woven composite. This indicates that the simulation model was able to

provide an accurate approximation of the impact behaviour of the composite materials.

Overall, the study demonstrates the usefulness of numerical modelling in providing insight into the impact behaviour of composite materials. This type of modelling can be particularly valuable in informing the design of composite structures subjected to similar loading conditions. However, it is important to recognize the limitations of the modelling approach and the potential sources of error in both the simulation and the experimental data.

4. CONCLUSIONS

The following conclusions can be derived from the research results generated during the research work:

1. Glass fibre orthogonal 3D woven composites embedded with a carbon nanotube for structural health monitoring have been developed. The carbon nanotube transfer method from porous media to the fabric preform under vacuum pressure results in uniform dispersion of the carbon nanotube in the resultant composites. The vacuum pressure of 101.3 kPa results in the infusion of the carbon nanotube through the thickness of the fabric, while 30.3 kPa results in the partial infusion of the carbon nanotube.
2. Glass fibre 3D woven T-profile composites doped by MXene nanoparticles have been developed. A coating of 10 layers of 3.3 mg/mL concentration of MXene dispersion in water is effective to build a conductive layer of $10^5 \Omega$.
3. Multiaxial composites have been designed and developed by the open and closed reed weaving method. A *Dornier* open reed weaving loom was used to weave glass fibres of 1200 tex in five different patterns to reinforce a 5 mm hole. The angle of the multiaxial fibre progressively increased from 0° to 45° across 5 patterns. In the second method, a new technique for weaving multiaxial preforms by using carbon fibres of 200 tex as multiaxial fibres on a closed reed weaving mechanism has been developed. This method was able to successfully produce multiaxial preforms with 45° orientation of the constituent carbon multiaxial fibres without complex modifications in the existing weaving mechanism.
4. The carbon nanotube layer infused through the thickness was able to sense damage and deformation under tensile loading conditions by changing its resistance values corresponding to the applied strain to the orthogonal 3D woven composite. Similarly, the partially infused carbon nanotube layer was able to sense damage and deformation under flexural loading conditions of the glass fibre orthogonal 3D woven composite. The MXene coated glass fibre 3D woven T profile composite was able to sense displacement and damage during tensile loading up to 2140 N, as well as during fatigue loading of 6000 cycles at 0.5 Hz and 50 N, as well as at 1 Hz and 100 N, respectively.
5. The tensile testing of ORW multiaxial composites showed that the 0° multiaxial fibre pattern provided the highest level of reinforcement, by increasing the ultimate tensile force by 44%, and the multiaxial fibre patterns deflected stress accumulation arising at the hole towards the loading axis. The multiaxial composites manufactured by the closed reed method were found to reinforce the carbon fibre composite by 6% under the impact loading conditions.

6. The simulation model to evaluate the mechanical behaviour of multiaxial composites has been developed. Finite element analysis was carried out by using static structural analysis of the tensile testing of glass fibre open reed woven composites and explicit dynamic simulation of the impact loading of carbon fibre composites. The stress values near the hole in open reed woven composites increased as the multiaxial fibre angle deviated from the warp, which is well corroborated with the experimental results. The simulation results of the impact loading of a multiaxial carbon fibre composite by closed reed were in good agreement with the experimental data, with a discrepancy of 3% for the plain-woven composite, and 5% for the multiaxial woven composite.

5. ANOTACIJA

Įvadas

Pastaraisiais metais kompozitinių medžiagų srityje buvo įvykdyti dideli pasiekimai. Pagrindinis dėmesys skirtas naujų ir inovatyvių medžiagų, kurios galėtų būti naudojamos aviacinėje, kosminėje, civilinės inžinerijos ir kitose pramonės srityse, kūrimui. Kompozitinių medžiagų arba kompozitų ir daugiaašių kompozitų struktūrinė sveikatos stebėseną (SSS) yra viena iš daug žadančių sričių. Čia šiuo metu kuriami kompozitai, galintys vietoje aptikti pažeidimus, ir pažangūs kompozitai su daugiau nei 2 kryptimis integruotu pluoštu.

Kompozitų SSS – tai struktūrinio vientisumo ir kompozitinių medžiagų veikimo stebėseną naudojant įvairius metodus ir technologijas. Kompozitai – tai iš dviejų ar daugiau skirtingų komponentų sudarytos medžiagos (paprastai matrica ir armuojanti medžiaga), kurios kartu sudaro geresnes mechanines savybes turinčią medžiagą. Tačiau joms irgi gali būti pakenkta, pavyzdžiui, jos gali būti išsluoksniuotos, gali būti pertrauktas jų pluoštas, gali įskilti matrica, jos gali prisigerti drėgmės, o tai per laiką stipriai paveikia jų mechanines savybes ir struktūrinį vientisumą. Kompozitų SSS metodai paprastai apima jutiklių naudojimą, duomenų gavimo sistemas ir analitinius algoritmus, padedančius stebėti kompozitų struktūrą, aptikti galimą žalą ar nuvertėjimą ir iš anksto nuolat arba periodiškai įspėti apie struktūrinius klausimus. Vieni dažniausių kompozitų SSS metodų: įtempimo jutikliai, garso sklaidimo jutikliai, ultragarso jutikliai, termografija, vibracijos analizė, pjezovaržos jutikliai, duomenų analizė ir mašininis mokymasis. Iš visų šių metodų kompozito SSS naudojami elektrinės varžos jutikliai buvo plačiai tyrinėjami taikant labai daug skirtingų nanodalelių, pavyzdžiui, anglies nanovamzdelius (ANV), grafeną, makseną ir pan., skirtingais kompozito gamybos etapais.

ANV – tai nanolygio cilindrinės struktūros, sudarytos iš anglies atomų, o maksenai – dvimatės medžiagos, gautos selektyviai ėsdinant titano karbido MAX fazę. Šios nanodalelės pasižymi dideliu elektros laidumu ir pjezovarža, kas naudinga kompozitų SSS. Be to, buvo nustatyta, kad šios nanodalelės sustiprina kompozitų mechanines savybes, dėl ko jos gali puikiai aptikti kompozitams padarytą žalą.

Nors kompozitų SSS, naudojant nanodaleles, buvo tiriama dirbant su dvimačiais sluoksniuotais kompozitais, tačiau dar labai trūksta šių nanodalelių elgsenos tyrimų, kai jos įstatomos į trimačius austinius kompozitus. Trimatis audimas – tai būsima kompozitų gamybos sritis. Pluoštai bus integruojami 3 kryptimis išankstinio formavimo audimo etapo metu, kad iš anksto būtų išvengta bet kokių sluoksnių. Trimačiai austiniai kompozitai pašalina išsluoksniavimą ir pasižymi geresnėmis mechaninėmis savybėmis nei dvimačiai sluoksniuoti kompozitai.

Daugiaašiai kompozitai – dar viena būsima kompozitų gamybos sritis. Čia pluoštas išankstinio formavimo gamybos etape integruojamas daugiau nei 2 kryptimis. Įprastas daugiaašio išankstinio formavimo procesas – tai pluošto mezgimas, pynimas arba audimas. Iš jų audimas pasižymi didžiausiu matavimo stabilumu. Tačiau, audžiant daugiaašius kompozitus įprastomis audimo staklėmis, atsiranda didelių iššūkių, pavyzdžiui, netytys ir skietas trukdo indeksuoti daugiaašį

pluoštą reikalingu kampu. Norėdami įveikti šį iššūkį, tyrinėtojai sukūrė inovatyvius metodus ir pakeitė audimo stakles taip, kad pluoštas galėtų būti naudojamas daugiau nei 2 kryptimis. Vienas iš būdų, kaip išausti daugiaašes formas, – tai atviro skieto naudojimas ant įprastų audimo staklių. Toks skietas turi atvirus krumplius, o uždaro skieto ant tradicinių audimo staklių krumpLIAI yra uždaryti abiejose pusėse. Atviras skietas turi specialius krumplius daugiaašiam pluoštui ir specialius nyčių velenus, leidžiančius judėti 2 ašimis.

Nors egzistuoja daug skirtingų daugiaašių formų audimo metodų, tačiau naujų daugiaašių formų gamybos metodų raidoje yra spragų. Be to, labai trūksta mechaninių daugiaašių kompozitų savybių ir daugiaašio pluošto teorinio bei praktinio poveikio įprastiems kompozitams tyrimų.

Šiuo tyrimu buvo siekiama išsiaiškinti trimačių austinių kompozitų su ANV ir makseno nanodalelėmis panaudojimo SSS sistemose galimybes bei ištirti jų elgseną tempimo, lenkimo ar nuovargio apkrovos sąlygomis. Be to, buvo pasiūlyti ir pažangūs daugiaašių austinių kompozitų gamybos metodai bei ištirtos šiais metodais pagamintų kompozitų mechaninės savybės.

Tyrimo tikslas ir uždaviniai

Šio tyrimo tikslas yra sukurti, ištirti ir pagaminti saviagnostinius trimačius austinius ir daugiaašius kompozitus. Šiam tikslui pasiekti numatyti šie uždaviniai:

1. Sukurti stiklo pluošto trimačius austinius kompozitus su ANV.
2. Sukurti stiklo pluošto trimačius austinius T profilio kompozitus su makseno nanodalelėmis.
3. Suprojektuoti ir sukurti daugiaašius kompozitus, taikant atviro ir uždaro skieto audimo metodą.
4. Ištirti trimačių austinių kompozitų SSS efektyvumą, stebint elektromechaninį atsaką tempimo, lenkimo ir nuovargio bandymų metu.
5. Ištirti daugiaašių kompozitų elgseną tempimo ir smūginio apkrovimo metu.
6. Sukurti skaičiuojamąjį modelį, padėsiantį įvertinti mechanines daugiaašių kompozitų savybes.

Mokslinis naujumas

1. Buvo sukurtas naujas metodas, kaip įtraukti ANV į stiklo pluošto trimačių austinių kompozitų lokalizuotą vietą naudojant poringas medžiagas. Šis metodas padėjo sumažinti ANV kiekį, reikalingą veiksmingai trimačių austinių kompozitų SSS, taip sutaupant medžiagų kaštus.
2. Buvo pagamintas naujas stiklo pluošto trimatis austinis T profilio kompozitas, į sujungimo vietą įdedant makseno nanodalelių. Šis metodas buvo sėkmingas aptinkant kompleksiniams kompozitams padarytą žalą vietoje.
3. Buvo sukurtas naujas metodas, kaip austi daugiaašes formas su uždaru skietu, taip panaikinant poreikį atlikti kompleksinius pakeitimus tradicinėse audimo staklėse.

Praktinė reikšmė

Šis tyrimas yra reikšmingas, nes gali pasiūlyti naujas ir inovatyvias kompozitines medžiagas SSS sistemai ir padėti siekti pažangos daugiaašių kompozitų srityje. Šio tyrimo rezultatai leistų pagerinti struktūrinę saugą ir patikimumą įvairiose pramonės srityse ir geriau suprasti trimačių austinių kompozitų su ANV ir makseno nanodalelėmis elgseną apkrovos sąlygomis, pavyzdžiui, tempimą, lenkimą ir nuovargį. Kita vertus, naujas daugiaašių kompozitų gaminimo metodas audžiant išankstines formas uždaru skietu galėtų padėti masinei gamybai. Be to, stiklo pluošto daugiaašių kompozitų tyrimų rezultatai gali labai pagerinti kompozitų dizainą, nes angos bus tvirtesnės, o kaina išliks konkurencinga.

Gynimo teiginiai

1. Vakuuminio perdavimo būdu ant stiklo pluošto trimačio austinio kompozito integruoti ANV gali veikti kaip pažeidimų jutiklis tempimo ir lenkimo apkrovos sąlygomis. Per porėtą medžiagą, taikant vakuuminį slėgį, perduoti ANV nėra filtruojami stiklo pluošto.
2. Makseno nanodalelės, įtrauktos į stiklo pluošto trimačius austinius T profilio kompozitus, gali aptikti pažeidimus tempimo ir nuovargio apkrovos sąlygomis. Užpurškus makseno nanodalelių ant T profilio kompozito sujungimo, palengvėja gamyba ir sunaudojamas minimalus makseno kiekis.
3. Daugiaašiai kompozitai, kurių pluoštas integruotas daugiau nei 2 kryptimis, padeda apibrėžti mechanines kompozitų savybes. Atviro ir uždaro skieto būdu pagaminti daugiaašiai kompozitai gali sustiprinti anglies kompozitus smūginės apkrovos sąlygomis, o stiklo pluošto kompozitus – tempimo apkrovos sąlygomis.

Tyrimo rezultatų paskelbimas

Šio tyrimo rezultatai buvo pristatyti trijuose ekspertų įvertintose publikacijose žurnaluose, pateikiamuose CA WoS duomenų bazėje, ir vienoje ekspertų įvertintoje publikacijoje prie konferencijos medžiagos. Be to, eksperimentiniai rezultatai pristatyti trijose tarptautinėse konferencijose.

Disertacijos struktūra ir planas

Disertacija yra suskirstyta į penkis skyrius, įskaitant įvadą, literatūros apžvalgą, medžiagą ir metodus, rezultatus ir jų aptarimą bei išvadas. Įvade trumpai apžvelgiamas tyrimas ir jo tikslai, prie literatūros apžvalgos pateikiama atitinkama bazinė informacija ir pristatomi ankstesni šios srities tyrimai. Metodologijos skyriuje pristatomi tyrimo metu naudoti metodai ir būdai, o rezultatų skyriuje pateikiami ir analizuojami rezultatai. Aptarimo skyriuje tyrinėjamos rezultatų reikšmės, o prie išvadų apibendrinami pagrindiniai radiniai ir pateikiamos rekomendacijos dėl būsimų tyrimų. Darbą sudaro 118 puslapių, 31 paveikslų ir 15 lentelių.

Ankstesnių tyrimų su trimačiais austiniais kompozitais, daugiaašiais kompozitais ir kompozitų SSS, naudojant ANV ir makseno nanodaleles, apžvalga

Aviacinėje kosminėje srityje kompozitai naudojami dalims pagaminti, kai keletas austinio anglinio audinio lakštų dedama ant formos, kiekvienas sluoksnis sudrėkinamas epoksidine derva arba tinkama matrica. Šis procesas, įtraukiantis uždaro formavimo metodą (RTM) arba vakuuminį uždaro formavimo metodą (VaRTM), dažnai padeda išsluoksniuoti sluoksnius, taikant tempimo ar spaudimo apkrovas. Norint išspręsti šią problemą, visas susluoksniavimas sustiprinamas siūlėmis, Z ašies pluošto armavimu arba dygsniais, o trimačio audimo metodas panaikina sluoksnių poreikį, sujungdamas juos į vieną išankstinę formą [1-10]. Du pagrindiniai trimačių audinių audimo būdai yra kampų sujungimas ir stačiakampis sujungimas. Kampų sujungimo audimo metodas – tai trimatis audimo metodas, kai gijos ar pluoštas sujungiami atitinkamu kampu, sukuriant stabilią nešančiąją konstrukciją. Kampinio sujungimo audimui reikia pakeistos dvimačio audimo mašinos, galinčios pakeisti gijų kelią audimo proceso metu [11-22].

Stačiakampis trimatis audimas – tai trimatis audinio formavimo procesas, kurio metu gaunamas sluoksnis be trimačio audinio, rišančiomis gijomis sujungiant linijines gijas. Skirtingai nei trimačio proceso metu, nepinamos jokios gijos, išskyrus rišančiąsias. Nustatyta, kad stačiakampis trimatis austinis kompozitas veikia geriau nei kampu sujungti kompozitai [23-38].

Aviacinėje kosminėje srityje reikia papildomų įstrižų gijų, kad būtų pagerintos kirpimo savybės. Jos dedamos įstrižiniu kampu θ pagrindinei apmatų linijai. Įstrižinės gijos periodiškai praeina pločio / ataudų kryptimi ir įtraukiamos į audinį mezgant, pinant arba audžiant. Audimas suteikia geresnę struktūrinę vientisumą tokio tipo audiniui, tačiau tradicinis skietas trukdo gijoms judėti. Šiuo tikslu buvo sukurtos specialios audimo staklės ir mechanizmai, kuriems nereikia tradicinio skieto, o gijas sujungia kiti elementai. Šios mašinos naudoja įvairius gijų indeksavimo metodus, pavyzdžiui, lygius arba sriegiuotus velenus, begalinius diržą pernešančius griovelius, per kuriuos praleidžiamos įstrižinės gijos, o žingsninis variklis suka diržą, kad indeksuotų įstrižines gijas palei audinio plotį, naudodamas kreipiamojo bloko rinkinį, kurį kerta velenas. Įstrižinės gijos pereina pro šiuos blokus besisukdamos. Atviro skieto audimą sukūrė „Lindauer Dornier GmbH“, naudojanti specialų skietą, nyčių veleną ir pan. [39-46].

Kompozitų SSS naudoja jutiklius, pavaras ir kitus prietaisus, padedančius stebėti sveikatą ir kompozitinių struktūrų veikimą realiu laiku, kad galima būtų aptikti ir diagnozuoti galimą pažeidimą ir nusidėvėjimą bei iš anksto įspėti apie galimą gedimą. Tokios laidžios nanodalelės, kaip anglies nanovamzdėliai, grafeno nanoplokštelės, makseno nanodalelės ir nanosidabro dalelės bei pan., naudojamos kompozitų SSS [47-64].

Buvo atlikti išsamūs ANV kaip medžiagos, kurią galima būtų naudoti kompozitinėse medžiagose SSS tikslu, tyrimai, nes ANV pasižymi išskirtinėmis mechaninėmis, elektrinėmis ir šiluminėmis savybėmis. ANV buvo sėkmingai įtrauktos į skirtingų kompozitinių medžiagų sudėtį, taip pagerinant jų jutimines

savybes. ANV naudoti ir kuriant elektrinės varžos jutiklius, aptinkančius kompozitų mechaninių savybių pasikeitimus. Jie naudoti ir didesnio šiluminio laidumo kompozitinių medžiagų kūrimui SSS tikslu [65-86].

Makseno nanodalelės yra dvimatės medžiagos, sudarytos iš pereinamųjų metalų karbidų arba nitridų. Dėl savo paviršiaus funkcinių grupių ir dvimatės struktūros jos pasižymi išskirtinėmis mechaninėmis ir elektrinėmis savybėmis. Makseno dalelės praveda elektrą per kvanto tuneliavimą ir kontaktinę varžą ir gali būti vienodai išsklaidytos matricoje, taikant įvairius metodus, pavyzdžiui, maišymą lydinyje, *ex situ* maišymą ir polimerizaciją vietoje. Makseno nanodalelės pasižymi dideliu elektros laidumu, todėl jos tinka elektros varža pagrįstoms SSS sistemoms. Be to, jos sustiprina kompozitinių medžiagų šiluminės ir mechaninės savybes, dėl ko jos tampa idealiai tinkamos kompozitams, kuriems tenka didesnis spaudimas ir įtempimas. Dažniausiai su makseno nanodalelėmis naudojami polimerai – tai polipropilenas, polilaktinė rūgštis, poliuretanai, polistirenas ir polivinilo fluoridas [87-112].

Baigtinių elementų metodo (BEM) taikymas kompleksinio austinio pluošto sluoksninių kompozitų pažeidimo simuliacijai ir nuspėjimui smūgio ir įtempimo sąlygomis buvo labai išsamiai nagrinėtas. Kompozitai pasižymi puikia jėga, savituoju standumu ir atsparumu nuovargiui, tačiau jiems gali pakenkti mažo greičio smūginės ir įtempimo apkrovos. Smūgiai gali sukelti sudėtingus pažeidimus, pavyzdžiui, matricos įskilimą, išsluoksniavimą ir pluošto suardymą, o dėl įtempimo gali pasireikšti tokie trūkumai, kaip matricos įskilimas, matricos atpalaidavimas ir pluošto ištraukimas [113-114].

ANSYS – tai bendro pobūdžio simuliacijos programinė įranga, pritaikanti tikslią dinamiką, o „LS Dyna“ padeda spręsti smūgio problemas. Tam reikia įvesti medžiagos savybes, pradines ir ribines sąlygas bei kontaktines sąlygas. Programinė įranga leidžia naudotojams apibrėžti iki devynių papildomų kriterijų kaip naudotojo apibrėžtus pradinius kriterijus, leidžiančius nustatyti, kada ir kur atsiras medžiagos pažeidimas [115-128].

Tyrimų metodika

a) Trimačių austinių kompozitų su ANV SSS⁴

Buvo paruoštas pradinis epoksidinės dervos ir 2 % masinės dalies daugiasienių ANV, kurių vidutinis skersmuo yra 10 nm, mišinys. Miltelinės formos ANV nupirkti iš „Nanocyl®“ Belgijoje. Kompozitui naudota matrica buvo bisfenolio F derva su amino kietikliu. Trimačiai austiniai kompozitai pagaminti naudojant vakuuminę infuziją trimis skirtingais metodais. Gautiems pavyzdžiams suteikti S_i.G_n formato unikalūs kodai, kur „i“ reiškia metodą, o „n“ – grupės numerį, nurodytus 5.1 lentelėje.

5.1 lentelė. Pavyzdžių kodai ir gamybos metodai

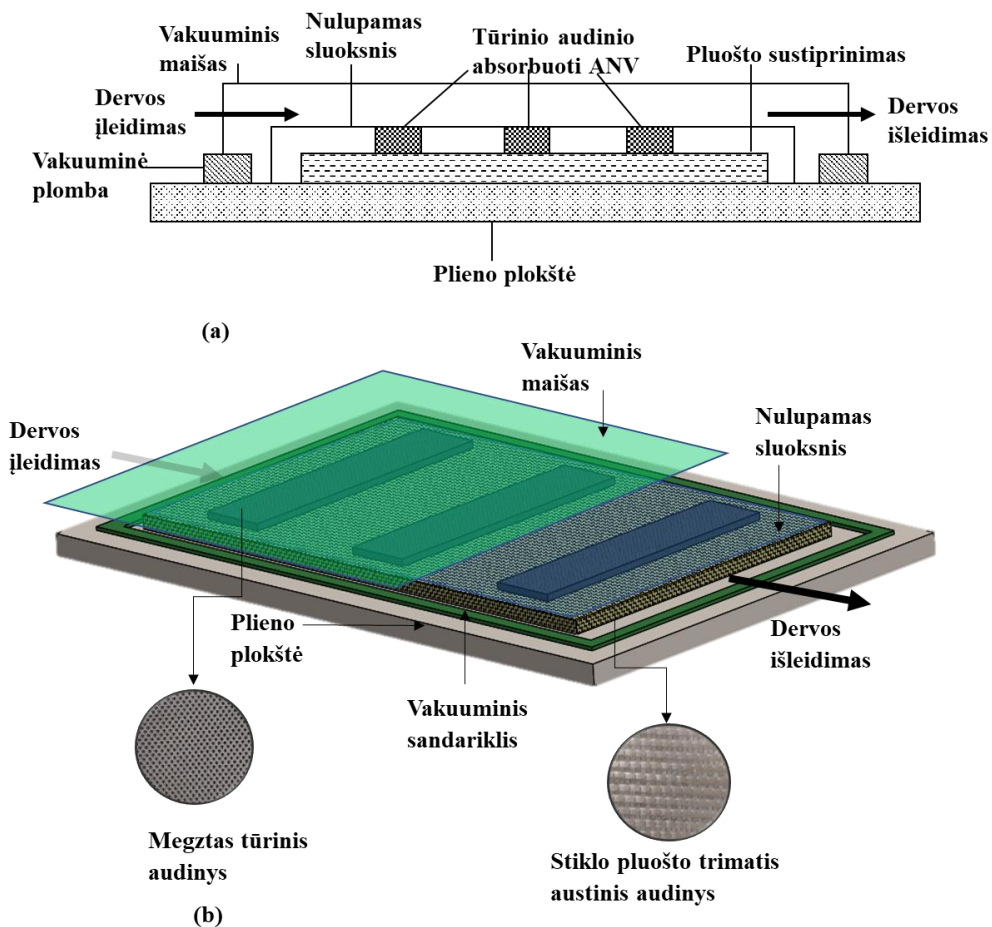
Metodas ir pavyzdžio kodas	1 metodas		2 metodas	3 metodas	
	S ₁ .G ₁	S ₁ .G ₂	S ₂	S ₃ .G ₁	S ₃ .G ₂
Išmatavimai (mm)	300 × 250	300 × 250	100 × 100	300 × 300	300 × 300
ANV išsklaidymo procesas	Liejimas	Liejimas	Infuzija	Vakuuminis perdavimas	Vakuuminis perdavimas
Vakuuminis slėgis (kPa)	101,3	101,3	101,3	101,3	0,4
„V“ formos griovelis	ANV plėvelės viduje	ANV plėvelės išorėje		Be griovelio	

1 metodo atveju švarūs trimačiai austiniai kompozitai buvo išlieti su 0,25 % masinės dalies ANV epoksidinėje dervoje. Tam naudotas valytuvus. Liejiniai buvo palikti kambario temperatūroje 12 valandų, kad sukietėtų, o vėliau jie buvo apdoroti 80°C krosnyje 5 valandas.

2 metodo atveju į trimatį austinį audinį buvo įlietas grynos epoksidinės dervos ir 0,25 % masinės dalies ANV užpildo mišinys. Tam naudotas VARTM procesas. Kompozitai buvo palikti kambario temperatūroje 12 valandų, kad sukietėtų, o vėliau jie buvo apdoroti 80°C krosnyje 5 valandas.

3 metodo atveju 0,25% masinės dalies ANV buvo impregnuoti tiesiogiai statmenai pluoštui, naudojant aktyto nailono porėto nailono tūrinę medžiagą, kaip pavaizduota 1 pav. Pavyzdžiai, S₃.G₁ taikytas 101,3 kPa vakuuminis slėgis, o S₃.G₂ – 30,4 kPa slėgis. Kompozitai buvo apdorojami 12 valandų iki baigtinio kompozito vėlesnio apdoravimo 80°C krosnyje 5 valandas.

⁴ Šio skyriaus medžiaga anksčiau buvo publikuota [126]



5.1 pav. Modifikuoti VaRTM procesai: (a) sudarant susluoksniavimo sukrovimo seką, (b) proceso schema

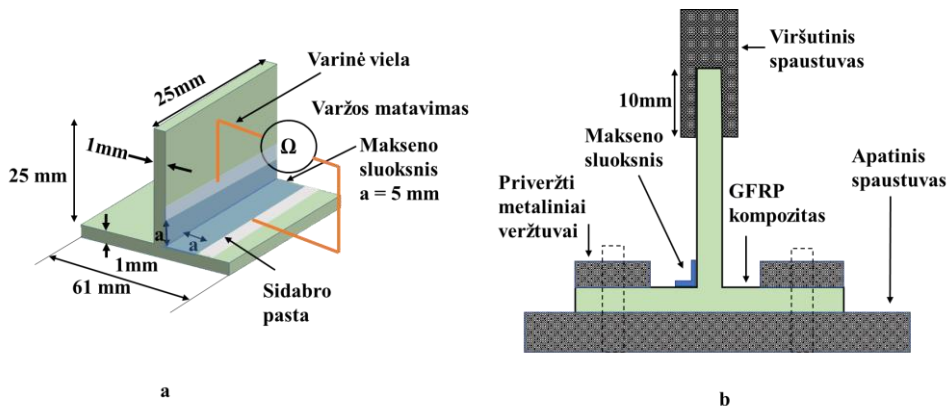
$S_1.G_1$, $S_1.G_2$, ir $S_3.G_1$ kompozitų pavydžių tempimo bandymai atitiko ISO 527-4 standartus. Testams buvo naudojama „Adamel DY36 UTM“ mašina, kurios skersinis greitis 2 mm/min. ANV tinklo elektros varža buvo nuolat stebima „Fluke 287 RMS“ multimetru. Kompozitinės medžiagos pavyzdžių $S_3.G_1$ ir $S_3.G_2$ lenkimo savybės buvo nustatytos taikant 3 taškų lenkimo testą pagal ISO-14125 standartus.

b) Trimačių austinių T profilio kompozitų su maksenu SSS⁵

$Ti_3C_2T_z$ maksenas buvo susintetintas iš Ti_3AlC_2 MAX fazės naudojant druskos rūgšties ir ličio fluorida mišinį. Gautas maksenas buvo išsluoksnuotas ir išgrynintas, taikant centrifugavimą ir plovimą. Taip paruoštas 3,3 mg/ml koncentracijos tirpalas, kuris buvo išpurkštas ant trimačių austinių T profilio kompozitų sandūros.

⁵ Šio skyriaus medžiaga anksčiau buvo publikuota [139]

Buvo išpjauti 5.2 pav. nurodytų matmenų penki T profilio kompozitų bandiniai. Jie buvo uždėti ant „Instron® ElectroPuls E10000T™“ mašinos. Elektros varžos pasikeitimas tempimo metu buvo išmatuotas dviejų zondų metodu, naudojant „Fluke 287 RMS“ multimetą. Tempimo testavimas atliktas 2 mm/min. greičiu, dinamometrinio daviklio galiai esant 10 kN. Statistinis koreliacijos koeficientas buvo apskaičiuotas siekiant nustatyti ryšį tarp taikomos galios ir makseno tinklo varžos.



5.2 pav. Trimačio austinio T profilio kompozito (a) bandinių matmenys, (b) eksperimentinis pasirengimas tempimo ir nuovargio apkrovai

Buvo tirta kompozitinės medžiagos nuovargio elgsena ciklinės apkrovos sąlygomis. 5.2a pav. rodomi penki bandiniai patikrinti dėl tempimo-tempimo nuovargio naudojant „Instron ElectroPuls E10000T™“ mašiną. Testai atlikti 6000 ciklų ir padalinti į 2000 ir 4000 ciklų grupes. Dažnis nustatytas ties 0,5 ir 1 Hz, o apkrova atitinkamai ties 50 N ir 100 N.

c) Daugiaašių kompozitų gamyba

Daugiaašiai kompozitai pagaminti 2 metodais, naudojant atviro skieto audimą (ASA) ir uždaro skieto audimą.

Buvo sukurti 5 modeliai. MAF kampas didintas. Jie buvo nuausti ASA mašina, kaip pagrindą naudojant paprastą audimą. 1200 tex stiklo pluošto „Hybon2002™“ iš Japonijos įmonės „NEG®“ buvo naudotas kaip metmenys, ataudai ir MAF. Gauto audinio sluoksnis buvo 600 GSM su 2,5 siūlų/cm apmatų ir ataudų tankiu. Išmatuotas atstumas tarp dviejų kaimyninių MAF buvo 2,5 cm. Daugiaašiai kompozitai pagaminti naudojant vakuuminį dervos infuzijos procesą. Taikyta RIMR 426 epoksidinės dervos sistema ir kietiklis RIMR 435 iš „Hexion Inc“. Sutvirtinta sluoksniuota medžiaga buvo laikoma 80°C krosnyje 8 valandas.

Tada tikrintas sluoksniuotų medžiagų tempimas pagal ISO 527-4 standartą naudojant „Zwick Roell®“ testavimo mašiną. Pavyzdžių matmenys: 250 mm x 25 mm. Modelio viduryje buvo išgręžta 5 mm (0° – 45° MAF atveju) ir 7–9 mm (0° MAF

atveju) skylė, kad galima būtų tirti armavimo poveikį pluoštui. Be to, sukurtas naujas audimo metodas, skirtas daugiaašiams audiniams austi uždaro skieto staklėmis.

d) Daugiaašio kompozito simuliacija

„Ansys“ darbastalyje buvo sukurtas FEM modelis, skirtas ASA angos kompozitų tempimo apkrovai ir daugiaašių anglies kompozitų smūginei apkrovai simuluoti.

Atliekant tempimo testą, medžiagos savybės, pateiktos 5.2 lentelėje, buvo apibrėžtos inžinerinių duomenų skyriuje. Sluoksniavimui projektuoti naudotas ACP modulis. Duomenys perduoti statinei struktūrinei analizei.

5.2 lentelė. Stiklo pluošto kompozitų medžiagos savybės

Savybė	Reikšmė
Tankis	1,85 g/cm ³
Jungo modulis X kryptimi E ₁	28085 MPa
Jungo modulis Y kryptimi E ₂	28085 MPa
Puasono koeficientas XY V ₁₂	0,159
Šlyties modulis XY G ₁₂	3610 MPa
Kompozito storis	2 mm

Norint simuluoti realų scenarijų, ribinėms sąlygoms priskirta geometrija buvo panaši į taikomas faktiniam pavyzdžiui. Poslinkis lygus 1 mm.

Norint simuluoti daugiaašio anglies kompozito smūgines savybes, bisfenolio epoksido F kaip matricos ir anglies pluošto kaip armavimo medžiagos savybės buvo taikomos 5.3 lentelėje pateiktos savybėms gauti. Simuliacija atlikta naudojant „Ansys“ tikslios dinamikos modulį, kur hemisferai buvo priskirtas 2,1 m/s greitis neigiama Z kryptimi, kad galima būtų imituoti lašo svorio poveikį.

5.3 lentelė. Anglies kompozitui sudarytos medžiagos savybės

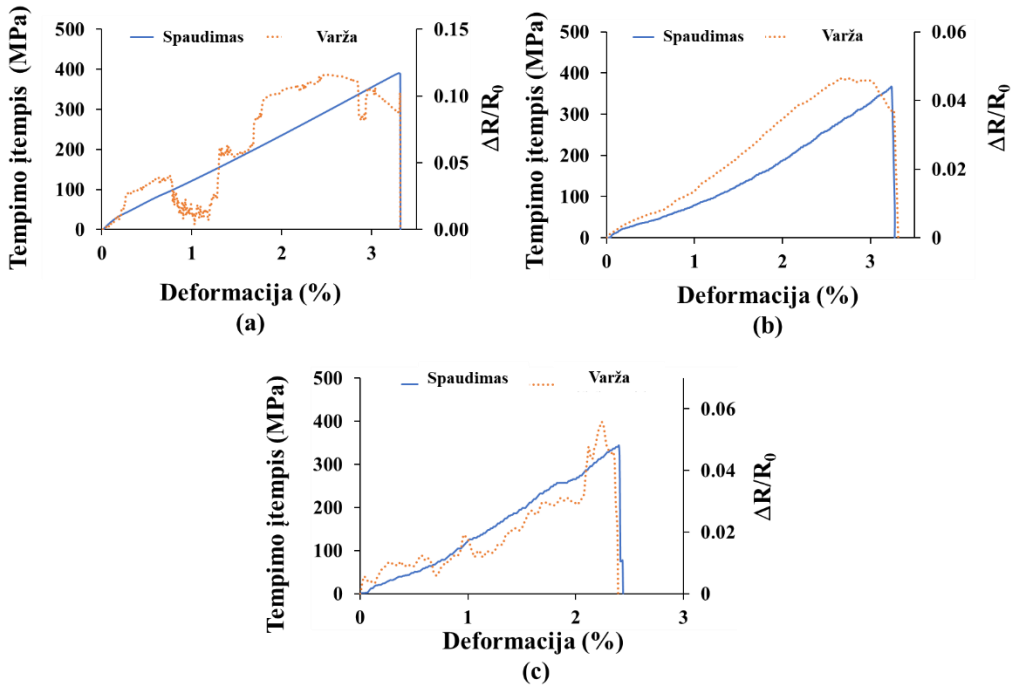
Parametrai	Reikšmės	Spaudimo ribos parametrai	Reikšmės	Įtempimo ribos parametrai	Reikšmės
Tankis	1420 kg/m ³	Tempimas X	805 MPa	Tempimas X	0,0126
Jungo modulis E ₁	61,34 GPa	Tempimas Y	805 MPa	Tempimas Y	0,0126
Jungo modulis E ₂	61,34 GPa	Tempimas Z	50 MPa	Tempimas Z	0,08
Jungo modulis E ₃	6,9 GPa	Suspaudimas X	509 MPa	Suspaudimas X	0,0102
Puasono koeficientas V ₂₃	0,3	Suspaudimas Y	509 MPa	Suspaudimas Y	0,0102
Puasono koeficientas V ₁₃	0,3	Suspaudimas Z	170 MPa	Suspaudimas Z	0,012
Šlyties modulis G ₁₂	3,3 GPa	Šlytis XY	125 MPa	Šlytis XY	0,022
Šlyties modulis G ₂₃	2,7 GPa	Šlytis YZ	65 MPa	Šlytis YZ	0,019
Šlyties modulis G ₁₃	2,7 GPa	Šlytis XZ	65 MPa	Šlytis XZ	0,019

Ribinės smūginės apkrovos sąlygos nustatytos taip, kad tinklo vidurinė žiedinė 40 mm skersmens dalis buvo palikta nesuvaržyta, o likęs tinklas pritvirtintas. Plokštė ir smūgiavimo tinklas buvo nustatyti trinties kontaktui ir naudotas 0,33 trinties koeficientas.

Rezultatai ir aptarimas

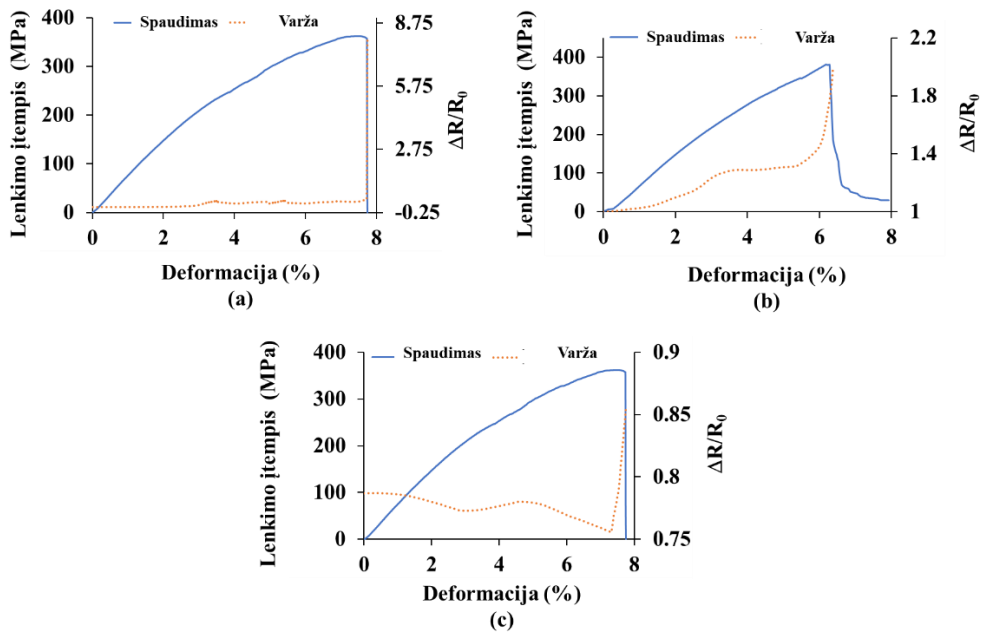
a) Trimačių austinių kompozitų su ANV SSS

Buvo analizuojami trys S₁.G₁, S₁.G₂, ir S₃.G₁ kompozitų pavyzdžiai. Varžos pokytis, normalizuotas iki pradinės varžos, buvo nustatytas santykinio pailgėjimo atžvilgiu, kaip parodyta 5.3 pav. Tyrimo metu nustatyta, kad S₁.G₁ ANV tinklas tapo netinkamas įtempimui žymėti dėl tęstinio tinklo pažeidimo. Priešingai, S₁.G₂ pasižymėjo varžos pokyčiu, atitinkančiu įtempimą, nenaudodamas kompozito pagrindo sunaikinimo energijos. S₃.G₁ pademonstravo ANV išilginimą su įtempimu ir nedidelį sunaikinimo energijos sugerimą.



5.3 pav. Realaus laiko pažeidimo aptikimas tempimo apkrovos metu a) $S_1.G_1$, b) $S_1.G_2$, c) $S_3.G_1$

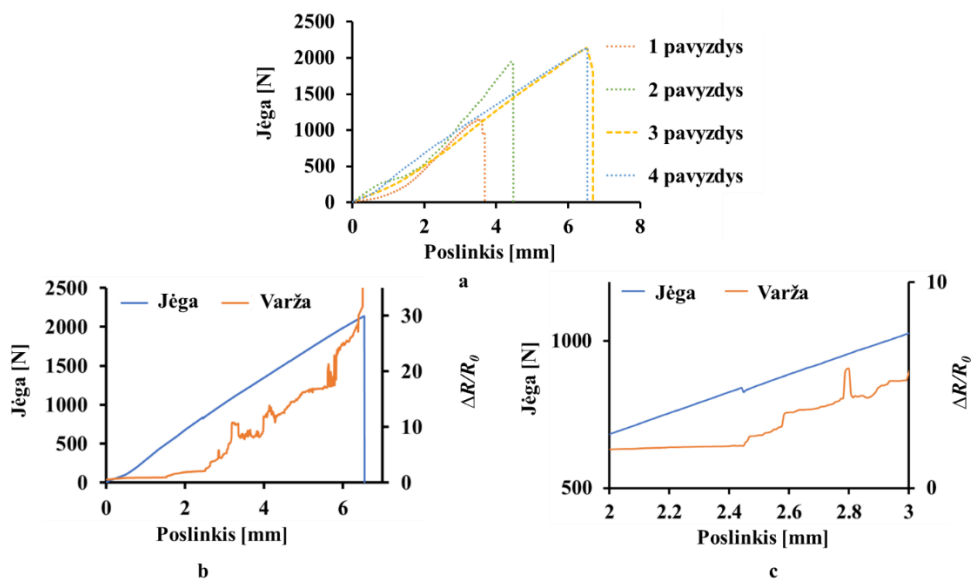
ANV tinklo pjezovaržos atsakas buvo sudarytas kaip $\Delta R/R_0$ pagal įtempimo reikšmes, pateiktas 5.4 pav. Rezultatai atskleidė, kad dalinai ANV įlieto tinklo lenkimo apkrovos žymėjimo veiksmingumas buvo didesnis nei pilnai įlietų tinklų atveju.



5.4 pav. Realaus laiko pažeidimo aptikimas lenkimo testavimo metu (a) $S_{3.G_1}$, (b) $S_{3.G_2}$ paviršiui taikant lenkimo įtempį, (c) $S_{3.G_2}$ paviršiui taikant sulenkimo įtempį

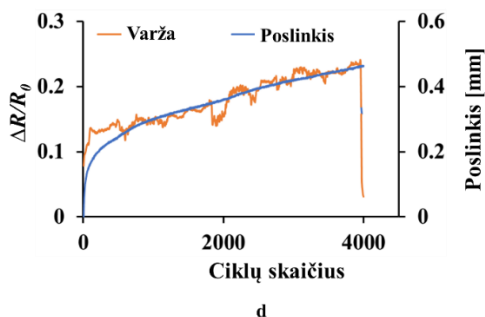
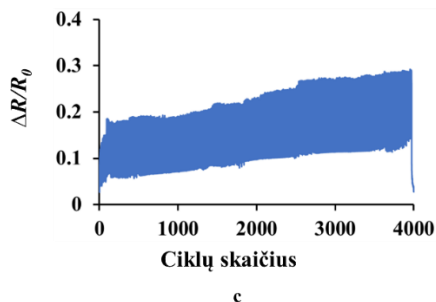
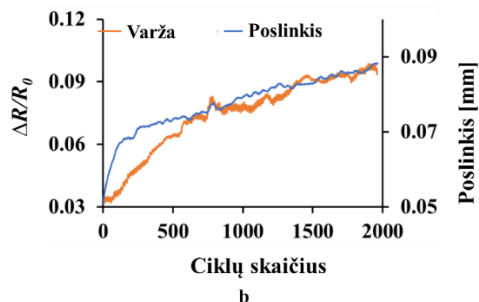
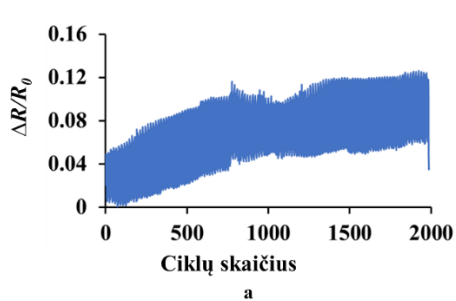
b) Trimačių austinių T profilio kompozitų su maksenu SSS

Buvo analizuojami keturių T profilio kompozitų pavyzdžių jėgos poslinkio grafikai. Juose matomos dvi skirtingos zonos: pradinis gedimas ir galinis gedimas, kur pradinis gedimas identifikuojamas kaip pirmasis tempimo apkrovos sumažėjimas, kaip parodyta 5.5 pav. Buvo apskaičiuotas kiekvieno pavyzdžio gaminio momento koreliacijos koeficientas jėgai ir varžos pokyčiui. Rezultatai atskleidė statistiškai monotoninę ryšį, kur koreliacijos koeficientas buvo nuo 0,68 iki 0,71.



5.5 pav. Realaus laiko T profilio kompozito deformacijos stebėjimas (a) T profilio kompozito tempimo testavimas, (b) makseno dangos pjezovaržos atsakas, (c) padidinta pradinio gedimo dalis

Ciklinės apkrovos sąlygomis buvo patikrinta ir T profilio kompozito, padengto maksenu, nuovargio elgsena. Tai parodyta 5.6 pav. Rezultatai leidžia teigti, kad makseno danga yra patikima medžiaga ciklinei apkrovai ir deformacijai aptikti. Be to, atskleistas aiškus ryšys tarp varžos reikšmių bei kompozito ciklinio įtempio ir deformacijos.

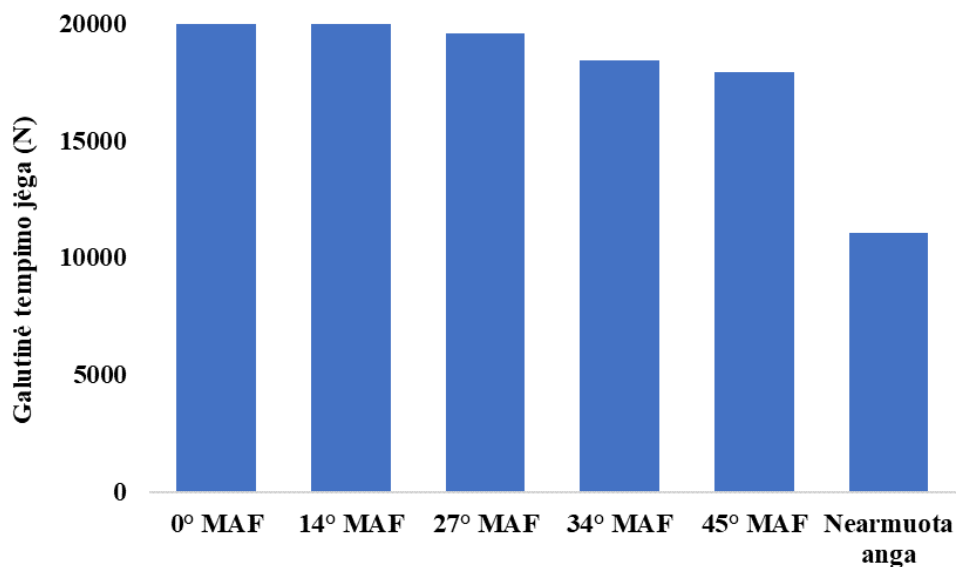


5.6 pav. Realaus laiko T profilio kompozito su makseno danga fiksavimas: (a) varžos matavimas esant 50 N–0,5 Hz, (b) poslinkio komponento fiksavimas 2000 ciklų nuovargio apkrovos metu, (c) varžos matavimas esant 100 N–1 Hz, (d) poslinkio komponento fiksavimas 4000 ciklų nuovargio apkrovos metu

c) Daugiaašio kompozito mechaninis charakterizavimas⁶

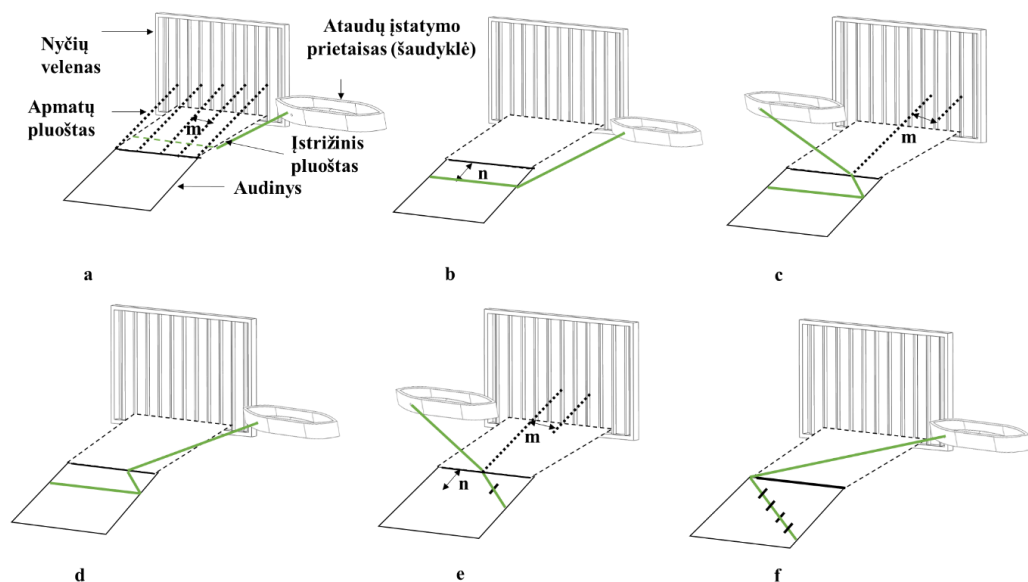
MAF modelių poveikis angos kompozito medžiagos armavimui rodo, kad galutinė tempimo jėga sumažėja, didėjant pluošto kampui. Tai rodo armavimo poveikio sumažėjimą padidinus MAF kampą, žr. 5.7 pav.

⁶ Šio skyriaus medžiaga anksčiau buvo publikuota [167]



5.7 pav. MAF modelių galutinės tempimo jėgos palyginimas

Įstrižinis pluoštas įdedamas atskirų šaudyklių veikimo metu. Jos turi daug pritvirtinimo taškų per audinio ilgį. Taip pasiekiamas reikalingas kampas. Daugiaašio audinio audimo šiuo metodu žingsniai pateikiami 5.8 pav.



5.8 pav. Daugiaašis audimas uždaro skieto staklėmis: a) įstrižinio pluošto pritvirtinimas prie pagrindo pluošto, b) audinio pagerinimas įtraukiant ataudus, c) įstrižinio

pluošto pritvirtinimas m atstumu nuo krašto, d) šaudyklės grįžimas į pradinį tašką, e) pritvirtinimo taško patraukimas į priekį, f) įstrižinio pluošto pritvirtinimo krypties pakeitimas

Kompozitų pavyzdžiai sudaryti rankinio sluoksniavimo metodu. Anglies pluošto armavimas buvo impregnuotas bisfenolio epoksidu F ir amino kietikliu ir paliktas 24 valandoms kambario temperatūroje, taikant vakuuminį slėgį. Vėliau kompozitai laikyti 80°C krosnyje 5 valandas. Pavyzdžio kodai ir kompozitų sukrovimo seka pateikiami 5.4 lentelėje.

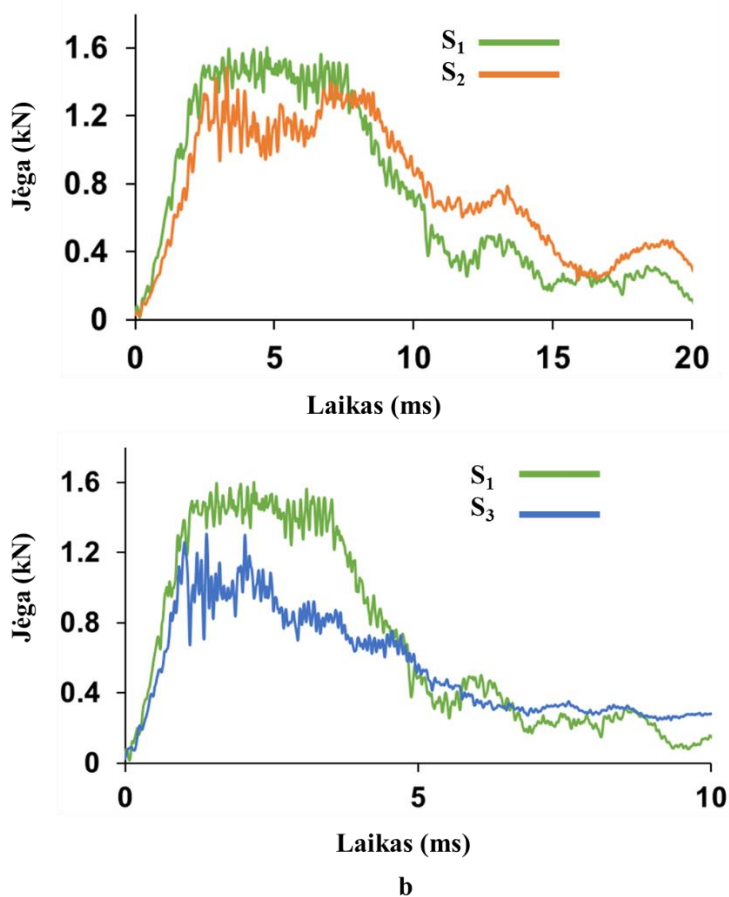
5.4 lentelė. Sukrovimo seka ir pavyzdžių kodai

Pavyzdžio kodas	Sukrovimo seka	Storis
S ₁	[0] ₄	0,85 mm
S ₂	[45/0/0/0]	0,85 mm
S ₃	[45/0/0/45]	0,85 mm
S ₄	[*0 ₄₅ /0/0/0]	0,85 mm
S ₅	[*0 ₄₅ /0/0/*0 ₄₅]	0,94 mm

* 0₄₅ – daugiaašiai pluoštai, integruoti į paprastą austinį audinį.

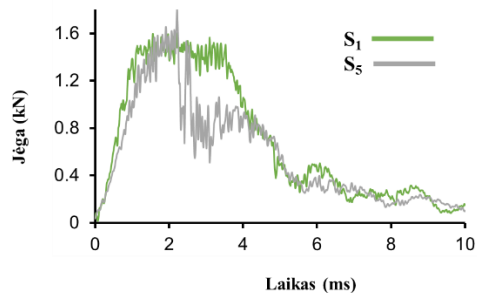
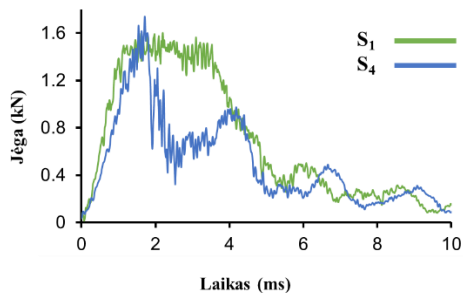
Smūgio testavimas atliktas naudojant „Coesfeld“ mažo greičio smūgio mašiną pagal ISO 6603-02 standartą. Kompozitų pavyzdžiai buvo supjaustyti 60 mm dydžio kvadratais ir pritvirtinti su vidinio 40 mm skersmens spaustuvu. 5,18 kg svorio ir 20 mm skersmens smūgiavimo prietaisas buvo numestas iš 0,4 m aukščio ant pavyzdžio. Bendra energija buvo lygi 20 J.

Sluoksniuotų medžiagų kryžminio ir kampinio sluoksnių jėgos ir laiko kreivės smūginės apkrovos atveju atskleidė, kad kampinio sluoksnių sluoksnių medžiaga (S₂) pasižymėjo mažesne kontaktine jėga nei kryžminio sluoksnių sluoksnių medžiaga (S₁), žr. 5.9 pav., a.



5.9 pav. a) S₁ su S₂, b) S₁ su S₃ jėgos ir laiko istorijos palyginimas

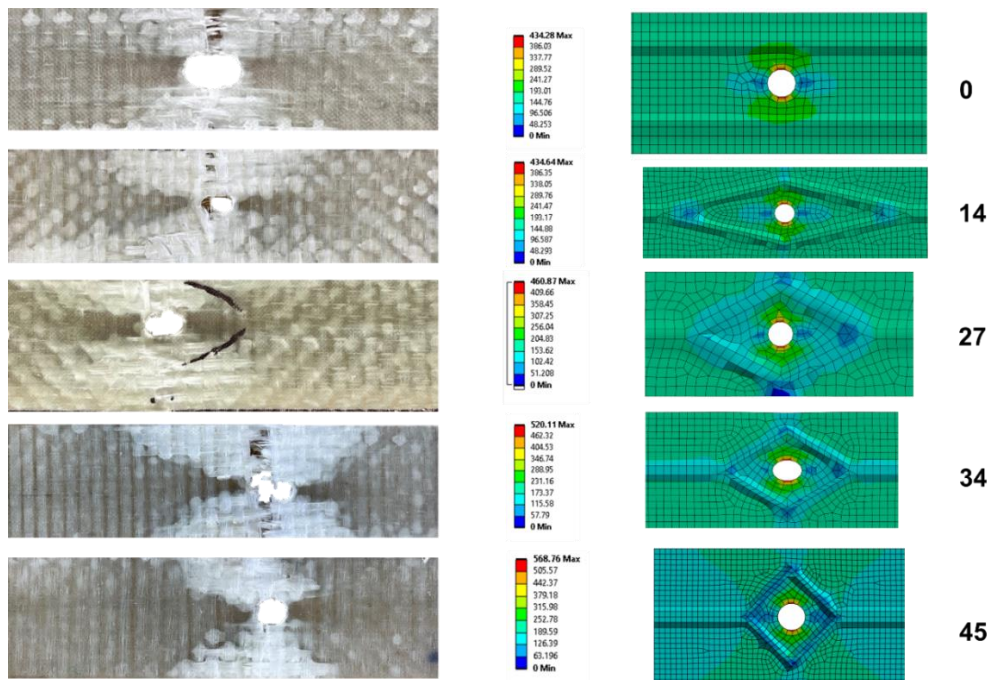
Norint panaikinti sluoksnių skirtingumus, įstrižiniai pluoštai buvo išausti ant paprasto austinio pagrindo. 5.10 pav. rodomos S₄ ir S₅ jėgos ir laiko kreivės lyginamos S₁. Atskleista, kad skirtingumas tarp kompozitinės medžiagos sluoksnių buvo sumažintas, dėl ko padidėjo didžiausia apkrova kontaktinės jėgos taške. Be to, pridėjus antrą daugiaašį sluoksnį į S₅, dar labiau padidėjo kryžminio pluošto armavimo poveikis, žr. 5.10 pav., b.



5.10 pav. a) S_1 su S_4 , b) S_1 su S_5 jėgos ir laiko istorijos palyginimas

d) Daugiaašio kompozito simuliacija

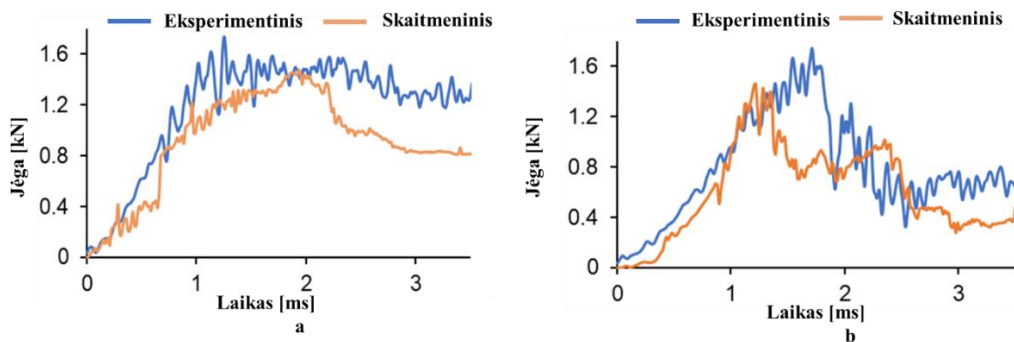
ASA kompozitų tempimo testavimo statinės konstrukcinės analizės rezultatai pateikiami 5.11 pav. Jie rodo, kad, MAF kampui nutolus nuo apmatų, spaudimas pradeda kauptis prie skylės.



5.11 pav. Daugiaašio kompozito tempimo testavimo eksperimentiniai ir simuliacijos rezultatai

Šiame skyriuje aptariamas skaitmeniniam kompozitinių medžiagų modeliavimui naudojamas Hašino kriterijus lašo svorio smūginės apkrovos testavimo metu. Simuliacijos rezultatai palyginti su eksperimentiniais duomenimis ir pateikiami 5.12 pav. Simuliacijos modeliu pavyko tiksliai nustatyti kompozitų pavyzdžių jėgos ir

laiko istoriją tiek elastinio, tiek nelinijinio plastiko srityse. Tarp eksperimentinių ir simuliacijos rezultatų pastebėtas tik nedidelis neatitikimas, kurį galima paaiškinti testavimo ir mašinos vibravimo klaidomis.



5.12 pav. a) paprasto austinio audinio ir b) daugiaašių kompozitų smūginės apkrovos eksperimentinių ir skaitmeninių rezultatų palyginimas

Išvados

Tyrimo rezultatai leidžia padaryti šias išvadas:

1. Sveikatos stebėsenai buvo sukurti stiklo pluošto stačiakampiai trimačiai austiniai kompozitai su anglies nanovamzdeliais. Taikant anglies nanovamzdelių perdavimo metodą iš porėtos aplinkos į audinio išankstinę formą, taikant vakuuminį slėgį, anglies nanovamzdeliai gaunamuose kompozituose pasiskirsto vienodai. 101,3 kPa vakuuminis slėgis padeda įleisti anglies nanovamzdelį pro audinio storį, o 30,3 kPa slėgis leidžia iš dalies įleisti anglies nanovamzdelius.
2. Buvo sukurti stiklo pluošto trimačiai austiniai T profilio kompozitai su makseno nanodalelėmis. Naudojant 10 sluoksnių 3,3 mg/ml koncentracijos makseno su vandeniu mišinį padengimui, sėkmingai sukuriama laidus $10^5 \Omega$ sluoksnis.
3. Daugiaašiai kompozitai suprojektuoti ir sukurti taikant atviro ir uždaro skieto audimo metodą. „Dornier“ atviro skieto audimo staklės naudotos penkių skirtingų modelių 1200 tex stiklo pluoštui austi, siekiant armuoti 5 mm skylę. Daugiaašio pluošto kampas buvo progresyviai didinamas nuo 0° iki 45° , dirbant su 5 modeliais. Antrasis metodas leido sukurti naują būdą, kaip austi daugiaašes formas naudojant 200 tex anglies pluoštą uždaro skieto audimo staklėmis. Šis metodas padėjo sėkmingai pagaminti daugiaašes 45° kampo anglies daugiaašių pluoštų formas, neatliekant sudėtingų esamo audimo mechanizmo pakeitimų.
4. Per storį įlietas anglies nanovamzdelių sluoksnis leido aptikti tempimo apkrovos sąlygų pažeidimus ir deformacijas, keičiant varžos reikšmes pagal stačiakampiam trimačiui austiniam kompozitui taikomą įtempimą. Taip pat dalinai įlietas anglies

nanovamzdelių sluoksnis leido aptikti stiklo pluošto stačiakampio trimačio austinio kompozito lenkimo apkrovos sąlygų pažeidimus ir deformacijas. Maksimalus padengtas stiklo pluošto trimatis austinis T profilio kompozitas gebėjo aptikti poslinkį ir pažeidimus, kai įtempimo apkrova buvo iki 2140 N, o 6000 ciklų nuovargio apkrova esant 0,5 Hz buvo 50 N ir 1 Hz esant 100 N. Testuojant ASA daugiaašių kompozitų įtempimą paaiškėjo, kad 0° daugiaašio pluošto modelis suteikė didžiausią armavimą, padidindamas galinę įtempimo jėgą 44 %, o daugiaašis pluoštas nukreipė spaudimo kaupimąsi iš skylės pakrovimo ašies link. Nustatyta, kad uždaro skieto metodu pagaminti daugiaašiai kompozitai sustiprino anglies pluošto kompozitus 6 % smūginės apkrovos sąlygomis.

5. Buvo sukurtas simuliacinis modelis, skirtas daugiaašių kompozitų mechaninėms savybėms įvertinti. Taikant stiklo pluošto atviro skieto būdu austų kompozitų tempimo testavimo statinę struktūrinę analizę, išanalizuoti baigtiniai elementai. Anglies pluošto kompozitų smūginei apkrovai taikyta tiksli dinaminė simuliacija. Spaudimas prie angos atviro skieto būdu austų kompozitų skylėje didėjo daugiaašio pluošto kampui nukrypstant nuo apmatų, o tai atitinka eksperimentinius rezultatus. Daugiaašių anglies pluošto kompozitų, gautų naudojant uždara skietą, smūginės apkrovos simuliacijos rezultatai iš esmės atitiko eksperimentinius duomenis. Neatitikimas buvo lygus 3 % paprasto austinio kompozito atveju ir 5 % – daugiaašio austinio kompozito atveju.

REFERENCES

1. SUN, Shengwei, HAN, Baoguo, JIANG, Shan, YU, Xun, WANG, Yanlei, LI, Hongyan and OU, Jinping. Nano graphite platelets-enabled piezoresistive cementitious composites for structural health monitoring. *Construction and Building Materials*. 2017. DOI 10.1016/j.conbuildmat.2017.01.006.
2. KANG, Inpil, SCHULZ, Mark J., LEE, Jong Won, CHOI, Gyeong Rak, JUNG, Joo Young, CHOI, Jae Boong, HWANG, Sung Ho, KANG, In Pil, SCHULZ, Mark J., LEE, Jong Won, CHOI, Gyeong Rak, JUNG, Joo Young, CHOI, Jae Boong and HWANG, Sung Ho. A carbon nanotube smart material for structural health monitoring. In : *Solid State Phenomena*. 2007. ISBN 3908451299. DOI 10.4028/www.scientific.net/SSP.120.289.
3. SODANO, Henry A., PARK, Gyuhae and INMAN, Daniel J. An investigation into the performance of macro-fiber composites for sensing and structural vibration applications. *Mechanical Systems and Signal Processing*. 2004. DOI 10.1016/S0888-3270(03)00081-5.
4. TULOUP, C., HARIZI, W., ABOURA, Z., MEYER, Y., KHELLIL, K. and LACHAT, R. On the use of in-situ piezoelectric sensors for the manufacturing and structural health monitoring of polymer-matrix composites: A literature review. *Composite Structures*. 2019. Vol. 215, p. 127–149. DOI 10.1016/j.compstruct.2019.02.046.
5. TANG, Hong Yue, WINKELMANN, Charles, LESTARI, Wahyu and LA SAPONARA, Valeria. Composite structural health monitoring through use of embedded PZT sensors. *Journal of Intelligent Material Systems and Structures*. 2011. Vol. 22, no. 8, p. 739–755. DOI 10.1177/1045389X11406303.
6. CAI, Jian, QIU, Lei, YUAN, Shenfang, SHI, Lihua, LIU, PeiPei and LIANG, Dong. Structural Health Monitoring for Composite Materials. In : *Composites and Their Applications*. Online. InTech, 2012.
7. KANG, In Pil, SCHULZ, Mark J., LEE, Jong Won, CHOI, Gyeong Rak, JUNG, Joo Young, CHOI, Jae Boong and HWANG, Sung Ho. A carbon nanotube smart material for structural health monitoring. In : *Solid State Phenomena*. 2007. ISBN 9783908451297. DOI 10.4028/www.scientific.net/SSP.120.289.
8. BALAJI, R. and SASIKUMAR, M. Structural Health Monitoring (SHM) System for Polymer Composites: A Review. *Indian Journal of Science and Technology*. Online. 8 November 2016. Vol. 9, no. 41. DOI 10.17485/ijst/2016/v9i41/85832.
9. LEE, Gil-Yong, KIM, Min-Soo, YOON, Hae-Sung, YANG, Jinkyu, IHN, Jeong-Beom and AHN, Sung-Hoon. Direct Printing of Strain Sensors via Nanoparticle Printer for the Applications to Composite Structural Health Monitoring. *Procedia CIRP*. Online. 2017. Vol. 66, p. 238–242. DOI 10.1016/j.procir.2017.03.279.
10. ALEXOPOULOS, N. D., BARTHOLOME, C., POULIN, P. and MARIOLI-RIGA, Z. Structural health monitoring of glass fiber reinforced composites using embedded carbon nanotube (CNT) fibers. *Composites Science and Technology*. 2010. Vol. 70, no. 2, p. 260–271. DOI 10.1016/j.compscitech.2009.10.017.
11. GIURGIUTIU, V. Structural health monitoring (SHM) of aerospace composites. In : *Polymer Composites in the Aerospace Industry*. Online. Elsevier, 2015. p. 449–507. ISBN 9780857099181.
12. GIURGIUTIU, Victor. 7.19 Smart Materials and Health Monitoring of Composites. In : *Comprehensive Composite Materials II*. Online. Elsevier, 2018. p. 364–381. ISBN 9780081005330.

13. GASCO, Federico, FERABOLI, Paolo, BRAUN, Jeff, SMITH, Joshua, STICKLER, Patrick and DEOTO, Luciano. Wireless strain measurement for structural testing and health monitoring of carbon fiber composites. *Composites Part A: Applied Science and Manufacturing*. 2011. DOI 10.1016/j.compositesa.2011.05.008.
14. ZHANG, Han, BILOTTI, Emiliano and PEIJS, Ton. The use of carbon nanotubes for damage sensing and structural health monitoring in laminated composites: a review. *Nanocomposites*. Online. 2 October 2015. Vol. 1, no. 4, p. 167–184. DOI 10.1080/20550324.2015.1113639.
15. ALOKITA, Shukla, RAHUL, Verma, JAYAKRISHNA, Kandasamy, KAR, V.R., RAJESH, M., THIRUMALINI, S. and MANIKANDAN, M. Recent advances and trends in structural health monitoring. In : *Structural Health Monitoring of Biocomposites, Fibre-Reinforced Composites and Hybrid Composites*. Online. Elsevier, 2019. p. 53–73. ISBN 9780081022917.
16. SEBASTIAN, J., SCHEHL, N., BOUCHARD, M., BOEHLE, M., LI, L., LAGOUNOV, A. and LAFDI, K. Health monitoring of structural composites with embedded carbon nanotube coated glass fiber sensors. *Carbon*. Online. January 2014. Vol. 66, p. 191–200. DOI 10.1016/j.carbon.2013.08.058.
17. LAU, K. T. Structural health monitoring for smart composites using embedded FBG sensor technology. *Materials Science and Technology (United Kingdom)*. 2014. Vol. 30, no. 13, p. 1642–1654. DOI 10.1179/1743284714Y.0000000608.
18. FIEDLER, Bodo and SCHULTE, Karl. 6.8 Carbon Nanotube-Based Composites. In : *Comprehensive Composite Materials II*. Online. Elsevier, 2018. p. 201–229. ISBN 9780081005330.
19. ANAS, Muhammad, NASIR, Muhammad Ali, ASFAR, Zeeshan, NAUMAN, Saad, AKALIN, Mehmet and AHMAD, Faiz. Structural health monitoring of GFRP laminates using graphene-based smart strain gauges. *Journal of the Brazilian Society of Mechanical Sciences and Engineering*. Online. 2018. Vol. 40, no. 8, p. 1–10. DOI 10.1007/s40430-018-1320-4.
20. KANG, Inpil, HEUNG, Yun Yeo, KIM, Jay H., LEE, Jong Won, GOLLAPUDI, Ramanand, SUBRAMANIAM, Srinivas, NARASIMHADEVARA, Suhasini, HURD, Douglas, KIRIKERA, Goutham R., SHANOV, Vesselin, SCHULZ, Mark J., SHI, Donglu, BOERIO, Jim, MALL, Shankar and RUGGLES-WREN, Marina. Introduction to carbon nanotube and nanofiber smart materials. *Composites Part B: Engineering*. 2006. DOI 10.1016/j.compositesb.2006.02.011.
21. CHUNG, D. D.L. *Structural health monitoring by electrical resistance measurement*. 2001.
22. GIURGIUTIU, Victor. Impact and Acoustic Emission Monitoring for Aerospace Composites SHM. In : *Structural Health Monitoring of Aerospace Composites*. Online. Elsevier, 2016. p. 317–394.
23. LIN, Xiu-juan, ZHOU, Ke-chao, ZHANG, Xiao-yong and ZHANG, Dou. Development, modeling and application of piezoelectric fiber composites. *Transactions of Nonferrous Metals Society of China*. Online. January 2013. Vol. 23, no. 1, p. 98–107. DOI 10.1016/S1003-6326(13)62435-8.
24. MALESKI, Kathleen, MOCHALIN, Vadym N. and GOGOTSI, Yury. Dispersions of Two-Dimensional Titanium Carbide MXene in Organic Solvents. *Chemistry of Materials*. Online. 28 February 2017. Vol. 29, no. 4, p. 1632–1640. DOI 10.1021/acs.chemmater.6b04830.
25. LI, Bohan, MA, Keming, LU, Shaowei, LIU, Xingmin, MA, Ziang, ZHANG, Lu, WANG, Xiaoqiang and WANG, Sai. Structural health monitoring for polymer

- composites with surface printed MXene/ink sensitive sensors. *Applied Physics A: Materials Science and Processing*. Online. 2020. Vol. 126, no. 10, p. 1–11. DOI 10.1007/s00339-020-03979-4.
26. MONASTYRECKIS, Gediminas, STEPURA, Anastasiia, SOYKA, Yaryna, MALTANAVA, Hanna, POZNYAK, Sergey K., OMASTOVÁ, Mária, ANISKEVICH, Andrey and ZELENIAKIENE, Daiva. Strain Sensing Coatings for Large Composite Structures Based on 2D MXene Nanoparticles. *Sensors*. Online. 29 March 2021. Vol. 21, no. 7, p. 2378. DOI 10.3390/s21072378.
 27. JOLLY, Mr, PRABHAKAR, A., STURZU, B., HOLLSTEIN, K., SINGH, R., THOMAS, S., FOOTE, P. and SHAW, A. Review of Non-destructive Testing (NDT) Techniques and their Applicability to Thick Walled Composites. *Procedia CIRP*. Online. 2015. Vol. 38, p. 129–136. DOI 10.1016/j.procir.2015.07.043.
 28. HONG NG, Vincent Ming, HUANG, Hui, ZHOU, Kun, LEE, Pooi See, QUE, Wenxiu, XU, Jason Zhichuan and KONG, Ling Bing. Recent progress in layered transition metal carbides and/or nitrides (MXenes) and their composites: synthesis and applications. *Journal of Materials Chemistry A*. Online. 2017. Vol. 5, no. 7, p. 3039–3068. DOI 10.1039/C6TA06772G.
 29. ZUKIENE, K., MONASTYRECKIS, G., KILIKEVICIUS, S., PROCHÁZKA, M., MICUSIK, M., OMASTOVÁ, M., ANISKEVICH, A. and ZELENIAKIENE, D. Wettability of MXene and its interfacial adhesion with epoxy resin. *Materials Chemistry and Physics*. Online. January 2021. Vol. 257, p. 123820. DOI 10.1016/j.matchemphys.2020.123820.
 30. SHI, Yongqian, LIU, Chuan, LIU, Lu, FU, Libu, YU, Bin, LV, Yuancai, YANG, Fuqiang and SONG, Pingan. Strengthening, toughening and thermally stable ultra-thin MXene nanosheets/polypropylene nanocomposites via nanoconfinement. *Chemical Engineering Journal*. Online. December 2019. Vol. 378, p. 122267. DOI 10.1016/j.cej.2019.122267.
 31. ZHANG, Jizhen, KONG, Na, UZUN, Simge, LEVITT, Ariana, SEYEDIN, Shayan, LYNCH, Peter A., QIN, Si, HAN, Meikang, YANG, Wenrong, LIU, Jingquan, WANG, Xungai, GOGOTSI, Yury and RAZAL, Joselito M. Scalable Manufacturing of Free-Standing, Strong Ti₃C₂T_x MXene Films with Outstanding Conductivity. *Advanced Materials*. Online. 20 June 2020. Vol. 32, no. 23, p. 2001093. DOI 10.1002/adma.202001093.
 32. PLUMMER, Gabriel, ANASORI, Babak, GOGOTSI, Yury and TUCKER, Garritt J. Nanoindentation of monolayer Ti₃C₂MXenes via atomistic simulations: The role of composition and defects on strength. *Computational Materials Science*. Online. February 2019. Vol. 157, p. 168–174. DOI 10.1016/j.commatsci.2018.10.033.
 33. FORCELLESE, Archimede, SIMONCINI, Michela, VITA, Alessio, GIOVANNELLI, Andrea and LEONARDI, Linda. Performance analysis of MWCNT/Epoxy composites produced by CRTM. *Journal of Materials Processing Technology*. Online. December 2020. Vol. 286, p. 116839. DOI 10.1016/j.jmatprotec.2020.116839.
 34. NAUMAN, Saad, CRISTIAN, Irina and KONCAR, Vladan. Intelligent carbon fibre composite based on 3D-interlock woven reinforcement. *Textile Research Journal*. 2012. Vol. 82, no. 9, p. 931–944. DOI 10.1177/0040517512436831.
 35. MOUNTASIR, A., HOFFMANN, G., CHERIF, Ch, LÖSER, M. and GROSSMANN, K. Competitive manufacturing of 3D thermoplastic composite panels based on multi-layered woven structures for lightweight engineering. *Composite Structures*. Online. December 2015. Vol. 133, p. 415–424. DOI 10.1016/j.compstruct.2015.07.071.

36. BILISIK, Kadir. Multiaxis three-dimensional weaving for composites: A review. *Textile Research Journal*. Online. 1 May 2012. Vol. 82, no. 7, p. 725–743. DOI 10.1177/00405175111435013.
37. UMER, R., ALHUSSEIN, H., ZHOU, J. and CANTWELL, WJ. The mechanical properties of 3D woven composites. *Journal of Composite Materials*. Online. 30 May 2017. Vol. 51, no. 12, p. 1703–1716. DOI 10.1177/0021998316681187.
38. BILISIK, Kadir. Multiaxis 3D Woven Preform and Properties of Multiaxis 3D Woven and 3D Orthogonal Woven Carbon/Epoxy Composites. *Journal of Reinforced Plastics and Composites*. Online. 27 April 2010. Vol. 29, no. 8, p. 1173–1186. DOI 10.1177/0731684409103153.
39. KHOKAR, N. 3D Fabric-forming Processes: Distinguishing Between 2D-weaving, 3D-weaving and an Unspecified Non-interlacing Process. *Journal of the Textile Institute*. Online. January 1996. Vol. 87, no. 1, p. 97–106. DOI 10.1080/00405009608659059.
40. TURGUT, Firat, KOYCU, Arda, NEJE, Ghanshyam, BEHERA, Bijoy, OZDEN YENIGUN, Elif and CEBECI, Hulya. Hierarchical CNTs Grown Multifunctional 3D Woven Composite Beams for Aerospace Applications. In : *AIAA Scitech 2020 Forum*. Online. Reston, Virginia : American Institute of Aeronautics and Astronautics, 6 January 2020. ISBN 978-1-62410-595-1. DOI 10.2514/6.2020-0153.
41. HUFENBACH, W., BÖHM, R., THIEME, M., WINKLER, A., MÄDER, E., RAUSCH, J. and SCHADE, M. Polypropylene/glass fibre 3D-textile reinforced composites for automotive applications. *Materials & Design*. Online. March 2011. Vol. 32, no. 3, p. 1468–1476. DOI 10.1016/j.matdes.2010.08.049.
42. MISHRA, Ashish and NAIK, N. K. Failure initiation in composite structures under low-velocity impact: Analytical studies. *Composite Structures*. 1 January 2010. Vol. 92, no. 2, p. 436–444. DOI 10.1016/J.COMPSTRUCT.2009.08.024.
43. MOOD, GI. Multiaxial yarn structure and weaving method. US Patent 5540260. 1996.
44. AHMAD, Furqan, HONG, Jung Wuk, CHOI, Heung Soap, PARK, Soo Jin and PARK, Myung Kyun. The effects of stacking sequence on the penetration-resistant behaviors of T800 carbon fiber composite plates under low-velocity impact loading. *Carbon Letters*. 2015. Vol. 16, no. 2, p. 107–115. DOI 10.5714/CL.2015.16.2.107.
45. OH, Hyun-Taik, WON, Jong-Ick, WOO, Sung-Choong and KIM, Tae-Won. Determination of Impact Damage in CFRP via PVDF Signal Analysis with Support Vector Machine. *Materials*. Online. 18 November 2020. Vol. 13, no. 22, p. 5207. DOI 10.3390/ma13225207.
46. OGIN, S.L., BRØNDSTED, P. and ZANGENBERG, J. Composite materials. In : *Modeling Damage, Fatigue and Failure of Composite Materials*. Online. Elsevier, 2016. p. 3–23.
47. LABANIEH, Ahmad Rashed, LEGRAND, Xavier, KONCAR, Vladan and SOULAT, Damien. Development in the multiaxis 3D weaving technology. *Textile Research Journal*. 2016. Vol. 86, no. 17, p. 1869–1884. DOI 10.1177/0040517515612365.
48. BRUYERE, Alain, DEBAILLE, Christian and FRANCK, Perret. Bias-bound fabric method for making same and weaving machine for continuously making such a fabric. US6494235B1. 2002.
49. WANG, Xinmiao, CHEN, Li, WANG, Junshan, LI, Xintao and ZHANG, Zhongwei. A novel multiaxial three-dimensional woven preform: Process and structure. *Journal of Reinforced Plastics and Composites*. Online. 1 February 2018. Vol. 37, no. 4, p. 247–266. [Accessed 22 April 2023]. DOI 10.1177/0731684417741204/ASSET/IMAGES/LARGE/10.1177_07316844177

- 41204-FIG18.JPEG.
50. SCHMANSKI, Donald. Woven material with filling threads at angle other than right angle. US4055697A. 1977.
 51. HASHIM, Mohd Khairul Rabani, ABDUL MAJID, Mohd Shukry, MOHD JAMIR, Mohd Ridzuan, KASIM, Farizul Hafiz, ALSHAHRANI, Hassan A., DEROS, Mohd Azaman Md and HUI, David. Effects of Ply Orientations and Stacking Sequences on Impact Response of Pineapple Leaf Fibre (PALF)/Carbon Hybrid Laminate Composites. *Materials*. 2022. Vol. 15, no. 17. DOI 10.3390/ma15176121.
 52. DRZAL, L. T. and MADHUKAR, M. Fibre-matrix adhesion and its relationship to composite mechanical properties. *Journal of Materials Science*. Online. 1993. Vol. 28, no. 3, p. 569–610. DOI 10.1007/BF01151234.
 53. RAZALI, N., SULTAN, M.T.H., MUSTAPHA, F., YIDRIS, N. and ISHAK, M.R. Impact Damage on Composite Structures – A Review. *The International Journal Of Engineering And Science*. 2014. Vol. 3, no. 7, p. 8–20.
 54. BRYN, L., ISLAM, M. and W, Lowery. Three-dimensional woven forms with integral bias fibers and bias weaving loom. US Patent 6742547. 2004. USA : USA patent.
 55. ANDREW, J. Jefferson, SRINIVASAN, Sivakumar M., AROCKIARAJAN, A. and DHAKAL, Hom Nath. Parameters influencing the impact response of fiber-reinforced polymer matrix composite materials: A critical review. *Composite Structures*. 2019. Vol. 224, no. May. DOI 10.1016/j.compstruct.2019.111007.
 56. GIASIN, Khaled and AYVAR-SOBERANIS, Sabino. Microstructural investigation of drilling induced damage in fibre metal laminates constituents. *Composites Part A: Applied Science and Manufacturing*. Online. June 2017. Vol. 97, p. 166–178. DOI 10.1016/j.compositesa.2017.02.024.
 57. SOLIMAN, Eslam M., SHEYKA, Michael P. and TAHA, Mahmoud Reda. Low-velocity impact of thin woven carbon fabric composites incorporating multi-walled carbon nanotubes. *International Journal of Impact Engineering*. Online. 2012. Vol. 47, p. 39–47. DOI 10.1016/j.ijimpeng.2012.03.002.
 58. ANAHARA, Meiji, YASUI, Yoshiharu, HIROSHI, Omori, OMORI, H and YASUI, Yoshiharu. Three dimensional fabric and method for producing the same. Online. US Patent 5137058. 11 August 1992. USA : US Patent 5, 137, 058. Available from: <http://www.google.com/patents/US5137058>
 59. SIKARWAR, Rahul S. and VELMURUGAN, R. Impact damage assessment of carbon fiber reinforced composite with different stacking sequence. *Journal of Composite Materials*. 2020. Vol. 54, no. 2, p. 193–203. DOI 10.1177/0021998319859934.
 60. LIMA, Mário, FANGUEIRO, Raul, ROSIEPEN, Christien and ROCHA, Válter. Multiweave-A prototype weaving machine for multiaxial technical fabrics. *Indian Journal of Fibre & Textile Research*. 2009. Vol. 34, p. 59–63.
 61. RUZAND, Jean-Marc. Multiaxial three dimensional fabric and process for its manufacture. WO 94/20658. 1994.
 62. HONGKARNJANAKUL, N., BOUVET, C. and RIVALLANT, S. Validation of low velocity impact modelling on different stacking sequences of CFRP laminates and influence of fibre failure. *Composite Structures*. Online. 2013. Vol. 106, p. 549–559. DOI 10.1016/j.compstruct.2013.07.008.
 63. BADAWY, Amal A.M. Impact behavior of glass fibers reinforced composite laminates at different temperatures. *Ain Shams Engineering Journal*. 1 June 2012. Vol. 3, no. 2, p. 105–111. DOI 10.1016/J.ASEJ.2012.01.001.
 64. AO, Wenhong, ZHUANG, Weimin, XING, Bobin, ZHOU, Qing and XIA, Yong.

- Finite element method of a progressive intralaminar and interlaminar damage model for woven fibre laminated composites under low velocity impact. *Materials and Design*. Online. 2022. Vol. 223, p. 111256. DOI 10.1016/j.matdes.2022.111256.
65. UCHIDA, H, YAMAMOTO, T and TAKASHIMA, H. Three dimensional weaving machine. US Patent 6003563. 1999.
 66. CAMINERO, M. A., GARCÍA-MORENO, I. and RODRÍGUEZ, G. P. Experimental study of the influence of thickness and ply-stacking sequence on the compression after impact strength of carbon fibre reinforced epoxy laminates. *Polymer Testing*. Online. 2018. Vol. 66, no. February, p. 360–370. DOI 10.1016/j.polymertesting.2018.02.009.
 67. HER, Shiuh Chuan and LIANG, Yu Cheng. The finite element analysis of composite laminates and shell structures subjected to low velocity impact. *Composite Structures*. 1 October 2004. Vol. 66, no. 1–4, p. 277–285. DOI 10.1016/j.compstruct.2004.04.049.
 68. BØRVIK, T., HOPPERSTAD, O.S., BERSTAD, T. and LANGSETH, M. Perforation of 12mm thick steel plates by 20mm diameter projectiles with flat, hemispherical and conical noses. *International Journal of Impact Engineering*. Online. January 2002. Vol. 27, no. 1, p. 37–64. DOI 10.1016/S0734-743X(01)00035-5.
 69. GUO, Qiwei, ZHANG, Yifan, LI, Diansen, GUO, Ruiqing, MA, Ming and CHEN, Li. Effect of bias yarn on tensile fracture mechanism of multiaxial 3D angle-interlock woven composites. *Thin-Walled Structures*. 1 February 2021. Vol. 159, p. 107269. DOI 10.1016/J.TWS.2020.107269.
 70. BILISIK, A. Kadir. New method of weaving multiaxis three dimensional flat woven fabric: Feasibility of prototype tube carrier weaving. *Fibres and Textiles in Eastern Europe*. 2009. Vol. 77, no. 6.
 71. ATAS, Cesim and LIU, Dahsin. Impact response of woven composites with small weaving angles. *International Journal of Impact Engineering*. 2008. Vol. 35, no. 2, p. 80–97. DOI 10.1016/j.ijimpeng.2006.12.004.
 72. NAYFEH, S., ROHRS, J. and RIFNI, O. Bias weaving machine. US Patent 7077167. 2006.
 73. SÁDABA, S., MARTÍNEZ-HERGUETA, F., LOPES, C.S., GONZALEZ, C. and LLORCA, J. Virtual testing of impact in fiber reinforced laminates. In : *Structural Integrity and Durability of Advanced Composites*. Online. Elsevier, 2015. p. 247–270.
 74. ABDUROHMAN, K., SATRIO, T., MUZAYADAH, N. L. and TETEN. A comparison process between hand lay-up, vacuum infusion and vacuum bagging method toward e-glass EW 185/lycal composites. *Journal of Physics: Conference Series*. 2018. Vol. 1130, no. 1. DOI 10.1088/1742-6596/1130/1/012018.
 75. CUCINOTTA, Filippo, GUGLIELMINO, Eugenio and SFRAVARA, Felice. Life cycle assessment in yacht industry: A case study of comparison between hand lay-up and vacuum infusion. *Journal of Cleaner Production*. Online. 2017. Vol. 142, p. 3822–3833. DOI 10.1016/j.jclepro.2016.10.080.
 76. SUGUN, B. S. and RAO, R. M.V.G.K. Drop weight impact studies on rib-knit RTM laminates. *Journal of Reinforced Plastics and Composites*. 2000. DOI 10.1106/DND1-1F83-6BBL-BTP7.
 77. JHAN, Yu Ti, LEE, Ya Jung and CHUNG, Cheng Hsien. Resin flowing analysis in sandwich laminates under VARTM process. *Journal of Reinforced Plastics and Composites*. 2011. Vol. 30, no. 6, p. 533–545. DOI 10.1177/0731684411399142.
 78. ATAS, Cesim, AKGUN, Yalin, DAGDELEN, Olgay, ICTEN, Bulent M. and SARIKANAT, Mehmet. An experimental investigation on the low velocity impact response of composite plates repaired by VARIM and hand lay-up processes.

- Composite Structures*. Online. 2011. Vol. 93, no. 3, p. 1178–1186. DOI 10.1016/j.compstruct.2010.10.002.
79. MOURITZ, A.P., LEONG, K.H. and HERSZBERG, I. A review of the effect of stitching on the in-plane mechanical properties of fibre-reinforced polymer composites. *Composites Part A: Applied Science and Manufacturing*. Online. January 1997. Vol. 28, no. 12, p. 979–991. DOI 10.1016/S1359-835X(97)00057-2.
80. MOURITZ, A.P. Review of z-pinned composite laminates. *Composites Part A: Applied Science and Manufacturing*. Online. December 2007. Vol. 38, no. 12, p. 2383–2397. DOI 10.1016/j.compositesa.2007.08.016.
81. IVANOV, Dmitry S., LOMOV, Stepan V., BOGDANOVICH, Alexander E., KARAHAN, Mehmet and VERPOEST, Ignaas. A comparative study of tensile properties of non-crimp 3D orthogonal weave and multi-layer plain weave E-glass composites. Part 2: Comprehensive experimental results. *Composites Part A: Applied Science and Manufacturing*. 2009. DOI 10.1016/j.compositesa.2009.04.032.
82. GOKARNESHAN, N. and ALAGIRUSAMY, R. *Weaving of 3D fabrics: A critical appreciation of the developments*. 2009.
83. HUANG, Tao, WANG, Yanling and WANG, Gang. Review of the Mechanical Properties of a 3D Woven Composite and Its Applications. *Polymer - Plastics Technology and Engineering*. Online. 24 May 2018. Vol. 57, no. 8, p. 740–756. [Accessed 9 February 2023]. DOI 10.1080/03602559.2017.1344857.
84. WANG, Chunxia, LU, Zhenqian and JIN, Limin. A review on the mechanical performance and fatigue behavior of 3-D angle-interlock woven composites. *The Journal of The Textile Institute*. Online. 2 December 2015. Vol. 106, no. 12, p. 1306–1314. DOI 10.1080/00405000.2014.998872.
85. CHEN, F. and HODGKINSON, J. M. Impact behaviour of composites with different fibre architecture. *Proceedings of the Institution of Mechanical Engineers, Part G: Journal of Aerospace Engineering*. 2009. DOI 10.1243/09544100JAERO451.
86. SALEH, Mohamed Nasr and SOUTIS, Constantinos. Recent advancements in mechanical characterisation of 3D woven composites. *Mechanics of Advanced Materials and Modern Processes*. 2017. DOI 10.1186/s40759-017-0027-z.
87. COX, Brian N., DADKHAH, Mahyar S. and MORRIS, W.L. On the tensile failure of 3D woven composites. *Composites Part A: Applied Science and Manufacturing*. Online. January 1996. Vol. 27, no. 6, p. 447–458. DOI 10.1016/1359-835X(95)00053-5.
88. JIN, Limin, HU, Hong, SUN, Baozhong and GU, Bohong. Three-point bending fatigue behavior of 3D angle-interlock woven composite. *Journal of Composite Materials*. Online. 15 April 2012. Vol. 46, no. 8, p. 883–894. [Accessed 4 February 2023]. DOI 10.1177/0021998311412218.
89. CHEN, X, SPOLA, M, PAYA, J. Gisbert and SELLABONA1, P. Mollst. Experimental Studies on the Structure and Mechanical Properties of Multi-layer and Angle-interlock Woven Structures. *The Journal of The Textile Institute*. Online. 30 January 1999. Vol. 90, no. 1, p. 91–99. [Accessed 9 February 2023]. DOI 10.1080/00405009908658693.
90. CHEN, Xiaogang, TAYLOR, Lindsay Waterton and TSAI, Li ju. An overview on fabrication of three-dimensional woven textile preforms for composites. *Textile Research Journal*. 2011. DOI 10.1177/0040517510392471.
91. TAN, Ping, TONG, Liyong and STEVEN, G.P. Behavior of 3D orthogonal woven CFRP composites. Part II. FEA and analytical modeling approaches. *Composites Part A: Applied Science and Manufacturing*. Online. March 2000. Vol. 31, no. 3, p. 273–

281. [Accessed 9 February 2023]. DOI 10.1016/S1359-835X(99)00071-8.
92. TAN, Ping, TONG, Liyong, STEVEN, G. P. and ISHIKAWA, Takashi. Behavior of 3D orthogonal woven CFRP composites. Part I. Experimental investigation. *Composites Part A: Applied Science and Manufacturing*. Online. March 2000. Vol. 31, no. 3, p. 259–271. [Accessed 9 February 2023]. DOI 10.1016/S1359-835X(99)00070-6.
 93. COX, B. N. and DADKHAH, M. S. The Macroscopic Elasticity of 3D Woven Composites. *Journal of Composite Materials*. Online. 1995. Vol. 29, no. 6, p. 785–819. [Accessed 9 February 2023]. DOI 10.1177/002199839502900606.
 94. JIN, Limin, JIN, Bo Cheng, KAR, Nikhil, NUTT, Steven, SUN, Baozhong and GU, Bohong. Tension–tension fatigue behavior of layer-to-layer 3-D angle-interlock woven composites. *Materials Chemistry and Physics*. Online. June 2013. Vol. 140, no. 1, p. 183–190. [Accessed 4 February 2023]. DOI 10.1016/j.matchemphys.2013.03.020.
 95. KHOKAR, N. 3D-Weaving: Theory and Practice. *Journal of the Textile Institute*. 2001. DOI 10.1080/00405000108659570.
 96. DHIMAN, Sarvesh, POTLURI, Prasad and SILVA, Christopher. Influence of binder configuration on 3D woven composites. *Composite Structures*. 2015. DOI 10.1016/j.compstruct.2015.08.126.
 97. GREENWOOD, K. Weaving Loom. U.S. Patent No. 3818951. 1974.
 98. R.W., King. Three dimensional fabric material. Online. 4, 038,440. 1977. US Patent. [Accessed 20 February 2023]. Available from: <https://patents.google.com/patent/US4038440A/en>
 99. SUGUN, BS. *Practical Approach to 3D Weaving*. Online. Cham : Springer International Publishing, 2021. Materials Horizons: From Nature to Nanomaterials. ISBN 978-3-030-80423-7.
 100. CHIU, Chang Hsuan and CHENG, Chao Chuan. Weaving Method of 3D Woven Preforms for Advanced Composite Materials. *Textile Research Journal*. 2003. DOI 10.1177/004051750307300107.
 101. RUDOV-CLARK, S., MOURITZ, A. P., LEE, L. and BANNISTER, M. K. Fibre damage in the manufacture of advanced three-dimensional woven composites. *Composites Part A: Applied Science and Manufacturing*. 2003. DOI 10.1016/S1359-835X(03)00213-6.
 102. REIFSNIDER, KL, SENDECKYJ, GP, WANG, SS, CHAIO, TT, FENG, W, STEVEN JOHNSON, W, RODERICKS, GL, STINCHCOMB, WW, GUESS, TR and REEDY, ED. Comparison of Interlocked Fabric and Laminated Fabric Kevlar 49/Epoxy Composites. *Journal of Composites Technology and Research*. Online. 1985. Vol. 7, no. 4, p. 136. [Accessed 11 February 2023]. DOI 10.1520/CTR10310J.
 103. MAHADIK, Y., BROWN, K. A. Robson and HALLETT, S. R. Characterisation of 3D woven composite internal architecture and effect of compaction. *Composites Part A: Applied Science and Manufacturing*. 2010. DOI 10.1016/j.compositesa.2010.02.019.
 104. STIG, Fredrik and HALLSTRÖM, Stefan. Influence of crimp on 3D-woven fibre reinforced composites. *Composite Structures*. 2013. DOI 10.1016/j.compstruct.2012.07.022.
 105. FLECK, N. A., JELF, P. M. and CURTIS, P. T. Compressive failure of laminated and woven composites. *Journal of Composites Technology and Research*. 1995. DOI 10.1520/ctr10485j.
 106. GU, Huang and ZHILI, Zhong. Tensile behavior of 3D woven composites by using different fabric structures. *Materials and Design*. 2002. DOI 10.1016/s0261-

- 3069(02)00053-5.
107. KUO, Wen Shyong, KO, Tse Hao and CHEN, Cheng Po. Effect of weaving processes on compressive behavior of 3D woven composites. *Composites Part A: Applied Science and Manufacturing*. 2007. DOI 10.1016/j.compositesa.2006.02.025.
 108. GUO, Xu, LI, Wang and QIU, Yi Ping. Compressive behavior of 3-D Kevlar/epoxy woven composites at various strain rates. *Hangkong Cailiao Xuebao/Journal of Aeronautical Materials*. Online. 2006. Vol. 26, no. 6, p. 68–71. [Accessed 11 February 2023]. Available from: https://www.sciencedirect.com/science/article/pii/S0142941805000103?casa_token=MGYaf923MnUAAAAA:rpaz2ggir3_sloe3HNB3-hj4LnMIelg27YotJJRwaYYv4R8Ai6jddkIQav96ilYwFoasM3td5Q
 109. GERLACH, Robert, SIVIOUR, Clive R., WIEGAND, Jens and PETRINIC, Nik. In-plane and through-thickness properties, failure modes, damage and delamination in 3D woven carbon fibre composites subjected to impact loading. *Composites Science and Technology*. 2012. DOI 10.1016/j.compscitech.2011.11.032.
 110. DORNIER, Lindauer. Quality creates value PI rapier weaving machine with Open Reed Weave (ORW) technology for multiaxial weaving. Online. [Accessed 9 April 2023]. Available from: www.lindauerdornier.com
 111. KATUNIN, Andrzej, DRAGAN, Krzysztof and DZIENDZIKOWSKI, Michał. Damage identification in aircraft composite structures: A case study using various non-destructive testing techniques. *Composite Structures*. 2015. DOI 10.1016/j.compstruct.2015.02.080.
 112. SCOTT, I. G. and SCALA, C. M. A review of non-destructive testing of composite materials. *NDT International*. 1982. DOI 10.1016/0308-9126(82)90001-3.
 113. DUFOUR, Clément, BOUSSU, François, WANG, Peng and SOULAT, Damien. Local strain measurements of yarns inside of 3D warp interlock fabric during forming process. *International Journal of Material Forming*. Online. 6 November 2018. Vol. 11, no. 6, p. 775–788. DOI 10.1007/s12289-017-1385-0.
 114. QURESHI, Y., TARFAOUI, M., LAFDI, K. K. and LAFDI, K. Development of microscale flexible nylon/Ag strain sensor wire for real-time monitoring and damage detection in composite structures subjected to three-point bend test. *Composites Science and Technology*. Online. 2019. Vol. 181, no. June, p. 107693. DOI 10.1016/j.compscitech.2019.107693.
 115. KHAN, Taimoor A, NAUMAN, Saad, ASFAR, Zeeshan, NASIR, M. Ali and KHAN, Zaffar M. Screen-printed nanocomposite sensors for online in situ structural health monitoring. *Journal of Thermoplastic Composite Materials*. Online. 11 February 2020. Vol. 33, no. 2, p. 236–253. DOI 10.1177/0892705718805131.
 116. KIM, Young Ju, CHA, Ju Young, HAM, Heon, HUH, Hoon, SO, Dae Sup and KANG, Inpil. Preparation of piezoresistive nano smart hybrid material based on graphene. In : *Current Applied Physics*. 2011. DOI 10.1016/j.cap.2010.11.022.
 117. BEITOLLAHI, Hadi and GARKANI NEJAD, Fariba. Graphene Oxide/ZnO Nano Composite for Sensitive and Selective Electrochemical Sensing of Levodopa and Tyrosine Using Modified Graphite Screen Printed Electrode. *Electroanalysis*. 2016. DOI 10.1002/elan.201600143.
 118. STARKOVA, O., MANNOV, E., SCHULTE, K. and ANISKEVICH, A. Strain-dependent electrical resistance of epoxy/MWCNT composite after hydrothermal aging. *Composites Science and Technology*. Online. 2015. Vol. 117, p. 107–113. DOI 10.1016/j.compscitech.2015.06.004.
 119. ZHANG, Han, KUWATA, Manabu, BILOTTI, Emiliano and PEIJS, Ton. Integrated

- damage sensing in fibre-reinforced composites with extremely low carbon nanotube loadings. *Journal of Nanomaterials*. 2015. Vol. 2015, p. 1–7. DOI 10.1155/2015/785834.
120. LI, Weikang, DICHIARA, Anthony and BAI, Jinbo. Carbon nanotube-graphene nanoplatelet hybrids as high-performance multifunctional reinforcements in epoxy composites. *Composites Science and Technology*. 2013. DOI 10.1016/j.compscitech.2012.11.015.
 121. HU, Ning, KARUBE, Yoshifumi, ARAI, Masahiro, WATANABE, Tomonori, YAN, Cheng, LI, Yuan, LIU, Yaolu and FUKUNAGA, Hisao. Investigation on sensitivity of a polymer/carbon nanotube composite strain sensor. *Carbon*. Online. 2010. Vol. 48, no. 3, p. 680–687. DOI 10.1016/j.carbon.2009.10.012.
 122. COSTA, P., SILVA, J., ANSÓN-CASAOS, A., MARTINEZ, M. T., ABAD, M. J., VIANA, J. and LANCEROS-MENDEZ, S. Effect of carbon nanotube type and functionalization on the electrical, thermal, mechanical and electromechanical properties of carbon nanotube/styrene-butadiene-styrene composites for large strain sensor applications. *Composites Part B: Engineering*. 2014. DOI 10.1016/j.compositesb.2014.01.048.
 123. TAKEDA, Tomo, SHINDO, Yasuhide, KURONUMA, Yu and NARITA, Fumio. Modeling and characterization of the electrical conductivity of carbon nanotube-based polymer composites. *Polymer*. Online. August 2011. Vol. 52, no. 17, p. 3852–3856. DOI 10.1016/j.polymer.2011.06.046.
 124. SU, Yanan, ZHANG, Shouchun, ZHANG, Xinghua, ZHAO, Zhenbo and JING, Deqi. Preparation and properties of carbon nanotubes/carbon fiber/poly (ether ether ketone) multiscale composites. *Composites Part A: Applied Science and Manufacturing*. Online. 2018. Vol. 108, no. October 2017, p. 89–98. DOI 10.1016/j.compositesa.2018.02.030.
 125. KARGER-KOCSIS, József, MAHMOOD, Haroon and PEGORETTI, Alessandro. All-carbon multi-scale and hierarchical fibers and related structural composites: A review. *Composites Science and Technology*. 2019. Vol. 186, no. 2020, p. 1–15. DOI 10.1016/j.compscitech.2019.107932.
 126. SHIMPI, Prasad, ANISKEVICH, Andrey and ZELENIAKIENE, Daiva. Improved method of manufacturing carbon nanotube infused multifunctional 3D woven composites. *Journal of Composite Materials*. Online. 14 February 2022. Vol. 56, no. 3, p. 479–489. DOI 10.1177/00219983211055823.
 127. STIG, Fredrik and HALLSTRÖM, Stefan. Assessment of the mechanical properties of a new 3D woven fibre composite material. *Composites Science and Technology*. 2009. DOI 10.1016/j.compscitech.2008.04.047.
 128. CHEE HO, Kingsley Kin, QIAN, Hui and BISMARCK, Alexander. Carbon Fiber: Surface Properties. In : *Wiley Encyclopedia of Composites*. Online. John Wiley & Sons, Ltd, 2011. p. 1–11. [Accessed 11 February 2023].
 129. BOCCACCINI, Aldo R, CHO, Johann, ROETHER, Judith A, THOMAS, Boris J C, MINAY, E Jane and SHAFFER, Milo S P. Electrophoretic deposition of carbon nanotubes. . 2006. Vol. 44, p. 3149–3160. DOI 10.1016/j.carbon.2006.06.021.
 130. YU, Bin, JIANG, Zhenyu, TANG, Xiu Zhi, YUE, Chee Yoon and YANG, Jinglei. Enhanced interphase between epoxy matrix and carbon fiber with carbon nanotube-modified silane coating. *Composites Science and Technology*. Online. 30 July 2014. Vol. 99, p. 131–140. [Accessed 11 February 2023]. DOI 10.1016/j.compscitech.2014.05.021.
 131. XU, Junyi, XU, Dongxia, WANG, Xiaojun, LONG, Shengru and YANG, Jie.

- Improved interfacial shear strength of carbon fiber/polyphenylene sulfide composites by graphene. <https://doi.org/10.1177/0954008316664398>. Online. 7 December 2016. Vol. 29, no. 8, p. 913–921. [Accessed 11 February 2023]. DOI 10.1177/0954008316664398.
132. MA, Lin, WU, Lixin, CHENG, Xiuyan, ZHUO, Dongxian, WENG, Zixiang and WANG, Rui. Improving the interlaminar properties of polymer composites using a situ accumulation method to construct the multi-scale reinforcement of carbon nanofibers/carbon fibers. *Composites Part A: Applied Science and Manufacturing*. 1 May 2015. Vol. 72, p. 65–74. DOI 10.1016/j.compositesa.2015.01.023.
 133. LEE, Chang Yeong, BAE, Ji Hun, KIM, Tae Yoon, CHANG, Seung Hwan and KIM, Soo Young. Using silane-functionalized graphene oxides for enhancing the interfacial bonding strength of carbon/epoxy composites. *Composites Part A: Applied Science and Manufacturing*. 1 August 2015. Vol. 75, p. 11–17. DOI 10.1016/J.COMPOSITESA.2015.04.013.
 134. FENG, Chuang and JIANG, Liying. Micromechanics modeling of the electrical conductivity of carbon nanotube (CNT)-polymer nanocomposites. *Composites Part A: Applied Science and Manufacturing*. 2013. Vol. 47, p. 143–149. DOI 10.1016/j.compositesa.2012.12.008.
 135. GONG, Kaili, ZHOU, Keqing, QIAN, Xiaodong, SHI, Congling and YU, Bin. MXene as emerging nanofillers for high-performance polymer composites: A review. *Composites Part B: Engineering*. Online. July 2021. Vol. 217, p. 108867. DOI 10.1016/j.compositesb.2021.108867.
 136. GAO, Lingfeng, LI, Chao, HUANG, Weichun, MEI, Shan, LIN, Han, OU, Qi, ZHANG, Ye, GUO, Jia, ZHANG, Feng, XU, Shixiang and ZHANG, Han. MXene/Polymer Membranes: Synthesis, Properties, and Emerging Applications. *Chemistry of Materials*. Online. 10 March 2020. Vol. 32, no. 5, p. 1703–1747. DOI 10.1021/acs.chemmater.9b04408.
 137. HAI, Yun, JIANG, Saihua, ZHOU, Chilou, SUN, Ping, HUANG, Yubin and NIU, Shichao. Fire-safe unsaturated polyester resin nanocomposites based on MAX and MXene: a comparative investigation of their properties and mechanism of fire retardancy. *Dalton Transactions*. Online. 2020. Vol. 49, no. 18, p. 5803–5814. DOI 10.1039/D0DT00686F.
 138. WANG, Xiaoqiang, LU, Jian, LU, Shaowei, LI, Bo, ZHANG, Lu, MA, Chengkun, MA, Keming, LIN, Lunyang, JIANG, Xiaowei and YANG, Bin. Health monitoring of repaired composite structure using MXene sensor. *Composites Communications*. Online. October 2021. Vol. 27, no. June, p. 100850. DOI 10.1016/j.coco.2021.100850.
 139. SHIMPI, Prasad, OMASTOVA, Maria, ANISKEVICH, Andrey and ZELENIAKIENE, Daiva. In Situ Deformation Monitoring of 3D Woven Composite T-Profile Using MXene Nanoparticles. *Materials*. Online. 7 April 2022. Vol. 15, no. 8, p. 2730. DOI 10.3390/ma15082730.
 140. DEYSHER, Grayson, SHUCK, Christopher Eugene, HANTANASIRISAKUL, Kanit, FREY, Nathan C., FOUCHER, Alexandre C., MALESKI, Kathleen, SARYCHEVA, Asia, SHENOY, Vivek B., STACH, Eric A., ANASORI, Babak and GOGOTSI, Yury. Synthesis of Mo₄VAIc₄ MAX Phase and Two-Dimensional Mo₄VC₄ MXene with Five Atomic Layers of Transition Metals. *ACS Nano*. 28 January 2020. Vol. 14, no. 1, p. 204–217. DOI 10.1021/ACS.NANO.9B07708.
 141. KHAZAEI, Mohammad, RANJBAR, Ahmad, ESFARJANI, Keivan, BOGDANOVSKI, Dimitri, DRONSKOWSKI, Richard and YUNOKI, Seiji. Insights

- into exfoliation possibility of MAX phases to MXenes. *Physical Chemistry Chemical Physics*. Online. 2018. Vol. 20, no. 13, p. 8579–8592. [Accessed 17 February 2023]. DOI 10.1039/C7CP08645H.
142. YANG, Jian, BAO, Weizhai, JAUMAUX, Pauline, ZHANG, Songtao, WANG, Chengyin and WANG, Guoxiu. MXene-Based Composites: Synthesis and Applications in Rechargeable Batteries and Supercapacitors. *Advanced Materials Interfaces*. Online. 18 April 2019. Vol. 6, no. 8, p. 1802004. DOI 10.1002/admi.201802004.
 143. NAGUIB, Michael, MASHTALIR, Olha, CARLE, Joshua, PRESSER, Volker, LU, Jun, HULTMAN, Lars, GOGOTSI, Yury and BARSOUM, Michel W. Two-Dimensional Transition Metal Carbides. *ACS Nano*. Online. 28 February 2012. Vol. 6, no. 2, p. 1322–1331. DOI 10.1021/nn204153h.
 144. HE, Shuangjiang, ZHAN, Yingqing, HU, Jiabin, ZHANG, Guiyuan, ZHAO, Shumei, FENG, Qingying and YANG, Wei. Chemically stable two-dimensional MXene@UO-66-(COOH)₂ composite lamellar membrane for multi-component pollutant-oil-water emulsion separation. *Composites Part B: Engineering*. 15 September 2020. Vol. 197, p. 108188.
 145. HUANG, Hongye, JIANG, Rumeng, FENG, Yulin, OUYANG, Hui, ZHOU, Naigen, ZHANG, Xiaoyong and WEI, Yen. Recent development and prospects of surface modification and biomedical applications of MXenes. *Nanoscale*. Online. 2020. Vol. 12, no. 3, p. 1325–1338. [Accessed 17 February 2023]. DOI 10.1039/C9NR07616F.
 146. PU, Jun-Hong, ZHAO, Xing, ZHA, Xiang-Jun, BAI, Lu, KE, Kai, BAO, Rui-Ying, LIU, Zheng-Ying, YANG, Ming-Bo and YANG, Wei. Multilayer structured AgNW/WPU-MXene fiber strain sensors with ultrahigh sensitivity and a wide operating range for wearable monitoring and healthcare. *Journal of Materials Chemistry A*. Online. 2019. Vol. 7, no. 26, p. 15913–15923. DOI 10.1039/C9TA04352G.
 147. MA, Chang, CAO, Wen-Tao, ZHANG, Wei, MA, Ming-Guo, SUN, Wen-Ming, ZHANG, Juan and CHEN, Feng. Wearable, ultrathin and transparent bacterial celluloses/MXene film with Janus structure and excellent mechanical property for electromagnetic interference shielding. *Chemical Engineering Journal*. Online. January 2021. Vol. 403, p. 126438. DOI 10.1016/j.cej.2020.126438.
 148. SONG, Guichen, KANG, Ruiyang, GUO, Liangchao, ALI, Zulfiqar, CHEN, Xiaoyong, ZHANG, Zhenyu, YAN, Chao, LIN, Cheng-Te, JIANG, Nan and YU, Jinhong. Highly flexible few-layer Ti₃C₂ MXene/cellulose nanofiber heat-spreader films with enhanced thermal conductivity. *New Journal of Chemistry*. Online. 2020. Vol. 44, no. 17, p. 7186–7193. DOI 10.1039/D0NJ00672F.
 149. XUE, Yijiao, FENG, Jiabing, HUO, Siqi, SONG, Pingan, YU, Bin, LIU, Lei and WANG, Hao. Polyphosphoramidate-intercalated MXene for simultaneously enhancing thermal stability, flame retardancy and mechanical properties of polylactide. *Chemical Engineering Journal*. Online. October 2020. Vol. 397, p. 125336. DOI 10.1016/j.cej.2020.125336.
 150. LIN, Bo, YUEN, Anthony Chun Yin, LI, Ao, ZHANG, Yang, CHEN, Timothy Bo Yuan, YU, Bin, LEE, Eric Wai Ming, PENG, Shuhua, YANG, Wei, LU, Hong-Dian, CHAN, Qing Nian, YEOH, Guan Heng and WANG, Chun H. MXene/chitosan nanocoating for flexible polyurethane foam towards remarkable fire hazards reductions. *Journal of Hazardous Materials*. Online. January 2020. Vol. 381, p. 120952. DOI 10.1016/j.jhazmat.2019.120952.

151. HANDSCHUH-WANG, Stephan, WANG, Tao and TANG, Yongbing. Ultrathin Diamond Nanofilms—Development, Challenges, and Applications. *Small*. Online. 26 July 2021. Vol. 17, no. 30, p. 2007529. DOI 10.1002/smll.202007529.
152. SI, Jing-Yu, TAWIAH, Benjamin, SUN, Wei-Long, LIN, Bo, WANG, Cheng, YUEN, Anthony, YU, Bin, LI, Ao, YANG, Wei, LU, Hong-Dian, CHAN, Qing and YEOH, Guan. Functionalization of MXene Nanosheets for Polystyrene towards High Thermal Stability and Flame Retardant Properties. *Polymers*. Online. 3 June 2019. Vol. 11, no. 6, p. 976. DOI 10.3390/polym11060976.
153. RAJAVEL, Krishnamoorthy, LUO, Suibin, WAN, Yanjun, YU, Xuecheng, HU, Yougen, ZHU, Pengli, SUN, Rong and WONG, Chingping. 2D Ti₃C₂T_x MXene/polyvinylidene fluoride (PVDF) nanocomposites for attenuation of electromagnetic radiation with excellent heat dissipation. *Composites Part A: Applied Science and Manufacturing*. Online. February 2020. Vol. 129, p. 105693. DOI 10.1016/j.compositesa.2019.105693.
154. ASKARI, Ehsan. Mathematical models for characterizing non-Hertzian contacts. *Applied Mathematical Modelling*. 1 February 2021. Vol. 90, p. 432–447. DOI 10.1016/J.APM.2020.08.048.
155. LI, C. F., HU, N., YIN, Y. J., SEKINE, H. and FUKUNAGA, H. Low-velocity impact-induced damage of continuous fiber-reinforced composite laminates. Part I. An FEM numerical model. *Composites Part A: Applied Science and Manufacturing*. 1 August 2002. Vol. 33, no. 8, p. 1055–1062. DOI 10.1016/S1359-835X(02)00081-7.
156. LIN, H. J. and LEE, Y. J. Use of statical indentation laws in the impact analysis of composite laminated plates and shells. *Journal of Applied Mechanics, Transactions ASME*. Online. 1990. Vol. 57, no. 3, p. 787–789. [Accessed 24 February 2023]. DOI 10.1115/1.2897095.
157. BARBERO, Ever J. *Finite Element Analysis of Composite Materials Using ANSYS*., *Second Edition*. Online. 2013. [Accessed 15 March 2023]. ISBN 9781466516908. Available from: https://books.google.com/books?hl=en&lr=&id=sKHT0WwTm2UC&oi=fnd&pg=P1&ots=jP1Jo7vD6l&sig=8PGg_shcTVvEwsCkxVuxc4z5rr4
158. HASHIN, Z. Failure criteria for unidirectional fiber composites. *Journal of Applied Mechanics, Transactions ASME*. Online. 1 June 1980. Vol. 47, no. 2, p. 329–334. [Accessed 15 March 2023]. DOI 10.1115/1.3153664.
159. BARBERO, Ever J. and SHAHBAZI, Mehdi. Determination of material properties for ANSYS progressive damage analysis of laminated composites. *Composite Structures*. 15 September 2017. Vol. 176, p. 768–779. DOI 10.1016/J.COMPSTRUCT.2017.05.074.
160. WANG, Wenzhi, WAN, Xiaopeng, ZHOU, Jun, ZHAO, Meiyong, LI, Yulong, SHANG, Shen and GAO, Xiaosheng. Damage and Failure of Laminated Carbon-Fiber-Reinforced Composite under Low-Velocity Impact. *Journal of Aerospace Engineering*. March 2014. Vol. 27, no. 2, p. 308–317. DOI 10.1061/(ASCE)AS.1943-5525.0000243.
161. DINESH, D and RAJU, F Anand. Optimum Design And Analysis Of A Composite Drive Shaft For An Automobile By Using Genetic Algorithm And Ansys. *International Journal Of Engineering Research And Applications (IJERA)*. Vol. 2, p. 1874–1880.
162. DAS, Subhankar, CHOUDHURY, Pannalal, HALDER, Sudipta and SRIRAM, P. Stress and Free Edge Delamination Analyses of Delaminated Composite Structure Using ANSYS. *Procedia Engineering*. 1 January 2013. Vol. 64, p. 1364–1373.

- DOI 10.1016/J.PROENG.2013.09.218.
163. ECHAABI, Jamal, TROCHU, François and GAUVIN, Raymond. Review of failure criteria of fibrous composite materials. *Polymer Composites*. Online. 1 December 1996. Vol. 17, no. 6, p. 786–798. [Accessed 25 February 2023]. DOI 10.1002/PC.10671.
 164. ZHENG, Jianxiao, DUAN, Zhishan and ZHOU, Liming. Finite element analysis and energy recovery calculation of carbon fiber composite based on ANSYS software. *Journal of Applied Biomaterials and Functional Materials*. Online. 4 January 2022. Vol. 20, p. 228080002211400. [Accessed 23 February 2023]. DOI 10.1177/22808000221140059.
 165. ALBAHKALI, T., ALSANABANI, N., SOULI, M. and ALBAHKALI, E. A concept to estimate the life cycle of the railway track using finite element modeling. *International Journal of Multiphysics*. Online. 11 July 2021. Vol. 15, no. 3, p. 265–274. [Accessed 23 February 2023]. DOI 10.21152/1750-9548.15.3.275.
 166. VIJAYANANDH, R., VENKATESAN, K., RAMESH, M., RAJ KUMAR, G. and SENTHIL KUMAR, M. Optimization of orientation of carbon fiber reinforced polymer based on structural analysis. *International Journal of Scientific and Technology Research*. Online. 2019. Vol. 8, no. 11, p. 3020–3029. [Accessed 23 February 2023]. Available from: www.ijstr.org
 167. SHIMPI, Prasad, SRIDHARAN, Sugun Bangalore, MONASTYRECKIS, Gediminas and ZELENIAKIENE, Daiva. Novel method of multiaxis weaving and impact analysis of the ensuing composites. *Journal of Composite Materials*. Online. 4 January 2024. DOI 10.1177/00219983231225453.
 168. LYSSAKOW, Pawel, STEIN, Sebastian, HUBER, Philipp, SCHLESINGER, Yanick and SCHRÖDER, Kai-Uwe. TOWARDS AN ANALYTICAL AND NUMERICAL DESIGN APPROACH FOR TAILORED TEXTILES. In : . 2019.

CURRICULUM VITAE

Prasad Shimpi

prasad.shimpi@ktu.edu

Education

2010 – 2014 Bachelor's degree in Textile Engineering

2015 – 2017 Master's degree in Textile Engineering

2019 – 2023 PhD studies in Mechanical Engineering

Professional experience

2014 – 2015 Graduate Engineer trainee at *Arvind OG Ltd.*, India

2017 – 2019 Research Assistant at the *National Aerospace Laboratory*, India

2019 – present PhD researcher at Kaunas University of Technology

Areas of research interest

Research and development of 3D woven self-sensing composites infused with nanoparticles, such as carbon nanotube and MXene. Development of biased weaving and tailored fibre placement

Scientific papers related to the topic of dissertation.

ARTICLES IN PEER-REVIEWED SCIENTIFIC PUBLICATIONS

In publications indexed in the Web of Science with Impact Factor (JCR SCIE)

International (foreign) publishers

1. [S1; CH; OA] **Shimpi, Prasad**; Omastova, Maria; Aniskevich, Andrey; Zeleniakiene, Daiva. In situ deformation monitoring of 3D woven composite T-profile using MXene nanoparticles // *Materials*. Basel: MDPI. ISSN 1996-1944. 2022, Vol. 15, iss. 8, art. No. 2730, p. 1 –10. DOI: 10.3390/ma15082730. [Science Citation Index Expanded (Web of Science); Q1 (2021, InCites JCR SCIE)] [FOR: T 009] [Input: 0.250]
2. [S1; GB] **Shimpi, Prasad**; Aniskevich, Andrey; Zeleniakiene, Daiva. Improved method of manufacturing carbon nanotube infused multifunctional 3D woven composites // *Journal of Composite Materials*. London: SAGE. ISSN 0021-9983. eISSN 1530-793X. 2022, Vol. 56, iss. 3, p. 479–489. DOI: 10.1177/00219983211055823. [Science Citation Index Expanded (Web of Science); Q3 (2021, InCites JCR SCIE)] [FOR: T 009] [Input: 0.334]

3. [S1; GB] **Shimpi, Prasad**; Sridharan Sugun Bangalore; Monastyreckis Gediminas; Zeleniakiene Daiva. Novel method of multiaxis weaving and impact analysis of the ensuing composites // *Journal of Composite Materials*. London: SAGE. ISSN 0021-9983. eISSN1530-793X. 2024, 0(0). DOI:10.1177/00219983231225453. [Science Citation Index Expanded (Web of Science); Q3 (2021, InCites JCR SCIE)] [FOR: T 009] [Input: 0.250]

CONFERENCE PROCEEDINGS

- 1.[P1b; CH; OA] Shimpi, Prasad; Zeleniakiene, Daiva; Spacek, Vladimir. Strain sensing of complex shaped 3D woven composite using MXene nanoparticles // *Composites meet sustainability*. Vol. 1 – *Materials: proceedings of the 20th European conference on composite materials, ECCM20*, 26–30 June 2022, Lausanne, Switzerland / edited by: A.P. Vassilopoulos, V. Michaud. Lausanne: Ecole Polytechnique Fédérale de Lausanne, 2022. eISBN 9782970161400. p. 516–521. [FOR: T 009] [Input: 0.334].
- 2.[T3; LV] Shimpi, Prasad; Zeleniakiene, Daiva. Improved method of manufacturing multiaxial woven composites // *Advanced composites and applications: 81st international scientific conference of the University of Latvia*, February 16, 2023: book of abstracts. Riga : University of Latvia. 2023, p. 10. [FOR: T 009].
3. [T3; LV; OA] Shimpi, Prasad; Zeleniakiene, Daiva. Structural health monitoring of 3d woven composites using mxene nanoparticles // *Advanced composites and applications: 80th international scientific conference of the University of Latvia*, February 15, 2022: book of abstracts. Riga : University of Latvia. 2022, p. 14. [FOR: T009].
4. [T3; LV; OA] Shimpi, P.; Zeleniakiene, D. Structural health monitoring of 3D woven composites by carbon nanotube strain gauges // *Durability of advanced polymer composites: 79th conference of the University of Latvia*, online, February 16, 2021: book of abstracts. [Riga] : [University of Latvia]. 2021, p. 13. DOI: 10.22364/iscful.79.dapc.ab. [FOR: T 009].

ACKNOWLEDGEMENTS

I would like to express my sincere gratitude to the following individuals and organizations who have played a crucial role in the completion of this thesis:

H2020-MSCA-RISE-2017 Project No. 777810 *Multifunctional polymer composites doped with novel 2D nanoparticles for advanced applications*, Nano2Day. This project received funding from the European Union's *Horizon 2020* research and innovation program under the Marie Skłodowska-Curie grant agreement No. 777810.

My supervisor Prof. Dr. Daiva Zeleniakienė: Your guidance, support, and invaluable feedback have been instrumental throughout this research journey. Your expertise and encouragement have truly shaped the direction of this thesis.

Faculty Members: I extend my appreciation to the faculty members, especially Prof. Dr. Paulius Griškevičius and Dr. Vitalis Leišis of Mechanical Engineering, Dr. Ahmed Samy Yousef Saed of Production Engineering, Dr. Valdas Norvydas, head of laboratories, for their academic insight, stimulating discussions, and for fostering an environment conducive to scholarly pursuits.

Family: A heartfelt thank you to my wife Preethi, mother Hemangi and brother Rushikesh for their unwavering support, understanding, and encouragement. Your belief in me has been my pillar of strength, and I am deeply grateful for the sacrifices you have made to see me through this academic endeavour.

Friends: To my friends who have been providing not only academic assistance but also emotional support, thank you for being there during the challenging times and for celebrating the successes together.

Peers and Colleagues: I am grateful to my peers and colleagues Dr. Gediminas Monastyreckis, Dr. Sharath Subadra and Tomas Simonaitis who have offered so many valuable insights, shared resources, and engaged in thoughtful discussions which enriched the quality of this research.

Institutional Support: I acknowledge the support provided by *SYNPO a.s* and RWTH Aachen University, including the access to resources, facilities, and research funding that have enhanced the quality and scope of this thesis.

This thesis is a testament to the collaborative efforts of a community of people, and I am profoundly grateful for the role each of you has played.

UDK 620.17+677.074+666.189.212](043.3)

SL344. 2021-*-* , * leidyb. apsk. I. Tiražas 14 egz. Užsakymas * .
Išleido Kauno technologijos universitetas, K. Donelaičio g. 73, 44249 Kaunas
Spausdino leidyklos „Technologija“ spaustuvė, Studentų g. 54, 51424 Kaunas